Aus dem Institut für Medizinische Immunologie
der Medizinischen Fakultät Charité – Universitätsmedizin Berlin

DISSERTATION

Mechanismus der Hemmung der entzündungsfördernden IFN-γ Produktion in Gedächtnis-T-Zellen

zur Erlangung des akademischen Grades
Doctor rerum medicinalium (Dr. rer. medic.)

vorgelegt der Medizinischen Fakultät
Charité – Universitätsmedizin Berlin

von

Dipl. Ing. Biotech. (FH) Sandra Naundorf

aus Rathenow

Datum der Promotion: 17.09.2021

Vorwort

Diese Dissertation fasst meine Untersuchungen zum Thema „Mechanismus der Hemmung der entzündungsfördernden IFN-γ Produktion in Gedächtnis-T-Zellen“ kumulativ zusammen. Ergebnisse meiner Dissertation wurden in folgenden Publikationen veröffentlicht.

1. Publikation

Naundorf S*, Schröder M*, Höflich C, Suman N, Volk HD, Grütz G. IL-10 interferes directly with TCR-induced IFN-gamma but not IL-17 production in memory T cells. Eur J Immunol. 2009;39:1066-77.

2. Publikation

Schottelius AJ, Zügel U, Döcke WD, Zollner TM, Röse L, Mengel A, Buchmann B, Becker A, Grütz G, **Naundorf S**, Friedrich A, Gaestel M, Asadullah K. The role of mitogen-activated protein kinase-activated protein kinase 2 in the p38/TNF-alpha pathway of systemic and cutaneous inflammation. J Invest Dermatol. 2010;130:481-91.

3. Publikation

Reismann D, Stefanowski J, Günther R, Rakhymzhan A, Matthys R, Nützi R, Zehentmeier S, Schmidt-Bleek K, Petkau G, Chang HD, **Naundorf S**, Winter Y, Melchers F, Duda G, Hauser AE, Niesner RA. Longitudinal intravital imaging of the femoral bone marrow reveals plasticity within marrow vasculature. Nat Commun. 2017;8:2153.

Inhaltsverzeichnis

1. ABSTRAKT 1

2. EINLEITUNG 4

2.1 Regulation der adaptiven Immunantwort durch Zytokine 4

2.2 Posttranskriptionelle Regulierung der Zytokinproduktion 5

2.3 Aufrechterhaltung von Gedächtnis-T-Zellen im Knochenmark 5

3. ZIEL 6

4. METHODIK 7

4.1 Anreicherung von TH-Subpopulationen 7

4.2 ELISA 7

4.3 Durchflusszytometrie 7

4.4 Quantitative Real-Time PCR 8

4.5 Aktivierung von Maus-Milzzellen 8

4.6 Analyse der Bewegungsaktivität von Mäusen 8

5. ERGEBNISSE 8

5.1 IL-10 interferiert direkt mit TCR-induziertem IFN-γ, jedoch nicht mit der IL-17-Produktion in Gedächtnis-T-Zellen – Publikation 1 8

5.1.1 IL-10 hemmt indirekt die IFN-γ- und IL-17-Produktion 8

5.1.2 IL-10 interferiert mit TCR-induziertem IFN-γ, jedoch nicht mit TCR-induziertem IL-17 in PBMCs 9

5.1.3 Die inhibitorische Wirkung von IL-10 auf die TCR-induzierte IFN-γ-Produktion ist IL-2 unabhängig 9

5.1.4 IL-10 hemmt die TCR-induzierte IFN-γ-Produktion unabhängig von APCs und Kostimulation 10

5.1.5 Die IL-10-Hemmung der TCR-induzierten IFN-γ-Produktion ist SHP-1 unabhängig 10

5.1.6 Verlust der inhibitorischen Wirkung von IL-10 in *in-vitro*-Kultur 11

5.1.7 TH17-Zellen zeigen eine intakte IL-10 Signaltransduktion 12

5.2 Die Rolle der MAPKAPK2 im p38/TNF-α-Weg der systemischen und kutanen Entzündung – Publikation 2 12

5.2.1 Vergleich der MK2-Abhängigkeit bei der TLR- und TCR-vermittelten Zytokinproduktion 12

5.3 Die Longitudinale intravitale Bildgebung des femoralen Knochenmarks veranschaulicht die Plastizität innerhalb des Gefäßsystems - Publikation 3 13

5.3.1 Einfluss des Mikroendoskops auf die Aktivität der Mäuse 13

6. DISKUSSION 13

6.1 IL-10 interferiert direkt mit TCR-induziertem IFN-γ, jedoch nicht mit der IL-17 Produktion in Gedächtnis-T-Zellen – Publikation 1 13

6.2 Die Rolle der MAPKAPK2 im p38/TNF-α-Weg der systemischen und kutanen Entzündung – Publikation 2 16
6.3 Die Longitudinale intravitale Bildgebung des femoralen Knochenmarks veranschaulicht die Plastizität innerhalb des Gefäßsystems– Publikation 3 17

7. LITERATURVERZEICHNIS 20

8. EIDESSTATTLICHE VERSICHERUNG 25

9. ANTEILSERKLÄRUNG 26

10. AUSGEWÄHLTE PUBLIKATIONEN 28

11. LEBENSLAUF 67

12. PUBLIKATIONSLISTE 68

13. DANKSAGUNG 69

1. Abstrakt

T-Helfer-(TH)Lymphozyten spielen eine zentrale Rolle bei der adaptiven Immunität und steuern über die Expression von Zytokinen die Immunantwort gegen pathogene Erreger. Interferon-γ (IFN-γ)-exprimierende TH1-Zellen und Interleukin-17 (IL-17)-exprimierende TH17-Zellen sind entzündungsfördernd wirkende Subpopulationen der TH-Lymphozyten und spielen eine bedeutsame Rolle bei der Pathogenese von chronischen Entzündungskrankheiten. Interleukin-10 (IL-10) ist ein wichtiges immunregulatorisches Zytokin, welches die Induktion TH-Zell-vermittelter Immunantworten – durch indirekte Wirkung auf Antigen-präsentierende Zellen (APC) – inhibiert. Therapeutische Studien mit IL-10 bei chronischen Entzündungen zeigten jedoch nur einen geringen Erfolg.

Daher wurde im Rahmen dieser Arbeit der direkte Effekt von IL-10 auf die IFN-γ- und IL-17-Expression in humanen TH-Lymphozyten im peripheren Blut untersucht. Hierbei sollte insbesondere analysiert werden, inwieweit IL-10 eine bereits etablierte Gedächtnis-T-Zellantwort hemmen kann.

Wir konnten nachweisen, dass IL-10 eine direkte hemmende Wirkung auf die T-Zell-Rezeptor-vermittelte IFN-γ-Produktion in CD4-positiven T-Zellen, wie CD45RO-positiven-Gedächtnis-T-Zellen und in CD28-negativen Effektor-Gedächtnis-T-Zellen, hat. Dieser Effekt war unabhängig von Haupthistokompatibilitätskomplex (MHC)-II-exprimierenden APCs. Wir konnten auch beobachten, dass die IFN-γ-Inhibierung unabhängig von bereits beschriebenen Wirkungen von IL-10 auf TH-Lymphozyten - wie die Hemmung der Proliferation oder die Inhibierung des CD28-Signalweges - war. Im Gegensatz dazu beeinflusste IL-10 die T-Zell-Rezeptor-induzierte IL-17-Expression in TH-Lymphozyten trotz intakter IL-10-Signaltransduktion nicht. Die Ergebnisse unserer Studie legen nahe, dass IL-10 unterschiedliche Wirkungen auf verschiedene TH-Zell-Subpopulationen aufweist. Dies könnte möglicherweise erklären, warum IL-10 bei der Therapie TH17-vermittelter chronischer Entzündungserkrankungen wenig Wirkung zeigt.

Weiterführend wurde der Einfluss von der Mitogen-aktivierten Proteinkinase-aktivierte Proteinkinase 2 (MK2) – eine nachgeschaltete Kinase von p38 – welche die Expression entzündungsfördernder Zytokine reguliert, in verschiedenen Entzündungsmodellen der Haut untersucht. Wir konnten *in-vitro* darlegen, dass die Produktion des entzündungsfördernden Zytokins Tumornekrosefaktor-α nach Stimulation des Toll-like-Rezeptors in MK2-defizienten Milzzellen inhibiert war. Im Gegensatz dazu zeigte die Aktivierung des T-Zell-Rezeptors keine Beeinträchtigung in der Zytokinproduktion. Diese Beobachtungen implizieren, dass der Erfolg einer MK2-inhibierenden Therapie bei T-Zell-abhängigen Entzündungserkrankungen eingeschränkt sein kann.

Des Weiteren entwickelten wir eine neuartige mikroendoskopische Methode, bei der Gewebebereiche im tiefen Knochenmark lebender Mäuse über einen langen Zeitraum

analysiert werden können. Das Knochenmark ist ein wichtiger Ort für die Aufrechterhaltung von Gedächtnis-T-Lymphozyten. Mit Hilfe der intravitalen Multiphotonen-Mikroskopie konnten wir eine strukturelle Plastizität der Blutgefäße und eine zelluläre Dynamik während der Gewebehomöostase beobachten. Die kontinuierliche Reorganisation der Knochenmarkgefäße deutet darauf hin, dass das benötigte Blutgefäßnetz für die Migration von Zellen und die Versorgung langlebiger Gedächtniszellen, variable und anpassungsfähige Merkmale aufweisen. Diese neue Methode eröffnet unter anderem die Möglichkeit, die Überlebensfaktoren, die zur Aufrechterhaltung des immunologischen Gedächtnisses beitragen, zu charakterisieren.

Abstract

T helper (Th) lymphocytes play a central role in adaptive immunity and control the immune response against pathogens by the expression of cytokines. Interferon-γ (IFN-γ)-expressing Th1 cells and interleukin-17 (IL-17)-expressing Th17 cells are pro-inflammatory subpopulations of Th lymphocytes and play a significant role in the pathogenesis of chronic inflammatory diseases. Interleukin-10 (IL-10) is an important immunoregulatory cytokine that inhibits the induction of T cell-mediated immune responses through indirect effects on antigen-presenting cells (APC). However, therapeutic trials with IL-10 to dampen an ongoing chronic inflammation have been largely disappointing.

Therefore, the direct effect of IL-10 on IFN-γ- and IL-17 expression in human Th lymphocytes in peripheral blood was investigated in this study. In particular, we wanted to analyze whether IL-10 is able to inhibit an already established memory T cell response.

We could demonstrate that IL-10 has a direct inhibitory effect on T cell receptor-mediated IFN-γ production in CD4 positive T cells, such as CD45RO positive memory T cells and CD28 negative effector memory T cells. This effect was independent of major histocompatibility complex (MHC) class-II-expressing APCs. We furthermore showed that inhibition of IFN-γ production was independent of previously described effects of IL-10 on Th lymphocytes, such as inhibition of T cell proliferation and inhibition of CD28-signaling. In contrast, IL-10 did not affect T cell receptor-induced IL-17 expression in Th lymphocytes despite an intact IL-10-signaling pathway. The results of our study suggest that IL-10 has different effects on different Th cell subpopulations. This may explain that IL-10 has its limitation in inhibiting an already established Th17-mediated chronic inflammation.

Further, the influence of mitogen-activated protein-kinase-activated protein-kinase 2 (MK2) - a downstream kinase of p38 - which regulates the expression of pro-inflammatory cytokines, was investigated in different inflammatory skin models. We could demonstrate *in-vitro* that production of the pro-inflammatory cytokine tumor necrosis factor-α in MK2-deficient spleencells was strongly diminished after toll-like receptor stimulation. In contrast, activation of T cell

receptor did not show any impairment in cytokine production. These observations imply that the success of MK2-inhibiting therapy in T cell-dependent inflammatory diseases may be limited.

Furthermore, we developed a novel microendoscopic method to analyze tissue areas in deep bone marrow of living mice over a long period of time. The bone marrow is an important site for the maintenance of memory Th lymphocytes. Using intravital multiphoton microscopy, we observed structural plasticity of blood vessels and cellular dynamics during tissue homeostasis. The continuous reorganization of the bone marrow vessels indicates that the blood vessel network required for cell migration and the supply of long-lived memory cells has variable and adaptive characteristics. This new method opens the possibility to characterize survival factors that contribute to the maintenance of immunological memory.

2. Einleitung

2.1 Regulation der adaptiven Immunantwort durch Zytokine

T Helfer (TH)-Zellen sind aufgrund ihrer Expression von Zytokinen zentrale Regulatoren adaptiver Immunantworten. Die Zytokine dienen als Mediatoren, um andere Zellen des Immunsystems für die Immunreaktion zu aktivieren. Die richtige Balance von entzündungsfördernden und entzündungshemmenden Zytokinen ist essentiell für eine adäquate Immunantwort auf pathogene Erreger und deren Eliminierung. Eine Dysregulation dieser Balance kann zu chronischen Entzündungskrankheiten, wie rheumatoide Arthritis, Psoriasis, Multiple Sklerose, Morbus Crohn oder Colitis ulcerosa, führen.

TH1- und TH17-Zellen, Subpopulationen der CD4-positiven T-Zellen, sezernieren die entzündungsfördernden Effektorzytokine Interferon-γ (IFN-γ) und Interleukin-17 (IL-17) und spielen eine wichtige Rolle bei der Pathogenese verschiedener entzündlicher Erkrankungen (1; 2). TH1-Zellen induzieren effektive Immunantworten gegen intrazelluläre Pathogene, TH17-Zellen gegen extrazelluläre Bakterien und Pilze (3). Neue Erkenntnisse deuten auf die Heterogenität und Plastizität von TH17-Zellen hin. Abhängig von der Mikroumgebung können TH17 Zellen in TH1 Zellen transdifferenzieren und koexprimieren sowohl IL-17 als auch IFN-γ (4). Diese TH17/TH1 Zellen sind mit einer höheren Pathogenität im Vergleich zu TH17 Zellen verbunden und stehen im Zusammenhang mit der Induktion von Autoimmunität (5; 6; 7).

IL-10 besitzt aufgrund seiner entzündungshemmenden und immunsuppressiven Eigenschaften eine herausragende Rolle in der Immunregulation. IL-10 ist ein starkes immunregulatorisches Zytokin und spielt eine herausragende Rolle bei der Begrenzung der Entwicklung von chronischen Entzündungen. IL-10-Defizienz in Mäusen führt zu einer spontanen Entwicklung einer chronischen Kolitis, die durch eine unkontrollierte Aktivierung von CD4-positiven T-Zellen getrieben wird (8). Die immunsuppressive Funktion von IL-10 auf T-Zellen wird vorwiegend indirekt vermittelt, indem es auf die Antigen-präsentierenden Zellen (APC) einwirkt. IL-10 beeinflusst die Sekretion von entzündungsfördernden Mediatoren (9; 10; 11) und reduziert die Oberflächenexpression des MHC (Haupthisto-kompatibilitätskomplex)-Klasse-II-Komplexes und der kostimulatorischen Moleküle CD80/CD86 (12; 13; 14) und hemmt so die Aktivierung der T-Zellen.

Aufgrund der starken entzündungshemmenden Wirkung von IL-10 wurde es in einigen Humanstudien zur Therapie von chronisch entzündlichen Erkrankungen eingesetzt, von denen angenommen wurde, dass diese Erkrankungen auf eine IL-12 vermittelte TH1-Immunantwort, zurückzuführen sind. Es zeigte sich aber kaum eine Verbesserung der Krankheitssymtome, verglichen mit anderen Biologika, wie z.B. der anti- Tumornekrosefaktor-α (TNF-α)-Therapie. Lediglich bei der Psoriasis konnte eine Verbesserung festgestellt werden (15). In experimentellen Studien mit Tiermodellen für chronische Darmentzündungen zeigte IL-10 eine

hemmende Wirkung auf die Induktion einer entzündlichen Immunantwort, jedoch nicht auf eine etablierte chronische Entzündung (16; 17).
Wie genau die Inhibierung auf molekularer Ebene vermittelt wird und ob alle TH-Zell-Subpopulationen gleichermaßen von IL-10 betroffen sind ist bisher nicht vollständig aufgeklärt.

2.2 Posttranskriptionelle Regulierung der Zytokinproduktion

IL-10 reguliert auf molekularer Ebene eine Vielzahl von entzündlichen Zytokinen hauptsächlich posttranskriptionell durch mRNA-Stabilisierung (18). Die Stabilität und Translation der mRNA von Zytokinen wird durch Adenin/Uridin-reiche Elemente (AREs) innerhalb der 3´-untranslatierten Region (3´UTR) vermittelt (22). Der Signalweg, über den die AREs der mRNAs kontrolliert werden, ist der p38 Mitogen-aktivierte Proteinkinase (p38MAPK) Weg. MAPK-aktivierte Proteinkinase 2 (MK2) ist eine nachgeschaltete Serin-Threonin-Kinase von p38 und wird unter Stress und Entzündungsreiz aktiviert. Es wurde gezeigt, dass MK2 eine direkte und wesentliche Komponente bei der Regulierung der Biosynthese von entzündungsfördernden Zytokinen ist. In MK2-defizienten Mäusen zeigte die Lipopolysaccharid (LPS)-induzierte Produktion eine Reduktion der entzündungsfördernden Zytokine TNF-α und IL-6 und einer damit verbundenen erhöhten Resistenz gegen Endotoxin und Kollagen-induzierter Arthritis (19; 20; 21).
Aufgrund seiner zentralen Rolle wurde p38 als molekulares Ziel für die Hemmung chronischer Entzündungen eingehend untersucht. Die pharmakologische Blockade hemmte zwar die Produktion einiger entzündungsfördernder Zytokine, war aber aufgrund schwerwiegender Nebenwirkungen, nicht erfolgreich (22). Aus diesem Grunde ist MK2 ein vielversprechender Ansatz als Angriffspunkt für pharmakologische Interventionen (23; 24).

2.3 Aufrechterhaltung von Gedächtnis-T-Zellen im Knochenmark

Ein wichtiges Merkmal des adaptiven Immunsystems beruht auf der Fähigkeit des immunologischen Gedächtnisses, welches bei wiederholtem Kontakt mit dem gleichen Antigen eine schnellere und effizientere Immunantwort erzeugt (25). Das nach der ersten Antigen-Begegnung erzeugte Gedächtnis kann Jahrzehnte andauern und bietet einen lang anhaltenden Immunschutz gegen wiederholt auftretende Krankheitserreger (26). Antigen-spezifische CD4-positive Gedächtnis-T-Zellen vermitteln die Immunität und befinden sich hauptsächlich im Knochenmark (27). Nach Exposition mit dem entsprechenden Antigen durch APCs werden sie schnell reaktiviert und exprimieren ihre Effektorzytokine. Für die Aufrechterhaltung des T-Zell-Gedächtnisses sind Überlebensnischen innerhalb des Knochenmarks notwendig. Es wurde gezeigt, dass Gedächtnis-T-Zellen in Bezug auf Proliferation, Transkription und Migration in Nischen ruhen, die von Stromazellen zur Verfügung gestellt werden (27; 28). Die Faktoren, die die Langlebigkeit fördern und wie diese Nischen reguliert werden, sind jedoch nicht vollständig aufgeklärt.

Neuartige bildgebende in vivo Technologien ermöglichen unter physiologischen und pathologischen Bedingungen einen Einblick in das Gefäßsystem des Knochenmarks. Dieses ist für die Zufuhr von Sauerstoff, Nährstoffen und Überlebensfaktoren verantwortlich (29) und reguliert somit die Mikroumgebung der Überlebensnischen von Immunzellen und das Migrationsverhalten von Zellen in oder aus dem Knochenmark.

3. Ziel

TH-Zellen vermitteln protektive Immunität gegen pathogene Erreger. Bei einer Fehlregulation der Immunreaktion können sie aber zur Induktion und Aufrechterhaltung chronischer Entzündungen beitragen.
In der vorliegenden Arbeit sollen folgende Aspekte untersucht werden.

(1) Anhand von humanen mononukleären Zellen des peripheren Blutes soll *in-vitro* die entzündungshemmende Wirkung des Zytokins IL-10 auf verschiedene TH-Zell-Subpopulationen in Bezug auf die TCR-induzierte Produktion der entzündungsfördernden Zytokine IFN-γ und IL-17 analysiert werden. Dabei soll geklärt werden, ob IL-10 eine direkte Wirkung auf T-Zellen hat und inwieweit IL-10 eine bereits etablierte Gedächtnis-T-Zellantwort hemmen kann.

(2) Weiterführend soll die Rolle der Proteinkinase MK2 bei der TCR-vermittelten Zytokinproduktion anhand von MK2-defizienten Mäusen untersucht werden.

(3) Abschließend soll eine mikroendoskopische Methode entwickelt werden, die eine zelluläre Langzeitbeobachtung im tiefen Knochenmark, dem zentralen Ort der Gedächtnis-T-Zellen, in lebenden Mäusen ermöglicht.

4. Methodik

4.1 Anreicherung von TH-Subpopulationen

Mononukleäre Zellen des peripheren Blutes (PBMCs) wurden durch Ficoll-Dichtegradienten-zentrifugation aus dem Blut von gesunden, freiwilligen Spendern isoliert und anschließend durch magnetische Zellsortierung (MACS, Miltenyi Biotec, Deutschland) separiert. Für die Isolierung von CD4+ T-Zellen wurden zunächst CD14+ Zellen depletiert und anschliessend CD4+ Zellen separiert. Dieses Verfahren ergab eine Population von CD4+ T-Zellen mit einer Reinheit von durchschnittlich 99%. Gedächtnis-T-Zellen wurden nach der CD4+ T-Zell-Separation anschließend anhand des Markers CD45RO+ isoliert. CD28- Zellen wurden isoliert, indem zuerst CD14+ Zellen und im Anschluss CD28+ depletiert wurden. Die Isolierung von IL-23 Rezeptor+ Zellen erfolgte nach CD14-Depletion.

4.2 ELISA

Zur Quantifizierung von Zytokinen nach Zellstimulation in Zellkulturüberständen wurde die *Enzyme-Linked Immunosorbent Assay* (ELISA)- Technik verwendet. Für die Bestimmung von humanem IFN-γ und IL-17 wurden kommerzielle ELISA-Kits (R&D) verwendet. Die Durchführung erfolgte anhand des Herstellerprotokolls.

4.3 Durchflusszytometrie

Nach Beendigung der Stimulation wurden Einzelzellsuspensionen mit fluoreszenz-gekoppelten Antikörpern, die gegen spezifische Zelloberflächenantigene gerichtet sind markiert und am Durchflusszytometer analysiert. Die Messung wurde am BD FACSCalibur (BD) durchgeführt und mit der CellQuest (BD) Software ausgewertet.

Um die intrazelluläre Zytokinproduktion (IFN-γ und IL-17) der TH-Zellen zu analysieren, wurde während der Zellstimulation die Sekretion der Zytokine mit Brefeldin A gehemmt, so dass die Zytokine in den Zellen akkumulierten. Im Anschluss wurde die Zelloberfläche mit Antikörpern markiert, dann die Zellen fixiert und die Zellmembran permeabilisiert. Daraufhin wurden die intrazellulären Zytokine mit fluoreszenz-markierten Antikörpern angefärbt und analysiert.

Der Nachweis der STAT3- und STAT1-Phosphorylierung erfolgte nach 20-minütiger Zellstimulation, anschließender Zellfixierung und Zellpermeabilisierung sowie die Anfärbung mit phospho-spezifischen Antikörpern.

Die Analyse proliferierender TH-Zellen erfolgte mittels CFSE-Färbung. Carboxyfluoreszein Diazetat Succinimidyl Ester (CFDA-SE) ist ein membrangängiger Farbstoff. Intrazelluläre Esterasen in lebenden Zellen spalten die Acetatgruppen und erzeugen ein Molekül mit grüner Fluoreszenz (CFSE), welches kovalent an freie Amine zytoplasmatischer Proteine bindet und dadurch membranundurchlässig ist. Die Farbstoffmenge wird pro Zellteilung zur Hälfte an die Tochterzellen weitergegeben.

4.4 Quantitative Real-Time PCR

Für die Analyse der Genexpression von humanen IFN-γ, IL-17 und SOCS-3 in PBMCs oder CD4+T-Zellen wurde die RNA mit Hilfe des absolut-RNA-RT-PCR Isolations-Kit (Stratagene) isoliert. Anschließend wurde die isolierte RNA mit der MLV Reverse Transcriptase (Gibco) in cDNA transkribiert. Die quantitative Analyse der Genexpression in Echtzeit erfolgte unter Verwendung des Sequence Detectors (ABI PRISM 7700 Sequence Detectors, Applied Biosystems). Primer Express Version 1.0 diente der Identifizierung von genspezifischen Primer und Sonden. Die Sonden wurden mit dem Reporterfarbstoff FAM (6-carboxyfluorescin) am 5'-Ende und dem Quencher TAMRA (6-carboxy-tetramethyl-rhodamine) am 3'-Ende markiert. Als Referenzgen dient ein konstitutiv exprimiertes sogenanntes *Housekeeping-Gen* (HPRT).

Dadurch können quantitative Aussagen zur Expression des zu untersuchenden Gens in verschiedenen Proben getroffen werden.

4.5 Aktivierung von Maus-Milzzellen

Isolierte Milzzellen von C57BL/6 Wildtyp- oder MK2-defizienten (Mapkapk2^{tm1Mgl}) Mäusen wurden mit dem bakteriellen Lipopolysaccharid (LPS), Zymosan, Imiquimod oder CpG-Oligonukleotide stimuliert. Als Kontrolle wurden Milzzellen von Wildtyp-Mäusen mit dem spezifischen p38 MAP-Kinase Inhibitor SB203580 oder SB220025 behandelt. Separierte CD4+ T-Zellen aus der Milz wurden mit Antikörpern gegen CD3 und CD28 aktiviert.

4.6 Analyse der Bewegungsaktivität von Mäusen

Die Messung der Aktivität der Mäuse (C57BL/6) nach dem chirurgischen Eingriff für die Implantation des Mikroendoskops am Mausfemur, erfolgte mit Hilfe der RFID-Technologie (Radio Frequency Identification). 3 Tage vor der Operation erhielten die Tiere subkutan biokompatible RFID-Transponder. Ein Sensorplattensystem (Phenosys, Berlin, Deutschland), welches sich unterhalb des normalen Heimkäfig befindet, zeichnete das Laufverhalten auf. Die Haltung der Mäuse mit Implantat und der Kontrollmäuse -die eine Scheinbehandlung erhielten- erfolgte während der gesamten Zeit in einem gemeinsamen Käfig. Dadurch ist eine automatisierte Überwachung einzelner Mäuse, innerhalb der etablierten Gruppe über einen langen Zeitraum möglich. Die Aktivität wurde bis 18 Tage nach der Operation aufgezeichnet. Die durchschnittliche tägliche Aktivität jedes Individuums in den drei Tagen vor der Operation wurde verwendet, um die Daten zu normalisieren.

5. Ergebnisse

Im Folgenden werden die Ergebnisse der beiliegenden Publikationen 1-3 dargestellt.

5.1 IL-10 interferiert direkt mit TCR-induziertem IFN-γ, jedoch nicht mit der IL-17-Produktion in Gedächtnis-T-Zellen – Publikation 1

Das Ziel dieser Publikation war es, zu analysieren, ob IL-10 eine direkte entzündungshemmende Wirkung -hinsichtlich der TCR-induzierten Zytokinproduktion- auf die entzündungsfördernden Zytokine IFN-γ und IL-17 hat. Dabei sollte insbesondere analysiert werden, inwieweit IL-10 eine bereits etablierte Gedächtnis-T-Zellantwort hemmen kann.

5.1.1 IL-10 hemmt indirekt die IFN-γ- und IL-17-Produktion

IL-10 hemmt indirekt die Produktion eines breiten Spektrums von TH-Zell-Zytokinen, indem es die Antigenpräsentation und die durch APCs vermittelte Kostimulation vermindert.

Wir konnten bestätigen, dass IL-10, nach Stimulation von PBMCs mit dem fungalen Antigen *Candida albicans*, die Expression von IFN-γ und IL-17 signifikant hemmen konnte. Unter diesen Bedingungen kann IL-10 seine Hemmwirkung auf APCs und T-Zellen ausüben. Die inhibitorische Wirkung von IL-10 auf die antigen-induzierte IFN-γ-Produktion war jedoch signifikant stärker als auf die Produktion von IL-17 [Publikation 1 (30), Abbildung 1 A].

5.1.2 IL-10 interferiert mit TCR-induziertem IFN-γ, jedoch nicht mit TCR-induziertem IL-17 in PBMCs

TH-Zellen, welche bereits durch einen initialen Stimulus aktiviert wurden, exprimieren nach Reaktivierung die gleichen Zytokine, die sie während ihrer ersten Aktivierung exprimiert haben. Diese Gedächtnis-T-Zellen reagieren direkt auf einen Zytokinstimulus oder durch Stimulation des T-Zell-Rezeptors (TCR) und produzieren innerhalb von 24h Effektorzytokine. Die Stimulation der PBMCs erfolgte mit Antikörpern gegen CD3 und CD28. IL-10 inhibierte signifikant die TCR-induzierte IFN-γ-Produktion im Zellkulturüberstand, es hatte jedoch nur einen schwachen und nicht signifikanten hemmenden Effekt auf die IL-17-Produktion. Diese Beobachtungen konnten auf mRNA-Ebene durch Messung der Genexpression und auf Einzelzellebene durch intrazelluläre Färbung bestätigt werden [Publikation 1 (30), Abbildung 1 C, D]. Als Reaktion auf die Stimulationsbedingungen produzierten CD4-positive- und CD8-positive T-Zellen IFN-γ sowie IL-17. IL-10 reduzierte den Prozentsatz und die mittlere Fluoreszenzintensität von IFN-γ-produzierenden T-Zellen, d.h. die Menge an IFN-γ pro Zelle, beeinflusste jedoch nicht IL-17-produzierende T-Zellen.

5.1.3 Die inhibitorische Wirkung von IL-10 auf die TCR-induzierte IFN-γ-Produktion ist IL-2 unabhängig

Da T-Zellen den IL-10 Rezeptor exprimieren, wurden auch einige inhibitorische Wirkungen von IL-10 auf naive T-Zellen beschrieben. IL-10 soll direkt auf naive T-Zellen wirken, indem es möglicherweise die IL-2-Produktion inhibiert (31). IL-2 ist ein wichtiger Kofaktor für die T-Zell-Proliferation und die IFN-γ-Produktion, indem es den mRNA-Transport und -Translation ermöglicht (32). Nach Aktivierung exprimiert die T-Zelle IL-2, welches autokrin die Proliferation von aktivierten T-Zellen fördert (33). Wir konnten bestätigen, dass das Vorhandensein von exogenem IL-2 die antiproliferative Wirkung von IL-10 auf T-Zellen aufhob. Im Gegensatz dazu wurde der hemmende Effekt von IL-10 auf die IFN-γ-Produktion nicht beeinflusst. Demgegenüber hatte die Zugabe von IL-2 - in Gegenwart oder Abwesenheit von IL-10 - keine Auswirkungen auf die IL-17-Produktion [Publikation 1 (30), Abbildung 2]. Diese Ergebnisse deuten auf eine direkte Wirkung von IL-10 auf IFN-γ hin, welche unabhängig von der IL-2 Repression ist.

5.1.4 IL-10 hemmt die TCR-induzierte IFN-γ-Produktion unabhängig von APCs und Kostimulation

In einer vorherigen Publikation haben wir gezeigt, dass der inhibitorische Effekt von IL-10 auf die durch Zytokine (IL-12/IL-18) induzierte IFN-γ-Produktion in T-Zellen von CD14-positiven APCs abhängig ist (34). Um die durch APCs vermittelte IL-10 Hemmung auszuschließen, wurden CD14-positive Monozyten und Makrophagen aus PBMCs depletiert und anschließend CD4-positive T-Zellen separiert. IL-10 inhibierte immer noch signifikant die TCR-induzierte IFN-γ-Produktion, obwohl der Effekt weniger ausgeprägt war als bei nur CD14-depletierten PBMCs [Publikation 1 (30), Abbildung 3 A]. Das ist darauf zurückzuführen, dass noch ein geringer Anteil an APCs in der *in-vitro* Kultur vorhanden ist.

Im Gegensatz zu naiven T-Zellen benötigen T-Zellen nach Antigenkontakt mit APCs keine Kostimulation für die erneute Aktivierung. Durch die Stimulation des TCR mit CD3 Antikörpern produzieren nur Gedächtnis-T-Zellen ihre Effektorzytokine. Wir konnten beobachten, dass IL-10 die CD3-induzierte IFN-γ-Produktion in PBMCs, CD14-depletierten PBMCs und CD45RO+ Gedächtnis-T-Zellen inhibieren konnte. Der gleiche Effekt konnte bei der CD3/CD28 Antikörper-induzierten IFN-γ-Produktion festgestellt werden. IL-10 zeigte jedoch keine Wirkung auf die CD3-induzierte IL-17-Produktion [Publikation 1 (30), Abbildung 3 B].

Naive und zentrale Gedächtnis-T-Zellen exprimieren CD28. In Effektor-Gedächtnis- und Effektor-T-Zellen (35) wird CD28 herunterreguliert. Es wurde postuliert, dass die inhibitorische Wirkung von IL-10 auf T-Zellen durch die Inhibierung der Tyrosinphosphorylierung von CD28 vermittelt wird (36). Das impliziert, dass nur CD28-positive T-Zellen durch IL-10 inhibiert werden können. Um dies zu ermitteln, wurden CD28-negative- und CD28-positive T-Zellen von CD14-depletierten PBMCs separiert und mit CD3/ CD28 Antikörpern inkubiert. Sowohl CD28-negative- als auch CD28-positive T-Zellen produzierten eine signifikante Menge an IFN-γ, welches durch IL-10 inhibiert wurde [Publikation 1 (30), Abbildung 4].

Die zusätzliche Markierung exprimierter Aktivierungsmarker auf Gedächtnis- und Effektor-T-Zellen (wie CD25 und HLA-DR) konnte ebenfalls die hemmende Wirkung von IL-10 auf die IFN-γ-Produktion bestätigen [Publikation 1 (30)].

5.1.5 Die IL-10-Hemmung der TCR-induzierten IFN-γ-Produktion ist SHP-1 unabhängig

Die Tyrosin-Phosphorylierung von Proteinen stellt einen zentralen Mechanismus bei der T-Zell-Aktivierung nach Bindung des Antigens dar. In einer Studie wurde vermutet, dass die transiente Aktivierung der Tyrosinphosphatase SHP-1 die inhibitorische Wirkung von IL-10 auf die CD28- oder ICOS-induzierte T-Zellproliferation vermittelt (37). Da SHP-1 an der negativen Regulation der T-Zell-Aktivierung beteiligt ist, würde es naheliegen, dass es auch eine Rolle bei der Hemmung der TCR-induzierten IFN-γ-Produktion durch IL-10 spielt. Die Inhibierung von SHP-1 durch den spezifischen, irreversiblen Inhibitor Natriumstibogluconat (38), überwand jedoch nicht

die Wirkung von IL-10 auf die TCR-induzierte IFN-γ-Produktion. Dies war der Fall bei der TCR-Stimulation mit CD3 Antikörpern allein sowie bei zusätzlicher Kostimulation mit CD28 Antikörpern. Selbst höhere Konzentrationen von Natriumstibogluconat (50 µg/ml) hoben die IL-10-Hemmwirkung nicht auf [Publikation 1 (30), Abbildung 5]. Um die Aktivität des Inhibitors bei der verwendeten Konzentration und Zeit zu kontrollieren, wurde die durch IFN-α-induzierte STAT-1-Aktivierung in T-Zellen gemessen.
Diese Daten legen nahe, dass IL-10 einen SHP-1-unabhängigen Mechanismus zur Hemmung der TCR-induzierten IFN-γ-Produktion verwendet [Publikation 1 (30)].

5.1.6 Verlust der inhibitorischen Wirkung von IL-10 in *in-vitro*-Kultur

Als nächstes untersuchten wir, ob kürzlich oder dauerhaft aktivierte Gedächtnis-T-Zellen, die bei einer akuten Infektion oder einer chronischen Entzündung auftreten für die inhibitorische Wirkung von IL-10 auf die IFN-γ-Produktion empfänglich sind. Es wurde vermutet, dass die IL-10-Rezeptor Expression nach der TCR-Aktivierung herunterreguliert wird, was zu einem Verlust der IL-10-Reaktionsfähigkeit in kürzlich aktivierten Gedächtnis-T-Zellen führen würde (39). Für diese Analyse haben wir PBMCs für 48 Stunden in Gegenwart von CD3/CD28 Antikörpern und IL-2 voraktiviert, um anschließend den Einfluss von IL-10 auf die IFN-γ-Produktion nach der Restimulation mit CD3/CD28 Antikörpern zu untersuchen. In Übereinstimmung mit anderen Berichten beobachteten wir keinen hemmenden Effekt von IL-10 auf die IFN-γ-Produktion [Publikation 1 (30), Abbildung 6 A]. Überraschenderweise verloren auch T-Zellen, welche ohne Voraktivierung *in-vitro* kultiviert wurden, ihre Reaktionsfähigkeit gegenüber IL-10. Dies führte uns zu dem Schluss, dass die Unempfindlichkeit gegenüber der inhibitorischen Wirkung von IL-10 auf frisch voraktivierte T-Zellen eher ein *in-vitro*-Kultur-Artefakt als eine stimulationsinduzierte Wirkung ist [Publikation 1 (30)].
Der durch IL-10 aktivierte Transkriptionsfaktor STAT3 (signal transducer and activator of transcription 3) ist essentiell für die entzündungshemmende Wirkung von IL-10 in T-Zellen. Die Bindung von IL-10 an den IL-10 Rezeptor induziert die STAT3-Phosphorylierung (40) und bewirkt die Expression von Zielgenen wie SOCS3 (suppressor of cytokine signaling 3). SOCS3 wiederum vermittelt die entzündungshemmende Wirkung von IL-10 und unterbindet die Signalweiterleitung für die Expression entzündungsfördernder Zytokine (41).
Trotz des Ausbleibens einer Wirkung von IL-10 auf die IFN-γ-Produktion induzierte IL-10 in *in-vitro* voraktivierte T-Zellen die STAT3-Phosphorylierung und die Expression von SOCS3 [Publikation 1 (30), Abbildung 6 B]. Das zeigt, dass die IL-10-vermittelte Signaltransduktion in aktivierten Gedächtnis-T-Zellen intakt ist.

5.1.7 TH17-Zellen zeigen eine intakte IL-10 Signaltransduktion

Da wir eine inhibitorische Wirkung von IL-10 auf die IFN-γ-, jedoch nicht auf die IL-17-Produktion in frisch isolierten, antigen-erfahrenen TH-Zellen beobachten konnten, untersuchten wir im nächsten Schritt, ob TH17-Zellen eine aktive IL-10-Signalübertragung besitzen. TH17-Zellen wurden anhand der Expression des IL-23 Rezeptors und den Chemokinrezeptoren CCR4 und CCR6 identifiziert (42). Überraschenderweise wiesen TH17-Zellen nach IL-10-Stimulation eine normale STAT3-Aktivierung auf. Ebenso konnte in angereicherten IL-23-Rezeptor positiven TH-Zellen die Expression von SOCS-3 nachgewiesen werden. Diese Ergebnisse zeigen, dass TH17-Zellen im vollen Umfang auf IL-10 reagieren, allerdings führt es nicht zu einer Hemmung der IL-17-Produktion [Publikation 1 (30), Abbildung 7].

5.2 Die Rolle der MAPKAPK2 im p38/TNF-α-Weg der systemischen und kutanen Entzündung – Publikation 2

Das Ziel dieser Publikation war es, zu bestimmen, ob MK2 ein vielversprechendes Wirkstoffziel für die Behandlung entzündlicher Hauterkrankungen darstellt.

5.2.1 Vergleich der MK2-Abhängigkeit bei der TLR- und TCR-vermittelten Zytokinproduktion

Die Funktion der Kinase MK2 wurde in verschiedenen Entzündungsmodellen der Haut in MK2-defizienten- und Wildtyp-Mäusen analysiert. Die MK2-Defizienz führte dabei zu unterschiedlichen Auswirkungen.

Für ein besseres Verständnis der beobachteten unterschiedlichen *in-vivo*-Effekte, wollten wir die Rolle von MK2 für die Produktion von TNF-α *in-vitro* weiter untersuchen. Die Stimulation verschiedener Toll-like-Rezeptoren (TLR) mit ihren jeweiligen Liganden (LPS, Zymosan, Imiquimod, CpG) führte in Wildtyp-Milzzellen zu einer starken Induktion von TNF-α, die in MK2-defizienten Milzzellen signifikant reduziert wurde. Diese Ergebnisse stimmen mit den Beobachtungen aus dem Modell der LPS-induzierten systemischen Entzündung überein (19). Darüber hinaus zeigte die TNF-α-Produktion in Wildtyp-Milzzellen nach Inhibierung mit dem spezifischen p38 MAP-Kinase Inhibitor SB203580 oder SB220025 eine vergleichbare Hemmung wie in MK2-defizienten Milzzellen. Wir konnten allerdings keine signifikante Hemmung von TNF-α in isolierten MK2-defizienten CD4-positiven T-Zellen nach TCR-Stimulation beobachten [Publikation 2 (43), Abbildung 7].

Diese *in-vitro* Daten zeigen, dass MK2 eine zentrale Rolle bei der TLR-stimulierten Produktion von TNF-α in Milzzellen spielt - während die TCR-induzierte TNF-α Produktion in TH-Zellen weniger beeinträchtigt ist.

5.3 Die Longitudinale intravitale Bildgebung des femoralen Knochenmarks veranschaulicht die Plastizität innerhalb des Gefäßsystems - Publikation 3

Das Ziel dieser Publikation war es, eine neue mikroendoskopische Methode zu entwickeln, durch die eine wiederholte Bildgebung derselben Geweberegion im Knochenmark lebender Mäuse über einen langen Zeitraum ermöglicht wird.

5.3.1 Einfluss des Mikroendoskops auf die Aktivität der Mäuse

Mit Hilfe der longitudinalen intravitalen Multiphotonen-Mikroskopie konnten wir unter physiologischen Bedingungen Einblick in die Interaktionen im Knochenmark erhalten. Dafür wurde ein GRIN-Endoskop (Gradientenbrechungsindex) dauerhaft in der Knochenmarkhöhle am rechten Femur der Maus so installiert, dass mithilfe der Zwei-Photonen-Mikroskopie Gewebebereiche in unterschiedlicher Tiefe erfasst werden können. Um die Auswirkungen der Operation und der Implantation des Endoskopsystems auf das Bewegungsverhalten und die Schmerzsensitivität der Mäuse zu beurteilen, analysierten wir die Tiere mit Hilfe der RFID-Technologie (Radio Frequency Identification). Dieses System ermöglicht die Aufzeichnung von individuellen Aktivitätsprofilen über einen langen Zeitraum. Mäuse, die das Endoskop erhalten hatten und scheinbehandelte Mäuse wurden vor und nach der Operation in ihrem gemeinsamen Käfig überwacht. Innerhalb von 3 Tagen nach der Operation konnte in beiden Gruppen ein Abfall des mittleren Aktivitätsprofils im Vergleich zu dem präoperativen Niveau beobachtet werden. Am Tag 14 nach der Operation kehrte die Aktivität der Mäuse in beiden Gruppen auf das präoperative Niveau zurück, ebenso wie die klinische Bewertung des allgemeinen Erscheinungsbildes und das Verhalten der einzelnen Mäuse [Publikation 3 (44), Abbildung 2]. Es gab keine signifikanten Unterschiede zwischen den beiden Gruppen, weder in der frühen Phase (Tag 3) noch in der späteren Phase (Tag 14) nach der Operation.

6. Diskussion

6.1 IL-10 interferiert direkt mit TCR-induziertem IFN-γ, jedoch nicht mit der IL-17 Produktion in Gedächtnis-T-Zellen – Publikation 1

TH-Lymphozyten regulieren über die Expression von Zytokinen die Immunantwort. Die Zytokine koordinieren die Rekrutierung und Aktivierung anderer Zellen des Immunsystems. IFN-γ-produzierende TH1-Zellen und IL-17-produzierende TH17-Zellen besitzen neben der Pathogenabwehr eine pathologisch bedeutsame Rolle bei verschiedenen chronischen Entzündungen. IL-10 ist ein immunregulatorisches Zytokin, welches an der Begrenzung von Entzündungen beteiligt ist. Es beeinträchtigt die Induktion verschiedener proinflammatorischer Mediatoren sowie die Antigenpräsentation und hemmt dadurch indirekt die TH-Zellantwort (9; 10; 13). IL-10-Defizienz in Mäusen führt zur Entwicklung einer Kolitis, die durch eine

unkontrollierte Aktivierung von CD4+ T-Zellen durch die Darmflora verursacht wird (8). Aufgrund dieser Eigenschaften wurde IL-10 in therapeutischen Studien zur Behandlung chronisch-entzündlicher Erkrankungen eingesetzt, von denen angenommen wurde, dass sie auf eine übermäßige TH1-vermittelte Immunantwort zurückzuführen sind (15). Die Therapie mit IL-10 führte jedoch nicht zu signifikant höheren Remissionsraten oder zu einer klinischen Verbesserung im Vergleich zur Placebo-Behandlung - mit Ausnahme bei der Psoriasis (45). Die meisten klinischen Studien haben hemmende Wirkungen von IL-10 auf die Induktion einer entzündlichen Immunantwort beschrieben, jedoch nicht auf eine etablierte, andauernde Entzündung. Neuere Daten zeigen, dass die Produktion von IL-17 anstelle von IFN-γ mit der Pathologie von chronischen Entzündungen assoziiert ist (46; 47; 48). Bisher ist jedoch nicht ausreichend aufgeklärt, ob alle TH-Zell-Subpopulationen gleichermaßen von IL-10 betroffen sind und ob es eine direkte Wirkung von IL-10 auf TH-Zellen gibt.

Daher wollten wir untersuchen, ob IL-10 eine direkte Wirkung auf die TCR-vermittelte IFN-γ- und IL-17 Expression in humanen TH-Zellen hat und inwieweit IL-10 eine bereits etablierte Gedächtnis-T-Zellantwort hemmen kann.

TH-Zellen, welche bereits aktiviert wurden behalten ihre ursprüngliche Induktion und exprimieren die gleichen Zytokine, die sie während ihrer ersten Aktivierung exprimiert haben. Diese Gedächtnis-T-Zellen reagieren direkt durch Stimulation des T-Zell-Rezeptors, ohne Kostimulation und produzieren innerhalb von 24h ihre Effektorzytokine, da die epigenetische Prägung bereits etabliert ist (49; 50).

Wir konnten in unserer Arbeit zeigen, dass IL-10 eine direkte hemmende Wirkung auf TH-Zellen hinsichtlich der TCR-induzierten IFN-γ-Produktion hat [Publikation 1 (30)]. Im Gegensatz zu früheren Publikationen (36; 37) inhibierte IL-10 die durch CD3-Aktivierung (ohne Kostimulation) induzierte IFN-γ-Produktion. Dieser Effekt war unabhängig von MHC-II-exprimierenden APCs, was im Gegensatz zur Zytokin-induzierten IFN-γ-Produktion steht (34). In Übereinstimmung damit, konnten wir die hemmende Wirkung von IL-10 auch in isolierten CD45RO-positiven Gedächtnis-T-Zellen und in CD28-negativen Effektor-Gedächtnis-T-Zellen bestätigen. Interessanterweise konnten wir die inhibitorische Wirkung von IL-10 nur in frisch isolierten Gedächtnis-T-Zellen beobachten. In Zellkultur war dieser Effekt, trotz IL-10-induzierter STAT-3-Phosphorylierung und SOCS-3-Expression, nicht mehr nachweisbar.

Ein direkter inhibitorischer Effekt von IL-10 auf T-Zellen, der bisher beschrieben wurde, ist die Hemmung der T-Zell-Proliferation, die durch exogene Gabe von IL-2 aufhebbar ist (31). Wir konnten bestätigen, dass das Vorhandensein von IL-2 die antiproliferative Wirkung von IL-10 auf T-Zellen zwar aufhob, jedoch den hemmenden Effekt von IL-10 auf die IFN-γ-Produktion nicht beeinflusste [Publikation 1 (30)]. Eine weitere inhibitorische Wirkung von IL-10 auf T-Zellen soll über den CD28-Signalweg vermittelt werden (36). Wir beobachteten, dass der IL-10 Effekt unabhängig von der CD28-Signaltransduktion war, da sowohl in den CD28-positiven

Gedächtnis-T-Zellen als auch in den CD28-negativen Effektor-Gedächtnis-T-Zellen die Hemmung der IFN-γ-Produktion erhalten blieb. Des Weiteren wurde vermutet, dass die Aktivierung der Tyrosinphosphatase SHP-1 die inhibitorische Wirkung von IL-10 auf die CD28- oder ICOS-induzierte T-Zellproliferation vermittelt (37). Wir konnten jedoch demonstrieren, dass die Inhibierung von SHP-1 nicht die Wirkung von IL-10 auf die TCR-induzierte IFN-γ-Produktion beeinflusste. Unsere Daten legen nahe, dass IL-10 keinen der bisher beschriebenen Mechanismen zur Hemmung der TCR-induzierten IFN-γ-Produktion verwendet [Publikation 1 (30)].

Im Gegensatz zu IFN-γ wurde die TCR-induzierte IL-17-Produktion von IL-10 nicht beeinflusst. Interessanterweise reagierten TH17-Zellen auf die IL-10 Stimulation mit einer effektiven STAT-3 Aktivierung und SOCS-3 Expression. Wir konnten aber beobachten, dass nach Antigenpräsentation über APCs die IL-17-Produktion vermindert war, was auf die immunsuppressiven Eigenschaften von IL-10 auf die APCs zurückzuführen ist. Unsere Daten könnten möglicherweise erklären, warum die IL-10-Therapie kaum eine Wirkung bei einer TH17-vermittelten chronischen Entzündung zeigt [Publikation 1 (30)].

Es ist jedoch bekannt, dass IL-10 die Produktion der Hauptinduktoren einer TH17-Immunantwort und die Proliferation von TH17-Zellen unterdrücken kann (51). IL-10 hemmt die IL-6 Sekretion (9) und die Expression der IL-12p40 Untereinheit (11), die IL-12 und IL-23 gemeinsam haben (52). Die Blockade von IL-12p40 verhindert die Induktion von mehreren Autoimmunkrankheiten in Mäusen. Die Hemmung von IL-23p19 oder von IL-12p35 haben unterschiedliche Auswirkungen, was darauf hindeutet, dass IL-12 und IL-23 verschiedene pathogene Funktionen in Autoimmunmodellen haben (2). Im Gegensatz zu TH1-Zellen ist die epigenetische Stabilität von TH17-Zellen in Bezug auf die Expression von IL-17 teilweise instabil. Die *in-vitro* Stimulation mit IL-12 induziert in TH-17 Zellen die Produktion von IFN-γ, während gleichzeitig die IL-17 Expression verloren gehen kann (53). Im entzündeten Gewebe von Autoimmunpatienten wurden TH-Zellen identifiziert, die IFN-γ und IL-17 koexprimieren (4). Der gemischte TH1/TH17-Phänotyp wird scheinbar von der Art der Entzündung, dem umgebenden Zytokinmilieu und von zellulären Stimulationsfaktoren bestimmt.

Eine mögliche Erklärung warum die IL-10-Behandlung kaum einen therapeutischen Effekt zeigt könnte sein, dass IL-10-Protein verwendet wurde. Im Gegensatz zu humanisierten Antikörpern gegen Zytokine besitzt das Protein eine geringere Halbwertszeit. Dadurch ist die lokale Bioverfügbarkeit bei systemischer Verabreichung wesentlich eingeschränkter. In einer klinischen Studie wurde Patienten mit chronischer Darmentzündung IL-10 durch gentechnisch veränderte Bakterien verabreicht. Infolge der Erhöhung der lokalen Endkonzentration von IL-10 zeigte sich eine Verbesserung des klinischen Ansprechens und eine Verringerung der Nebenwirkungen der Patienten (54). Eine weitere Erklärung könnte sein, dass die immunstimulatorische Wirkung von IL-10 auf andere Immunzellen die immunsuppressiven

Eigenschaften ausgleichen. IL-10 fördert die humorale und die angeborene Immunantwort. Es erhöht die Proliferation, die Antikörperproduktion und die MHC-II-Expression in B-Zellen und steigert die Differenzierung zu Plasmazellen (55; 56). IL-10 wirkt stimulierend auf natürliche Killerzellen, indem es die IL-2-induzierte Zytokinproduktion von IFN-γ induziert (57) und es steigert die Zytotoxizität von T-Zellen (58). Es wäre auch wahrscheinlich, dass die Verabreichung von IL-10 alleine die Dysregulation der Vielzahl von entzündungsfördernden Mediatoren, die an der Aufrechterhaltung einer chronischen Entzündung beteiligt sind, nicht wirksam unterdrücken kann.

Zusammenfassend legen unsere Ergebnisse nahe, dass die IL-10-basierte Therapie für entzündliche Erkrankungen vielversprechend ist, die allein durch eine anhaltende übermäßige TH1 Reaktion verursacht werden [Publikation 1 (30)]. Im Gegensatz dazu ist die Fähigkeit von IL-10, eine durch TH17-Gedächtniszellen verursachte Entzündung einzudämmen, möglicherweise begrenzt. IL-10 kann jedoch die Induktion einer entzündlichen TH17-Immunantwort verhindern. Im Gegensatz zu TH1-Zellen weisen TH17-Zellen eine hohe Plastizität auf und können einen gemischten TH1/TH17-Phänotyp aufzeigen, welcher vom umgebenen Zytokinmilieu gefördert wird. Demzufolge wäre es möglich, IL-10 in Kombination mit IL-17- oder IL-23-neutralisierenden Antikörpern bzw. mit IL-17RA- oder IL-23R-Antikörpern einzusetzen, um eine bereits bestehende entzündliche Immunantwort einzudämmen.

6.2 Die Rolle der MAPKAPK2 im p38/TNF-α-Weg der systemischen und kutanen Entzündung – Publikation 2

Der p38 MAPK-Weg hat sich als zentraler Regulator von Entzündungen erwiesen (59). MK2, die Downstream-Kinase von p38, kontrolliert über die Stabilität der mRNA, wichtige entzündungsfördernde Zytokine wie TNF-α und IL-6 (19; 60). Beide Kinasen wurden daher als potenziell vielversprechende Wirkstoffziele für pharmakologische Interventionen identifiziert (24). Das Anvisieren von MK2 könnte Vorteile gegenüber p38 haben, da die pharmakologische Hemmung von p38 mit schwerwiegenden Nebenwirkungen verbunden ist (22). MK2-defiziente Mäuse zeigen eine signifikante Abnahme der LPS-induzierten Biosynthese von TNF-α (5) und sind somit resistent gegenüber einem Endotoxinschock. Die Relevanz von MK2 als Wirkstoffziel wurde für bestimmte entzündliche Erkrankungen, wie rheumatoide Arthritis aufgeklärt (21), jedoch nicht bei entzündlichen Hauterkrankungen.

Um die pathophysiologische Rolle von MK2 in verschiedenen Hautentzündungsmodellen zu untersuchen, wurden MK2-defiziente- und Wildtyp-Mäuse verwendet. Der MK2-Defekt führte in den Modellen, die Merkmale von chronischen, subakuten und akuten Hautentzündungen aufweisen zu unterschiedlichen Auswirkungen. In den subakuten Modellen für induzierte Kontaktallergien durch Haptene (Dinitrofluorbenzol, DNFB oder Dinitrochlorbenzol, DNCB) sollten MK2-defiziente Mäuse eine T-Zell-abhängige Hautentzündung mit einem ausgeprägten

TH1-Phänotyp entwickeln. Lediglich in dem DNFB-induzierten Kontaktallergiemodell konnte eine entzündungshemmende Wirkung erzielt werden. In beiden Modellen wurde eine Erhöhung der TNF-α- und IL-1β mRNA-Expression beobachtet. Die Neutralisierung von TNF-α und die pharmakologische Blockade von p38 zeigte in beiden Modellen eine signifikante Reduzierung der Entzündung [Publikation 2 (43)].

Wir konnten *in-vitro* zeigen, dass die TLR-induzierte TNF-α-Produktion in MK2-defizienten Milzzellen signifikant reduziert wurde. Diese Daten stimmen mit den Ergebnissen aus dem Modell der LPS-induzierten systemischen Entzündung überein. Im Gegensatz dazu war die CD3/CD28-vermittelte TNF-α-Produktion in MK2-defizienten CD4+ T-Zellen weniger beeinflusst.

Die Tatsache, dass die TLR-abhängige, aber nicht TCR-abhängige TNF-α-Produktion in MK2-defizienten Zellen signifikant verringert war, stimmt mit der etablierten Rolle des p38/MK2-Pfad überein, der sich direkt stromabwärts des TLR4/IRAK4/TAK1/MKK3/MKK6-Signalweg befindet (61). Im Gegensatz dazu könnte die TCR-Stimulation einen alternativen Mechanismus verwenden, bei dem p38 an Tyr323 phosphoryliert wird [Publikation 2 (43)]. Dieser Mechanismus ist abhängig von der Tyrosinkinase Lck und wird durch Zap70 vermittelt (62). Dieser p38/MK2-unabhängige Weg könnte auch erklären, weshalb die pharmakologische Blockade von p38 in MK2-defizienten CD4+ T-Zellen geringere Auswirkungen auf die TNF-α-Produktion als die in MK2-defizienten Milzzellen nach TCR-Stimulation hat.

Eine mögliche Erklärung für den gegensätzlichen Einfluss des MK2-Defekts in T-Zell-abhängigen Kontaktallergiemodellen könnte die Auswirkung durch Chemikalien, wie Haptene auf Immunzellen sein. Verschiedene Studien haben Unterschiede in zellulären und molekularen Mechanismen gezeigt, die von diesen Verbindungen hervorgerufen werden. Im Gegensatz zu DNFB erhöht DNCB die Expression von CD86, HLA-DR und die TNF-α-Sekretion in dendritischen Zellen (63). Es wäre somit möglich, dass die Haptene unterschiedliche Signalwege aktivieren. Demzufolge wäre die therapeutische Blockade von MK2 nur sinnvoll, wenn der Entzündungsprozess vor allem von Makrophagen- oder dendritischen Zellen vermittelt wird. Die Erfolgsaussichten für TH1-oder TH17-vermittelte Entzündungen sind dagegen eingeschränkt.

6.3 Die Longitudinale intravitale Bildgebung des femoralen Knochenmarks veranschaulicht die Plastizität innerhalb des Gefäßsystems– Publikation 3

Das Knochenmark ist der zentrale Ort für die Bildung und Aufrechterhaltung des immunologischen Gedächtnisses und die Hämatopoese. Gedächtnis-T-Zellen vermitteln nach primären Antigenkontakt den Langzeitschutz vor Krankheitserregern (25; 26). In spezifischen Knochenmarksnischen, die von Stromazellen organisiert werden, überleben Gedächtnis-T-Zellen in einem Ruhezustand bis sie erneut mit demselben Antigen konfrontiert werden und

eine effektivere sekundäre Immunantwort eingeleitet wird (27; 28). Die Mechanismen, wie diese Nischen reguliert werden und welche Überlebenssignale die Gedächtnis-T-Zellen benötigen um eine schützende Immunität zu gewährleisten sind jedoch nicht vollständig aufgeklärt.
Das Knochenmarkgewebe wird von einem dichten System aus Blutgefäßen durchzogen. Diese sind für den Transport der in das Knochenmark eintretenden und austretenden Zellen sowie für die Zufuhr von Sauerstoff, Nährstoffen und Wachstumsfaktoren verantwortlich (29).
Die *in-vivo* Multi-Photonen-Mikroskopie ist eine geeignete Methode, um einen Einblick in die Interaktionen im lebenden Gewebe unter physiologischen und pathologischen Bedingungen zu erhalten. Die bereits etablierten Methoden zur Intravitalmikroskopie im Knochenmark von Mäusen sind jedoch zeitlich sehr begrenzt und besitzen geringe Eindringtiefen.
Es wurde von uns eine neue intravitale Multi-Photonen-Mikroskopie Methode entwickelt, wobei dieselben Gewebebereiche im Knochenmark in Längsrichtung im Femur von Mäusen analysiert werden konnten [Publikation 3 (44)]. Mit dieser Technik war es möglich, über mehrere Monate lang erfolgreich ein stabiles Bildgebungsvolumen in demselben Individuum tief in der Markhöhle nachzuweisen. Für die Visualisierung wurde ein Endoskopsystem dauerhaft in der Knochenmarkhöhle am Femur der Maus implantiert. Um eine mögliche Veränderung des Bewegungsverhaltens und der Schmerzsensitivität der Mäuse nach der Operation zu ermitteln, wurde die Aktivität der Tiere mit Hilfe der RFID-Technologie aufgezeichnet. Die Analyse zeigte, nachdem sich die Tiere von der Implantation des Endoskopsystems erholt hatten (am Tag 14), kam es zu keiner Beeinträchtigung der Aktivität. Interessanterweise gab es sowohl zu frühen als auch zu späten Zeitpunkten nach der Operation keine signifikanten Unterschiede der individuellen Aktivitätsprofile zwischen Kontrolltieren, die einer Scheinbehandlung unterzogen wurden und Mäusen, die das Endoskop erhalten haben.
Mit der Bildgebungstechnologie konnten wir eine zelluläre Dynamik und eine strukturelle Plastizität der Blutgefäße im Knochenmark, nicht nur während der Regenerationsphase nach der Implantation, sondern auch bei der Homöostase beobachten. Der direkte Vergleich aufeinanderfolgender Aufzeichnungen machte deutlich, dass sich das Gefäßnetzwerk und die zelluläre Zusammensetzung im Knochenmark kontinuierlich zu verändern scheint. Insbesondere konnten wir beobachten, dass kleinere Gefäße ihre Form ständig - innerhalb von 24 Stunden - dauerhaft umstrukturieren. Dies deutet darauf hin, dass das benötigte Blutgefäßnetz für die Migration und Proliferation von Zellen und die Bereitstellung von Überlebensfaktoren, Nährstoffen und Sauerstoff keine statischen Strukturen, sondern variable und dynamische Merkmale aufweisen [Publikation 3 (44)]. Somit passen sich Blutgefäße an und reagieren dynamisch auf Veränderungen in ihrer lokalen Mikroumgebung und können dadurch verschiedene physiologische, regenerative und pathobiologische Prozesse regulieren.
Zusammengenommen eröffnet diese neue Bildgebungstechnologie die Möglichkeit, sowohl langfristige, als auch kurzfristige Prozesse der Zelldynamik im Knochenmark zu visualisieren

und die Mechanismen, die zur Aufrechterhaltung des immunologischen Gedächtnisses beitragen, zu charakterisieren. Außerdem trägt es zu einem besseren Verständnis der Vaskularisation im Knochenmark und Prozesse wie Knochenregeneration und Hämatopoese bei.

7. Literaturverzeichnis

1. Langrish, C.L., Chen, Y., Blumenschein, W.M., Mattson, J., Basham, B., Sedgwick, J.D., McClanahan, T., Kastelein, R.A., Cua, D.J. IL-23 Drives a Pathogenic T Cell Population That Induces Autoimmune Inflammation . *J Exp Med.* 2005 , 201:233-40.
2. Murphy, C. A., Langrish, C. L., Chen, Y., Blumenschein, W., McClanahan, T., Kastelein, R. A., Sedgwick, J. D. and Cua, D. J. Divergent pro- and antiinflammatory roles for IL-23 and IL-12 in joint autoimmune inflammation. *The Journal of experimental medicine.* 2003, 198: 1951-1957.
3. Zhu, J., Paul, W.E. CD4 T cells: fates, functions, and faults. *Blood.* 2008, 112:1557-69.
4. Annunziato, F., Cosmi, L., Santarlasci, V., Maggi, L., Liotta, F., Mazzinghi, B., Parente, E., Fili, L., Ferri, S., Frosali, F., Giudici, F., Romagnani, P., Parronchi, P., Tonelli, F., Maggi, E. and Romagnani, S. Phenotypic and functional features of human Th17 cells. *The Journal of experimental medicine.* 2007, 204: 1849-1861.
5. Harbour, S.N., Maynard, C.L., Zindl, C.L., Schoeb, T.R., Weaver, C.T. Th17 Cells Give Rise to Th1 Cells That Are Required for the Pathogenesis of Colitis . *Proc Natl Acad Sci U S A.* 2015 , 112:7061-6.
6. Kamali, A.N., Noorbakhsh, S.M., Hamedifar, H., Jadidi-Niaragh, F., Yazdani, R., Bautista, J.M., Azizi, G. A role for Th1-like Th17 cells in the pathogenesis of inflammatory and autoimmune disorders. *Mol Immunol.* 2019, 105:107-115.
7. Kunkl, M., Frascolla, S., Amormino, C., Volpe, E., Tuosto, L. T Helper Cells: The Modulators of Inflammation in Multiple Sclerosis . *Cells.* 2020, 9, 482.
8. Kühn, R., Löhler, J., Rennick, D., Rajewsky, K., Müller, W. Interleukin-10-deficient mice develop chronic enterocolitis. *Cell.* 1993 , S. 75:263-74.
9. Fiorentino, D.F., Zlotnik, A., Mosmann, T.R., Howard, M., O'Garra, A. IL-10 inhibits cytokine production by activated macrophages. *J Immunol.* 1991, 147:3815-22.
10. de Waal Malefyt, R., Abrams, J., Bennett, B., Figdor, C.G., de Vries, J.E.,. Interleukin 10(IL-10) inhibits cytokine synthesis by human monocytes: an autoregulatory role of IL-10 produced by monocytes. *J Exp Med.* 1991, 174:1209-20.
11. D'Andrea, A., Aste-Amezaga, M., Valiante, N.M., Ma, X., Kubin, M., Trinchieri, G.,. Interleukin 10 (IL-10) inhibits human lymphocyte interferon gamma-production by suppressing natural killer cell stimulatory factor/IL-12 synthesis in accessory cells. *J Exp Med.* 1993, 178:1041-8.
12. Fiorentino, D.F., Zlotnik, A., Vieira, P., Mosmann, T.R., Howard, M., Moore, K.W., O'Garra, A. IL-10 acts on the antigen-presenting cell to inhibit cytokine production by Th1 cells. *J Immunol.* 1991, 146:3444-51.
13. de Waal Malefyt, R., Haanen, J., Spits, H., Roncarolo, M.G., te Velde, A., Figdor, C., Johnson, K., Kastelein, R., Yssel, H., de Vries, J.E. Interleukin 10 (IL-10) and viral IL-10 strongly reduce antigen-specific human T cell proliferation by diminishing the antigen-presenting capacity of monocytes via downregulation of class II major histocompatibility complex expression. *J Exp Med.* 1991, 174:915-24.
14. Ding, L., Linsley, P.S., Huang, L.Y., Germain, R.N., Shevach, E.M. IL-10 inhibits macrophage costimulatory activity by selectively inhibiting the up-regulation of B7 expression. *J Immunol.* 1993, 151:1224-34.
15. Asadullah, K., Sterry, W., Volk, H.D. Interleukin-10 therapy--review of a new approach. *Pharmacol Rev.* 2003, 55:241-69.
16. Barbara, G., Xing, Z., Hogaboam, C.M., Gauldie, J., Collins, S.M. Interleukin 10 gene transfer prevents experimental colitis in rats. *Gut.* 2000, 46:344-9.

17. Herfarth, H.H., Böcker, U., Janardhanam, R., Sartor, R.B. Subtherapeutic corticosteroids potentiate the ability of interleukin 10 to prevent chronic inflammation in rats. *Gastroenterology.* 1998, 115:856-65, S. 115:856-65.
18. Kontoyiannis, D., Kotlyarov, A., Carballo, E., Alexopoulou, L., Blackshear, P.J., Gaestel, M., Davis, R., Flavell, R., Kollias, G. Interleukin-10 targets p38 MAPK to modulate ARE-dependent TNF mRNA translation and limit intestinal pathology. *EMBO J.* 2001 , 20:3760-70.
19. Kotlyarov, A., Neininger, A., Schubert, C., Eckert, R., Birchmeier, C., Volk, H.D., Gaestel, M. MAPKAP kinase 2 is essential for LPS-induced TNF-alpha biosynthesis. *Nat Cell Biol.* 1999, 1:94-7.
20. Ronkina, N., Kotlyarov, A., Dittrich-Breiholz, O., Kracht, M., Hitti, E., Milarski, K., Askew, R., Marusic, S., Lin, L.L., Gaestel, M., Telliez, J.B. The mitogen-activated protein kinase (MAPK)-activated protein kinases MK2 and MK3 cooperate in stimulation of tumor necrosis factor biosynthesis and stabilization of p38 MAPK. *Mol Cell Biol.* 2007, 27:170-81.
21. Hegen, M., Gaestel, M., Nickerson-Nutter, C.L., Lin, L.L., Telliez, J.-B. MAPKAP Kinase 2-deficient Mice Are Resistant to Collagen-Induced Arthritis . *J Immunol.* 2006, 177, 1913-7.
22. Dambach, D.M. Potential Adverse Effects Associated With Inhibition of p38alpha/beta MAP Kinases. *Curr Top Med Chem.* 2005, 929-39.
23. Singh, R.K., Diwan, M., Dastidar, S.G., Najmi, A.K. Differential effect of p38 and MK2 kinase inhibitors on the inflammatory and toxicity biomarkers in vitro. *Hum Exp Toxicol.* 2018, 37:521-531. .
24. Gaestel, M. MAPKAP kinases — MKs — two's company, three's a crowd. *Nature Reviews Molecular Cell Biology .* 2006, 120–130.
25. Chang, H.D., Tokoyoda, K., Radbruch, A. Immunological memories of the bone marrow. *Immunol Rev.* 2018, 283:86-98.
26. Di Rosa, F., Gebhardt, T. Bone Marrow T Cells and the Integrated Functions of Recirculating and Tissue-Resident Memory T Cells. *Front Immunol.* 2016, 7: 51.
27. Tokoyoda, K., Zehentmeier, S., Hegazy, A.N., Albrecht, I., Grün, J.R., Löhning, M., Radbruch, A. Professional memory CD4+ T lymphocytes preferentially reside and rest in the bone marrow. *Immunity.* 2009 , 30:721-30.
28. Tokoyoda, K., Zehentmeier, S., Chang, H.D., Radbruch, A. Organization and maintenance of immunological memory by stroma niches. *Eur J Immunol.* 2009 , 39:2095-9.
29. Ramasamy, S.K., Kusumbe, A.P., Itkin, T., Gur-Cohen, S., Lapidot, T., Adams, R.H. Regulation of Hematopoiesis and Osteogenesis by Blood Vessel-Derived Signals. *Annu Rev Cell Dev Biol.* 2016, 32:649-675.
30. Naundorf, S., Schröder, M., Höflich, C., Suman, N., Volk, H.D., Grütz, G. IL-10 interferes directly with TCR-induced IFN-gamma but not IL-17 production in memory T cells. *Eur J Immunol.* 2009, 39:1066-77.
31. de Waal Malefyt, R., Yssel, H., de Vries, J.E. Direct effects of IL-10 on subsets of human CD4+ T cell clones and resting T cells. Specific inhibition of IL-2 production and proliferation. *J Immunol.* 1993, 150:4754-65.
32. Hodge, D.L., Martinez, A., Julias, J.G., Taylor, L.S., Young, H.A. Regulation of nuclear gamma interferon gene expression by interleukin 12 (IL-12) and IL-2 represents a novel form of posttranscriptional control. *Mol Cell Biol.* 2002, 1742-53.
33. Meuer, S.C., Hussey, R.E., Cantrell, D.A., Hodgdon, J.C., Schlossman, S.F., Smith, K.A., Reinherz, E.L. Triggering of the T3-Ti antigen-receptor complex results in clonal T-cell proliferation through an interleukin 2-dependent autocrine pathway. *Proc Natl Acad Sci USA.* 1984 , 81:1509–1513. .

34. Schröder, M., Meisel, C., Buhl, K., Profanter, N., Sievert, N., Volk, H.D., Grütz, G. Different modes of IL-10 and TGF-beta to inhibit cytokine-dependent IFN-gamma production: consequences for reversal of lipopolysaccharide desensitization. *J Immunol.* 2003, 170:5260-7.
35. Amyes, E., McMichael, A. J. and Callan, M. F. Human CD41T cells are predominantly distributed among six phenotypically and functionally distinct subsets. *J. Immunol.* 2005, 175: 5765–5773.
36. Joss, A., Akdis, M., Faith, A., Blaser, K., Akdis, C.A. IL-10 directly acts on T cells by specifically altering the CD28 co-stimulation pathway. *Eur J Immunol.* 2000, 30:1683-90.
37. Taylor, A., Akdis, M., Joss, A., Akkoç, T., Wenig, R., Colonna, M., Daigle, I., Flory, E., Blaser, K., Akdis, CA. IL-10 inhibits CD28 and ICOS costimulations of T cells via src homology 2 domain-containing protein tyrosine phosphatase 1. *J Allergy Clin Immunol.* 2007, 120:76-83.
38. Pathak, M.K., Yi, T. Sodium stibogluconate is a potent inhibitor of protein tyrosine phosphatases and augments cytokine responses in hemopoietic cell lines. *J Immunol.* 2001, 15;167(6):3391-7.
39. Liu. Y., Wei, S.H., Ho, A.S., de Waal Malefyt, R., Moore, K.W. Expression cloning and characterization of a human IL-10 receptor. *J Immunol.* 1994, 152:1821-9.
40. Kotenko, S.V., Krause, C.D., Izotova, L.S., Pollack, B.P., Wu, W., Pestka, S. Identification and functional characterization of a second chain of the interleukin-10 receptor complex. *EMBO J.* 1997, 16:5894-903.
41. Berlato, C., Cassatella, M.A., Kinjyo, I., Gatto, L., Yoshimura, A., Bazzoni, F. Involvement of suppressor of cytokine signaling-3 as a mediator of the inhibitory effects of IL-10 on lipopolysaccharide-induced macrophage activation. *J Immunol.* 2002 , 168:6404-11.
42. Shen, H., Goodall, J.C., Hill Gaston, J.S. Frequency and phenotype of peripheral blood Th17 cells in ankylosing spondylitis and rheumatoid arthritis. *Arthritis Rheum.* 2009, 60(6):1647-56.
43. Schottelius, A.J., Zügel, U., Döcke, W.D., Zollner, T.M., Röse, L., Mengel, A., Buchmann, B., Becker, A., Grütz, G., Naundorf, S., Friedrich, A., Gaestel, M., Asadullah, K. The role of mitogen-activated protein kinase-activated protein kinase 2 in the p38/TNF-alpha pathway of systemic and cutaneous inflammation. *J Invest Dermatol.* 2010, 130:481-91.
44. Reismann, D., Stefanowski, J., Günther, R., Rakhymzhan, A., Matthys, R., Nützi, R., Zehentmeier, S., Schmidt-Bleek, K., Petkau, G., Chang, H.D., Naundorf, S., Winter, Y., Melchers, F., Duda, G., Hauser, A.E., Niesner, R.A. Longitudinal intravital imaging of the femoral bone marrow reveals plasticity within marrow vasculature. *Nat Commun.* 2017, 8:2153.
45. Asadullah, K., Sterry, W., Stephanek, K., Jasulaitis, D., Leupold, M., Audring, H., Volk, H. D., Docke, W. D. IL-10 is a key cytokine in psoriasis. Proof of principle by IL-10 therapy: a new therapeutic approach. *J. Clin. Invest.* 1998, 101: 783–794.
46. Cua, D.J., Sherlock. J., Chen, Y., Murphy, C.A., Joyce, B., Seymour, B., Lucian, L., To, W., Kwan, S., Churakova, T., Zurawski, S., Wiekowski, M., Lira, S.A., Gorman, D., Kastelein, R.A., Sedgwick, J.D. Interleukin-23 rather than interleukin-12 is the critical cytokine for autoimmune inflammation of the brain. *Nature.* 2003, 421:744-8.
47. Toussirot, E.. The IL23/Th17 pathway as a therapeutic target in chronic inflammatory diseases. *Inflamm Allergy Drug Targets.* 2012, 11:159-68.
48. Kuwabara, T.,Ishikawa, F.,Kondo, M.,Kakiuchi, T. The Role of IL-17 and Related Cytokines in Inflammatory Autoimmune Diseases. *Mediators Inflamm.* 2017, 2017:3908061.
49. Lohning, M., Richter, A., Radbruch, A. Cytokine memory of T helper lymphocytes. *Adv. Immunol.* 2002, 80:115–181.
50. Wilson, C. B., Makar, K. W., Shnyreva, M., Fitzpatrick, D. R.,. DNA methylation and the expanding epigenetics of T cell lineage commitment. *Semin. Immunol.* 2005, 17:105–119.
51. Huber, S., Gagliani, N., Esplugues, E., O'Connor, W. Jr., Huber, F.J., Chaudhry, A., Kamanaka, M., Kobayashi, Y., Booth, C.J., Rudensky, A.Y., Roncarolo, M.G., Battaglia, M., Flavel,l R.A.

Th17 Cells Express Interleukin-10 Receptorand Are Controlled by Foxp3(-) and Foxp3(+) Regulatory CD4(+) T Cells in an Interleukin-10-Dependent Manner. *Immunity .* 2011, 34: 554-65.

52. Oppmann, B., Lesley, R., Blom, B., Timans, J. C., Xu, Y., Hunte, B ., Vega, F., Yu, N., Wang, J., Singh, K ., Zonin, F., Vaisberg, E., Churakova, T., Liu, M., Gorman, D., Wagner, J., Zurawski, S., Liu, Y., Abrams, J. S., Moore, K. W., Rennick, D., de Waal. Novel p19 Protein Engages IL-12p40 to Form a Cytokine, IL-23, With Biological Activities Similar as Well as Distinct From IL-12 . *Immunity.* 2000, 13,715-25.
53. Mukasa, R., Balasubramani, A., Lee, Y. K., Whitley, S. K., Weaver, B. T., Shibata, Y., Crawford, G. E., Hatton, R. D. and Weaver, C. T.,. Epigenetic instability of cytokine and transcription factor gene loci underlies plasticity of the T helper 17 cell lineage. *Immunity.* 2010, 32: 616-627.
54. Braat, H., Rottiers, P., Hommes, D.W., Huyghebaert, N., Remaut, E., Remon, J.P., van Deventer, S.J., Neirynck, S., Peppelenbosch, M.P., Steidler, L. A phase I trial with transgenic bacteria expressing interleukin-10 in Crohn's disease. *Clin. Gastroenterol. Hepatol.* 2006, 4:754–759.
55. Rousset, F., Garcia, E., Defrance, T., Péronne, C., Vezzio, N., Hsu, D.H., Kastelein, R., Moore, K.W., Banchereau, J. Interleukin 10 is a potent growth and differentiation factor for activated human B lymphocytes. *Proc Natl Acad Sci U S A.* 1992 , 89(5):1890-3.
56. Itoh, K.,Hirohata, S. The role of IL-10 in human B cell activation, proliferation, and differentiation. *J Immunol .* 1995, 154: 4341-4350.
57. Carson, W.E., Lindemann, M.J., Baiocchi, R., Linett, M., Tan, J.C., Chou, C.C., Narula, S., Caligiuri, M.A. The functional characterization of interleukin-10 receptor expression on human natural killer cells. *Blood.* 1995, 85:3577-85.
58. Emmerich, J., Mumm, J.B., Chan, I.H., LaFace, D., Truong, H., McClanahan, T., Gorman, D.M., Oft, M. IL-10 directly activates and expands tumor-resident CD8(+) T cells without de novo infiltration from secondary lymphoid organs. *Cancer Res.* 2012 , 72:3570-81.
59. Lee, J.C., Laydon, J.T., McDonnell, P.C., Gallagher, T.F., Kumar, S., Green, D., McNulty, D., Blumenthal, M.J., Heys, J.R., Landvatter, S.W., Strickler, J.E., McLaughlin, M.M., Siemens, I.R., Fisher, S.M., Livi, G.P., White, J.R., Adams, J.L., Young, P.R. A Protein Kinase Involved in the Regulation of Inflammatory Cytokine Biosynthesis . *Nature.* 1994, 372, 739-46 .
60. Neininger, A., Kontoyiannis, D., Kotlyarov, D., Winzen, R., Eckert, R., Volk, H.-D., Holtmann, H., Kollias, G., Gaestel, M. MK2 Targets AU-rich Elements and Regulates Biosynthesis of Tumor Necrosis Factor and interleukin-6 Independently at Different Post-Transcriptional Levels. *J Biol Chem.* 2002, 277, 3065-8 .
61. Gaestel, M., Kotlyarov, A., Kracht, M. Targeting innate immunity protein kinase signalling in inflammation. *Nat Rev Drug Discov.* 2009 , 8:480-99.
62. Salvador, J.M., Mittelstadt, P.R., Guszczynski, T., Copeland, T.D., Yamaguchi, H., Appella, E., Fornace, A.J. Jr., Ashwell, J.D. Alternative p38 activation pathway mediated by T cell receptor-proximal tyrosine kinases. *Nat Immunol.* 2005, 6:390-5.
63. Manome, H., Aiba, S., Tagami, H. Simple chemicals can induce maturation and apoptosis of dendritic cells. *Immunology.* 1999 , 98:481-90.
64. Mackay, C. R. T-cell memory: the connection between function, phenotype and migration pathways. *Immunol Today.* 1991, 12(6):189-192.
65. Geginat, J., Paroni, M., Maglie, S., Alfen, J.S., Kastirr, I., Gruarin, P., De Simone, M., Pagani, M., Abrignani, S. Plasticity of human CD4 T cell subsets. *Front Immunol.* 2014, 16;5:630.
66. Lexberg, M., Taubner, A., Albrecht, I., Lepenies, I., Richter, A., Kamradt, T., Radbruch, A., Chang, H.-D. IFN-γ and IL-12 synergize to convert in vivo generated Th17 into Th1/Th17 cells . *Eur. J. Immunol.* 2010, 40: 3017–3027.

67. Rajasingh, J., Bord, E., Luedemann, C., Asai, J., Hamada, H., Thorne, T., Qin, G., Goukassian, D., Zhu, Y., Losordo, D.W., Kishore, R. IL-10-induced TNF-alpha mRNA destabilization is mediated via IL-10 suppression of p38 MAP kinase activation and inhibition of HuR expression. *FASEB J.* 2006 , S. 20:2112-4.
68. Farber, D.L., Netea, M.G., Radbruch, A., Rajewsky, K., Zinkernagel, R.M. Immunological memory: lessons from the past and a look to the future. *Nat Rev Immunol.* 2016, 16:124-8.

8. Eidesstattliche Versicherung

„Ich, Sandra Naundorf, versichere an Eides statt durch meine eigenhändige Unterschrift, dass ich die vorgelegte Dissertation mit dem Thema: Mechanismus der Hemmung der entzündungsfördernden IFN-γ Produktion in Gedächtnis-T-Zellen – Mechanism of inhibition of inflammatory IFN-γ production in memory T cells – selbstständig und ohne nicht offengelegte Hilfe Dritter verfasst und keine anderen als die angegebenen Quellen und Hilfsmittel genutzt habe.
Alle Stellen, die wörtlich oder dem Sinne nach auf Publikationen oder Vorträgen anderer Autoren/innen beruhen, sind als solche in korrekter Zitierung kenntlich gemacht. Die Abschnitte zu Methodik (insbesondere praktische Arbeiten, Laborbestimmungen, statistische Aufarbeitung) und Resultaten (insbesondere Abbildungen, Graphiken und Tabellen) werden von mir verantwortet.

Meine Anteile an etwaigen Publikationen zu dieser Dissertation entsprechen denen, die in der untenstehenden gemeinsamen Erklärung mit dem Erstbetreuer, angegeben sind. Für sämtliche im Rahmen der Dissertation entstandenen Publikationen wurden die Richtlinien des ICMJE (International Committee of Medical Journal Editors; www.icmje.og) zur Autorenschaft eingehalten. Ich erkläre ferner, dass ich mich zur Einhaltung der Satzung der Charité – Universitätsmedizin Berlin zur Sicherung Guter Wissenschaftlicher Praxis verpflichte.

Weiterhin versichere ich, dass ich diese Dissertation weder in gleicher noch in ähnlicher Form bereits an einer anderen Fakultät eingereicht habe.

Die Bedeutung dieser eidesstattlichen Versicherung und die strafrechtlichen Folgen einer unwahren eidesstattlichen Versicherung (§§156, 161 des Strafgesetzbuches) sind mir bekannt und bewusst.“

Datum Unterschrift

9. Anteilserklärung

Sandra Naundorf hatte folgenden Anteil an den vorgelegten Publikationen:

Publikation 1

Naundorf S*, Schröder M*, Höflich C, Suman N, Volk HD, Grütz G. IL-10 interferes directly with TCR-induced IFN-gamma but not IL-17 production in memory T cells. Eur J Immunol. 2009

* geteilte Erstautorenschaft

Beitrag im Einzelnen: Die Daten dieser Publikation bilden den Großteil der von Frau Sandra Naundorf erzielten Ergebnisse in der Promotion ab. Frau Naundorf war für die Planung und Durchführung der meisten Experimente (immunologische und zellbiologische Assays) verantwortlich und führte die Auswertung und statistische Analyse der Daten selbständig aus.

Der ursprüngliche Ansatz, dass IL-10 einen Effekt auf die TCR-induzierte Zytokinproduktion hat, geht auf eine Beobachtung von Frau Martina Schröder zurück.

Frau Naundorf und Frau Schröder waren an der Erstellung des Manuskripts und der Überarbeitung der revidierten Fassung beteiligt. Daher ist Frau Naundorf als Erstautor (geteilte Erstautorenschaft mit Martina Schröder) in dieser Publikation gelistet.

Publikation 2

Schottelius AJ, Zügel U, Döcke WD, Zollner TM, Röse L, Mengel A, Buchmann B, Becker A, Grütz G, **Naundorf S**, Friedrich A, Gaestel M, Asadullah K. The role of mitogen-activated protein kinase-activated protein kinase 2 in the p38/TNF-alpha pathway of systemic and cutaneous inflammation. J Invest Dermatol. 2010

Anteil: 10%

Beitrag im Einzelnen:

Frau Naundorf trug wichtige Experimente zur Publikation bei (Bestimmung der TNF-α-Produktion von *ex vivo* isolierten Immunzellen von Wildtyp- und MK2-Ko-Mäusen; Figure 7) und beteiligte sich an der Erstellung des Manuskripts.

Publikation 3

Reismann D, Stefanowski J, Günther R, Rakhymzhan A, Matthys R, Nützi R, Zehentmeier S, Schmidt-Bleek K, Petkau G, Chang HD, **Naundorf S**, Winter Y, Melchers F, Duda G, Hauser AE, Niesner RA. Longitudinal intravital imaging of the femoral bone marrow reveals plasticity within marrow vasculature. Nat Commun. 2017

Anteil:10%

Beitrag im Einzelnen:

Frau Naundorf trug ein wichtiges Experiment zur Publikation bei (Bestimmung der Aktivität der Mäuse nach Implantation des Mikroendoskops mittels RFID-Technologie; Figure 2i) und

beteiligte sich an der Erstellung des Manuskripts.

_____

Unterschrift, Datum und Stempel des erstbetreuenden Hochschullehrers

_____

Unterschrift der Doktorandin

10. Ausgewählte Publikationen

Die Seiten 29 bis 66 umfassen folgende Originalartikel:

1. Publikation

Naundorf S*, Schröder M*, Höflich C, Suman N, Volk HD, Grütz G. IL-10 interferes directly with TCR-induced IFN-gamma but not IL-17 production in memory T cells. Eur J Immunol. 2009;39:1066-77.

Impact Factor: 5.179

2. Publikation

Schottelius AJ, Zügel U, Döcke WD, Zollner TM, Röse L, Mengel A, Buchmann B, Becker A, Grütz G, **Naundorf S**, Friedrich A, Gaestel M, Asadullah K. The role of mitogen-activated protein kinase-activated protein kinase 2 in the p38/TNF-alpha pathway of systemic and cutaneous inflammation. J Invest Dermatol. 2010;130:481-91.

Impact Factor: 6.270

3. Publikation

Reismann D, Stefanowski J, Günther R, Rakhymzhan A, Matthys R, Nützi R, Zehentmeier S, Schmidt-Bleek K, Petkau G, Chang HD, **Naundorf S**, Winter Y, Melchers F, Duda G, Hauser AE, Niesner RA. Longitudinal intravital imaging of the femoral bone marrow reveals plasticity within marrow vasculature. Nat Commun. 2017;8:2153.

Impact Factor: 12.353

European Journal of Immunology

IL-10 interferes directly with TCR-induced IFN-γ but not IL-17 production in memory T cells

Sandra Naundorf, Martina Schröder*, Conny Höflich, Nimisha Suman, Hans-Dieter Volk and Gerald Grütz*

Institute of Medical Immunology, Charité, Humboldt-University, Berlin, Germany

IL-10 is a potent immunoregulatory and anti-inflammatory cytokine. However, therapeutic trials in chronic inflammation have been largely disappointing. It is well established that IL-10 can inhibit Th1 and Th2 cytokine production *via* indirect effects on APC. Less data are available about the influence of IL-10 on IL-17 production, a cytokine which has been recently linked to chronic inflammation. Furthermore, there are only few reports about a direct effect of IL-10 on T cells. We demonstrate here that IL-10 can directly interfere with TCR-induced IFN-γ production in freshly isolated memory T cells in the absence of APC. This effect was independent of the previously described effects of IL-10 on T cells, namely inhibition of IL-2 production and inhibition of CD28 signaling. In contrast, IL-10 did not affect anti-CD3/anti-CD28-induced IL-17 production from memory T cells even in the presence of APC. This might have implications for the interpretation of therapeutic trials in patients with chronic inflammation where Th17 cells contribute to pathogenesis.

Key words: Cytokine · IFN-γ · IL-10 · IL-17 · T cells

Introduction

IL-10 was first described as a factor produced by Th2 cells, which inhibits cytokine production by Th1 cells [1]. Since then it has emerged that IL-10 is also produced by APC and that it can also inhibit cytokine production by Th0 and Th2 cells. Nevertheless, it is still unclear how exactly this inhibition is mediated on a molecular level and whether all T-cell subpopulations are equally affected by IL-10.

It has been demonstrated that a great amount of the inhibitory activity of IL-10 on T cells is indirect and results from its effects on APC. IL-10 down-regulates surface expression of MHC class II and of several co-stimulatory molecules on APC, such as CD80/86 and ICAM-1, and thereby strongly impairs their antigen-presenting capacity [2–4]. In addition, it influences the production of several soluble mediators including IL-1, IL-6, IL-12, IL-18 and TNF-α [5–7], which support T-cell activation and differentiation into Th1 cells. In line with this, we have previously demonstrated that the inhibitory effect of IL-10 on cytokine-induced IFN-γ production by T cells is entirely dependent on the presence of $CD14^+$ cells and that it can be overcome by the addition of exogenous cytokines [8]. However, T cells express IL-10 receptors and a few direct inhibitory effects of IL-10 on naïve T cells have been described, such as the inhibition of IL-2 production and more recently, the inhibition of CD28 signaling [9–11]. A transient activation of SHP-1 by IL-10 was suggested to mediate the inhibition of CD28 and also ICOS signaling [12].

Despite its broad anti-inflammatory profile, therapeutic trials with IL-10 to dampen an ongoing chronic inflammation have been largely disappointing (reviewed in [13]). The reasons for this are rather unclear. Chronic inflammation is thought to be driven by uncontrolled effector memory T-cell activation. It has been suggested that IL-10 has no direct effects on antigen-primed T cells because they would loose IL-10RI expression after

Correspondence: Dr. Gerald Grütz
e-mail: gerald.gruetz@charite.de

*These authors contributed equally to this work.

© 2009 WILEY-VCH Verlag GmbH & Co. KGaA, Weinheim

activation [14]. In the past, many chronic inflammatory diseases were linked with an excessive Th1 response, with IFN-γ as the detrimental effector cytokine. However, later reports demonstrated that IFN-γ is necessary for the activity of regulatory T cells [15] and that it has also a role in limiting inflammation [16]. It now emerges that excessive production of IL-17 from Th17 cells might be an even more decisive factor in chronic inflammation (reviewed in [17, 18]). Whereas several factors which negatively regulate Th17 cell development have been described [19, 20], it is unknown which factors can restrict an already established memory IL-17 production.

Therefore, we analyzed the effect of IL-10 on various T-cell subpopulations regarding their TCR-induced IFN-γ and IL-17 production. In contrast to earlier reports [11, 12, 21], we found that IL-10 can inhibit TCR-induced IFN-γ production in freshly isolated memory T cells in the absence of APC. However, we could not detect any direct inhibitory effect on Th17 cells regarding their anti-CD3-induced IL-17 production. Furthermore, in the presence of APC, IL-10 had a lower capacity to inhibit antigen-induced IL-17 production compared with IFN-γ production in T cells. These results may help to understand why the success of IL-10 therapy in an ongoing chronic inflammation has its limitations. IL-10 inhibits IFN-γ stronger then IL-17 after antigen presentation *via* APC.

Results

IL-10 inhibits IFN-γ and to a lesser extent, IL-17 after antigen presentation *via* APC

IL-10 is known to inhibit the production of a wide range of T-cell cytokines by reducing antigen presentation and co-stimulation mediated by APC. To test whether this also applies for IL-17 production, we compared the ability of IL-10 to inhibit antigen-dependent production of IFN-γ and IL-17, respectively. We choose a fungal stimulus as antigen because they are known inducers of IL-17. Therefore, we stimulated PBMC with *Candida albicans* antigen in the absence or presence of IL-10 for 72 h (Fig. 1A). Under these conditions, IL-10 can exert its inhibitory effect on APC and T cells. Antigen-induced IFN-γ and IL-17 production in the absence of IL-10 were comparable between IFN-γ and IL-17 with a median of around 350 pg/mL. As expected, IL-10 was able to inhibit both IFN-γ and IL-17 production (each with $p<0.05$, Fig. 1A). However, the inhibitory effect on IFN-γ production was significantly stronger than on IL-17 production ($p<0.05$, Fig. 1A). This indicates that IL-10 might use different mechanisms for inhibiting IFN-γ and IL-17 production, respectively.

IL-10 interferes with TCR-induced IFN-γ but not IL-17 in freshly-isolated PBMC

We next asked whether IL-10 would be able to inhibit IFN-γ and/or IL-17 production independently of its ability to down-regulate antigen presentation and co-stimulatory molecules on APC. Hence, we provided TCR- and co-stimulation through plate-bound antibodies against CD3 and CD28. PBMC were stimulated for 24 h in the presence or absence of IL-10 before IFN-γ and IL-17 production were measured in the supernatants by ELISA. IL-10 significantly inhibited TCR-induced IFN-γ production ($p<0.05$, Fig. 1B), but only had a weak and non-significant inhibitory effect on IL-17 production (Fig. 1B). Similar effects were seen on the mRNA level: IL-10 inhibited TCR-induced IFN-γ mRNA production by 80% ($p<0.05$, Fig. 1C), but did not affect IL-17 mRNA induction (Fig. 1C).

These data were confirmed by assessing intracellular cytokine production in anti-CD3/anti-CD28-stimulated PBMC. For this, we added Brefeldin A only during the last 6 h of TCR-stimulation in order to avoid any interference of Brefeldin A with the inhibitory activity of IL-10. IL-10 reduced the percentage of IFN-γ-producing $CD4^+$ as well as $CD8^+$ T cells, but did not affect IL-17-producing T cells (Fig. 1D). IL-10 did not affect the activation of T cells in general, as we saw no difference in the percentage of CD25-expressing T cells in the presence or absence of IL-10 (data not shown). Other T-cell activation markers such as HLA-DR, another marker for acute activation and CD57, a marker for chronic activation, were also largely unaffected by IL-10 (data not shown).

Inhibitory effect of IL-10 on TCR-induced IFN-γ is independent of IL-2

IL-2 is an important cofactor for IFN-γ production by enabling mRNA transport and translation [22, 23]. Furthermore, it has been reported that exogenous addition of IL-2 abrogates the inhibitory effects of IL-10 on T-cell proliferation [10]. Indeed, we could confirm that the presence of exogenous IL-2 abrogated the anti-proliferative effect of IL-10 on T cells (Fig. 2A). In contrast, it did-not influence the inhibitory effect of IL-10 on IFN-γ production (Fig. 2B). Furthermore, exogenous addition of IL-2 did neither influence IL-17 production in presence nor absence of IL-10 (data not shown). These results pointed toward a so far unknown direct effect of IL-10 on IFN-γ production independent of IL-2 repression. Furthermore, because the amount of IFN-γ induction was higher in the presence of IL-2, we decided to add IL-2 throughout the following experiments.

IL-10 directly inhibits TCR-induced IFN-γ production in the absence of APC

The IL-10-induced inhibition on IFN-γ production after direct T-cell-stimulation with plate-bound anti-CD3/anti-CD28 mAb in the presence and absence of exogenous IL-2 suggested an (i) APC- and (ii) IL-2-independent mode of inhibition. However, in our previous work, we demonstrated the necessity of $CD14^+$ monocytes for the inhibitory effect of IL-10 on cytokine-induced IFN-γ production by T cells [8]. We therefore wondered whether

© 2009 WILEY-VCH Verlag GmbH & Co. KGaA, Weinheim

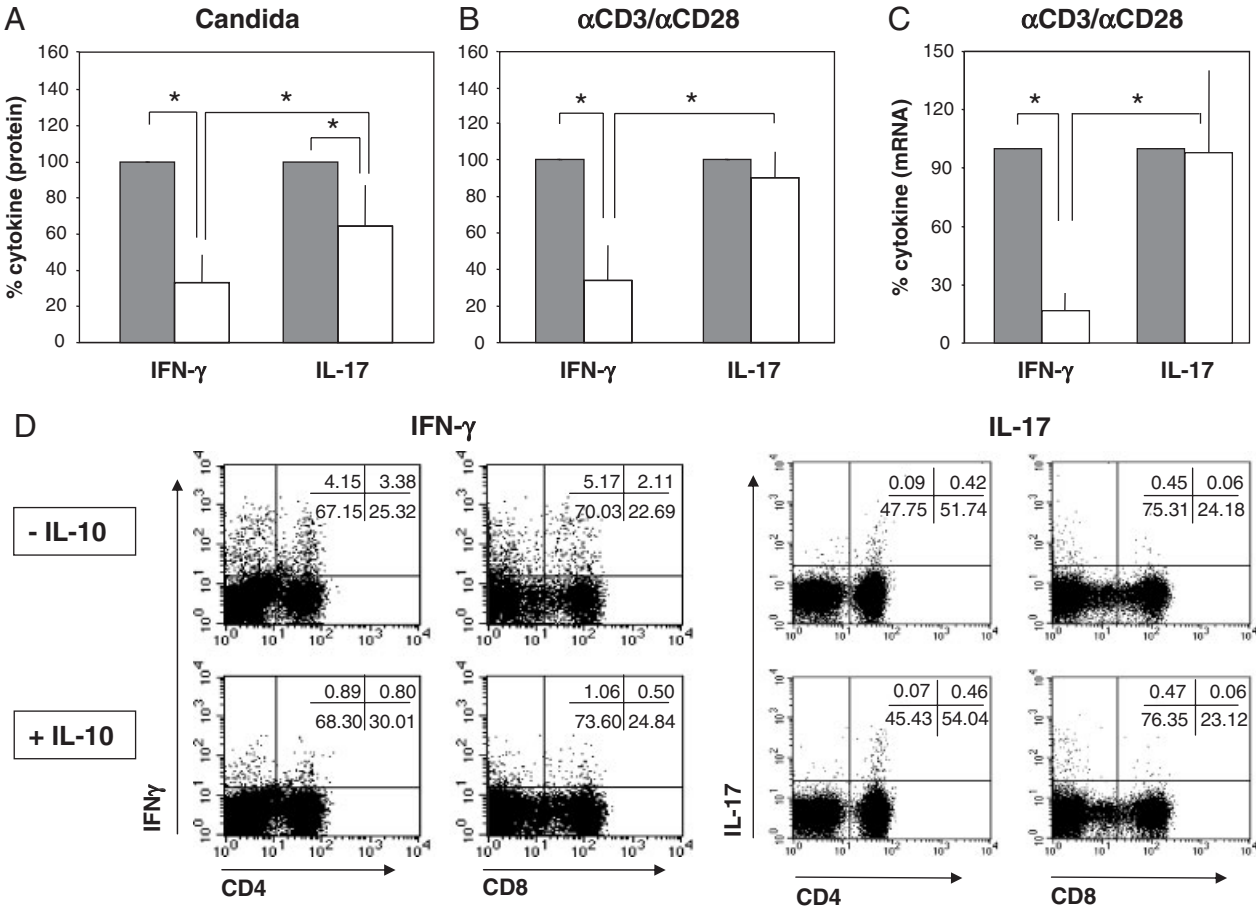

Figure 1. IL-10 does inhibit TCR-induced IFN-γ but not IL-17 production in freshly isolated PBMC. (A) Human PBMC from healthy blood donors were activated with *C. albicans* antigen for 72 h in the presence (white bars) or absence (gray bars) of IL-10 (10 ng/mL). Supernatants were collected for IFN-γ and IL-17 analyses by ELISA. The amount of IFN-γ or IL-17 in the absence of IL-10 was set to 100% for each individual donor, and IL-10 inhibition related to it. The absolute values ranged from 173 to 4453 pg/mL for IFN-γ and from 235 to 513 pg/mL for IL-17 in the non-inhibited samples. Results shown are averages from five independent experiments (±SD). (B) Human PBMC from healthy blood donors were activated with immobilised anti-CD3/anti-CD28 mAb (1 μg/mL each) and IL-2 (100 U/mL) for 24 h in the presence (white bars) or absence (gray bars) of IL-10 (10 ng/mL). Supernatants were collected thereafter and IFN-γ and IL-17 levels analyzed by ELISA. The amount of IFN-γ or IL-17 after anti-CD3/anti-CD28 treatment in the absence of IL-10 was set to 100% for each individual donor, and IL-10 inhibition related to it. The absolute values ranged from 9.4 to 427 ng/mL for IFN-γ and from 0.9 to 1.5 ng/mL for IL-17 in the non-inhibited samples. Results shown are averages from five independent experiments (±SD). (C) Following the same stimulation setup as described for (B), RNA was extracted from cells and IFN-γ and IL-17 mRNA levels were determined by Real-Time RT-PCR and normalized to the expression of the house keeping gene HPRT. The amount of IFN-γ or IL-17 mRNA following anti-CD3/anti-CD28 treatment without IL-10 incubation (gray bars) was set to 100% for each individual sample and IL-10 inhibition (white bars) related to this. Results shown are averages from five independent experiments (±SD). Significant differences as calculated by Wilcoxon test ($p<0.05$) are indicated by an asterisk (*). (D) PBMC were TCR-stimulated for 24 h by anti-CD3/anti-CD28 mAb (1 μg/mL each) and Brefeldin A added for the last 6 h. Cells were then stained with a mixture of CD3/CD4 and CD3/CD8 mAb, respectively, and intracellular IFN-γ and IL-17 production in $CD4^+$ and $CD8^+$ T cells was analyzed by flow cytometry. Data from one representative out of three experiments are shown.

this is also the case for TCR-induced IFN-γ production. Hence, we depleted $CD14^+$ monocytes from freshly isolated PBMC and then stimulated the remaining cells with anti-CD3/anti-CD28 mAb and IL-2 in the presence or absence of IL-10 for 24 h. IL-10 strongly inhibited TCR-induced IFN-γ production also in the absence of $CD14^+$ APC ($p<0.05$, Fig. 3A). To exclude an effect of $CD14^-$ APC such as B cells, we further purified the CD14-depleted PBMC by an additional step of $CD4^+$ selection. This procedure yielded highly purified $CD4^+$ T cells (on average 99%). IL-10 still significantly inhibited TCR-induced IFN-γ production, even though the effect was now less pronounced than with depletion of $CD14^+$ APC alone ($p<0.05$, Fig. 3A). Similar results were obtained after MACS™ purification of $CD4^+$ T cells either by direct $CD4^+$ selection or by CD4-untouched separation (data not shown). The observed inhibitory effect of IL-10 was not due to an inhibition of cell proliferation during the 24 h of stimulation, as was confirmed by ^{3}H-dTTP-incorporation (data not shown).

In conclusion, IL-10 had a direct inhibitory effect on TCR-induced IFN-γ production by $CD4^+$ T cells in the absence of APC and the presence of IL-2.

© 2009 WILEY-VCH Verlag GmbH & Co. KGaA, Weinheim

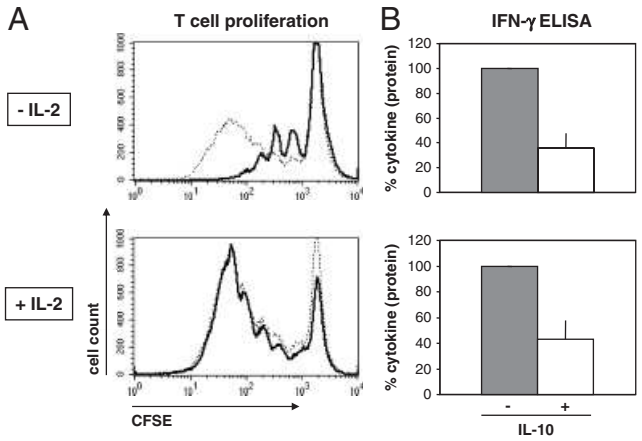

Figure 2. Exogenous IL-2 abrogates IL-10 inhibition of T-cell proliferation but has no influence on IL-10-induced inhibition of IFN-γ production. (A) Human PBMC were labeled with CSFE and proliferation was induced by TCR-stimulation with plate-bound anti-CD3/anti-CD28 mAb (1 μg/mL each) in the presence (bold lines) or absence (dotted lines) of IL-10 (10 ng/mL) and IL-2 (100 U/mL) as indicated. The degree of proliferation was assessed by analyzing the reduction of CSFE-label after cell devision by flow cytometry. One representative out of three experiments is shown. (B) Human PBMC were activated with immobilised anti-CD3/anti-CD28 mAb (1 μg/mL each) in the presence (white bars) or absence (gray bars) of IL-10 (10 ng/mL) and IL-2 (100 U/mL) as indicated. Supernatants were collected thereafter and IFN-γ production analyzed by ELISA. The amount of IFN-γ after anti-CD3/anti-CD28 treatment in the absence of IL-10 was set to 100% for each individual donor, and IL-10 inhibition related to it. The absolute values ranged from 2.7 to 87.6 ng/mL for IFN-γ in the non-inhibited samples. Results shown are averages from three independent experiments (±SD).

IL-10 inhibition of TCR-induced IFN-γ is not overcome by blocking SHP-1

In contrast to naïve T cells, antigen-primed T cells do not need co-stimulation for re-activation. Previous work suggested that IL-10 does not inhibit memory T cells, because T-cell proliferation induced by anti-CD3 in the absence of co-stimulation was not inhibited by IL-10 [11, 12, 21]. We therefore aimed to analyze the effect of IL-10 on TCR-induced IFN-γ and IL-17 production by memory T-cell subpopulations.

First, we investigated the effect of IL-10 on freshly isolated non-CD14-depleted and CD14-depleted PBMC that were TCR-stimulated in the absence of co-stimulation. Under these circumstances, only memory and effector T cells should produce IFN-γ. Surprisingly, IL-10 inhibited anti-CD3-induced IFN-γ production in non-CD14-depleted and CD14-depleted PBMC to a similar extent as anti-CD3/anti-CD28-induced IFN-γ production (both with $p<0.05$, Fig. 3B). The same results were obtained for CD14-depleted and then $CD4^+$ re-purified T cells, which ruled out an effect of contaminating APC ($p<0.05$, Fig. 3B). On the other hand, anti-CD3-induced IL-17 production was not inhibited by IL-10 (data not shown). This suggested that IFN-γ, but not IL-17 production from memory T cells, was directly inhibited by IL-10.

To confirm this, we repeated the experiments with $CD4^+$ memory ($CD45RO^+$) and naïve ($CD45RA^+$) T-cell subpopulations. Again, IL-10 inhibited IFN-γ production in memory $CD4^+$ T cells to a similar extent as in highly re-purified $CD4^+$ cells ($p<0.05$, Fig. 3C) but had no effect on anti-CD3-induced IL-17 production (Fig. 3C). Presence or absence of exogenous IL-2 did

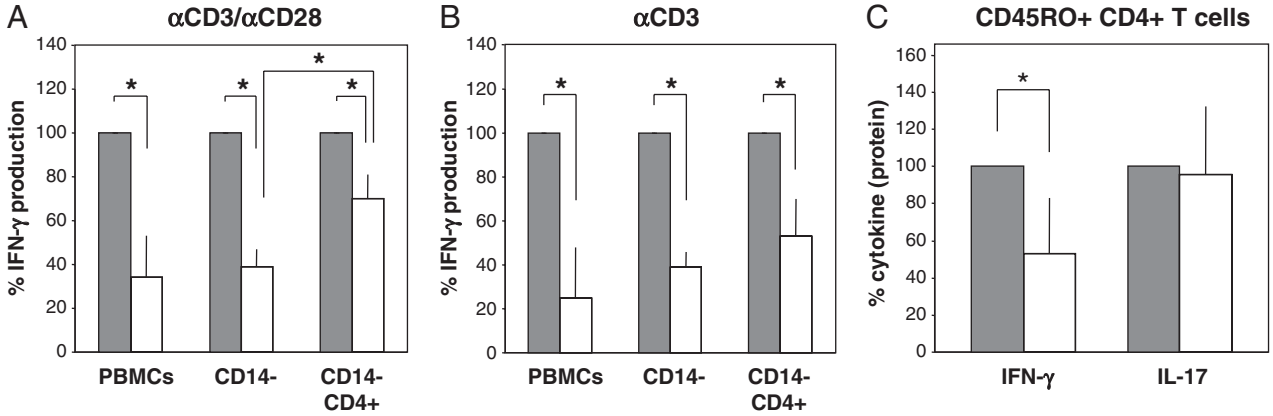

Figure 3. IL-10 directly inhibits TCR-induced IFN-γ production in the absence of APC and co-stimulation but has no influence on IL-17 production. PBMC from healthy blood donors were either used directly or depleted with anti-CD14-coated magnetic beads ($CD14^-$). $CD4^+$ T cells were further purified from CD14-depleted PBMC by $CD4^+$ selection to a purity of at least 99% ($CD14^-CD4^+$). For memory T-cell separation (C), $CD4^+$ cells were purified from PBMC by CD4-untouched magnetic separation. Then $CD45RO^+$ $CD4^+$ T cells were enriched by depleting $CD45RA^+$ cells. These different cell populations were activated with IL-2 (100 U/mL) and either (A) immobilised anti-CD3/anti-CD28 mAb (1 μg/mL each), or (B, C) immobilized anti-CD3 (1 μg/mL) for 24 h in the presence (white bars) or absence (gray bars) of IL-10 (10 ng/mL). Supernatants were collected thereafter and (A, B) IFN-γ production and (C) IFN-γ and IL-17 production was analyzed by ELISA. The amount of cytokine after respective stimulation without IL-10 was set to 100% for each individual donor and IL-10 inhibition related to this. In the absence of IL-10, the absolute values for IFN-γ (4–427 ng/mL for PBMC and 1.8–15.7 ng/mL for CD14-depleted and $CD4^+$ re-purified T cells) were comparable in the anti-CD3/anti-CD28-stimulated and only anti-CD3-stimulated samples. In memory $CD45RO^+$ $CD4^+$ T cells, in the absence of IL-10, the absolute values ranged from 4.6 to 15.5 ng/mL for IFN-γ and from 0.05 to 1.4 ng/mL for IL-17. Results shown are averages from five independent experiments (±SD). Significant differences as calculated by Wilcoxon test ($p<0.05$) are indicated by an asterisk (*).

© 2009 WILEY-VCH Verlag GmbH & Co. KGaA, Weinheim

not alter these results, and naïve CD4$^+$ T cells did neither produce significant amounts of IFN-γ nor IL-17 (data not shown).

Naïve and central memory T cells express CD28, but it becomes down-regulated in effector memory or effector T cells ([24, 25], and data not shown). Recently, Joss *et al*. postulated that the inhibitory effect of IL-10 on T cells is mediated *via* inhibition of CD28 signaling, indicating that only CD28$^+$ T cells would be inhibited by IL-10 [11]. To test this, we separated CD28$^-$ and CD28$^+$ cells from CD14-depleted PBMC, and determined IFN-γ concentrations in the supernatants of these cells after TCR-stimulation by anti-CD3/anti-CD28 incubation. Surprisingly, CD28$^-$ T cells produced a significant amount of IFN-γ after TCR-stimulation and were susceptible to inhibition by IL-10 (Fig. 4A). This suggested that IL-10 also affects the CD28$^-$ effector memory and effector T-cell subsets. To confirm these data by another approach, we stained CD28 and intracellular IFN-γ in TCR-stimulated, CD14-depleted PBMC (Fig. 4B). IL-10 reduced the number of IFN-γ-producing T cells within the CD28$^-$ T-cell population (3.1% of T cells compared with 8.3%) as much as in the CD28$^+$ T-cell population (3.2% of T cells compared with 7.0%) (Fig. 4B). However, IL-10 did not seem to significantly alter the amount of IFN-γ produced *per* cell (as measured by MFI, data not shown). We also analyzed the effect of IL-10 on IFN-γ production by the T-cell subsets expressing the activation markers CD25, HLA-DR and CD57, respectively. Similar to the results for CD28, the inhibition of IFN-γ production by IL-10 was comparable in T-cell subsets either positive or negative for these activation markers (data not shown).

In summary, in contrast to IL-17, TCR-induced IFN-γ production in CD4$^+$ memory T cells was inhibited by IL-10. Furthermore, the ability of IL-10 to inhibit IFN-γ production in CD28$^-$ T cells suggests a molecular mechanism, which is independent of CD28 co-stimulation.

IL-10 inhibition of TCR-induced IFN-γ production is not overcome by blocking SHP-1

A very recent study suggested that transient activation of the tyrosine phosphatase SHP-1 mediates the inhibitory effect of IL-10 on CD28- or ICOS-induced T-cell proliferation [12]. SHP-1 has also been described to interfere with TCR-induced ZAP-70 activation. Therefore, we wondered whether SHP-1 activation also plays a role in mediating the inhibition of anti-CD3-induced IFN-γ production by IL-10. To address this question, we first used the general phosphatase inhibitor pervanadate in our

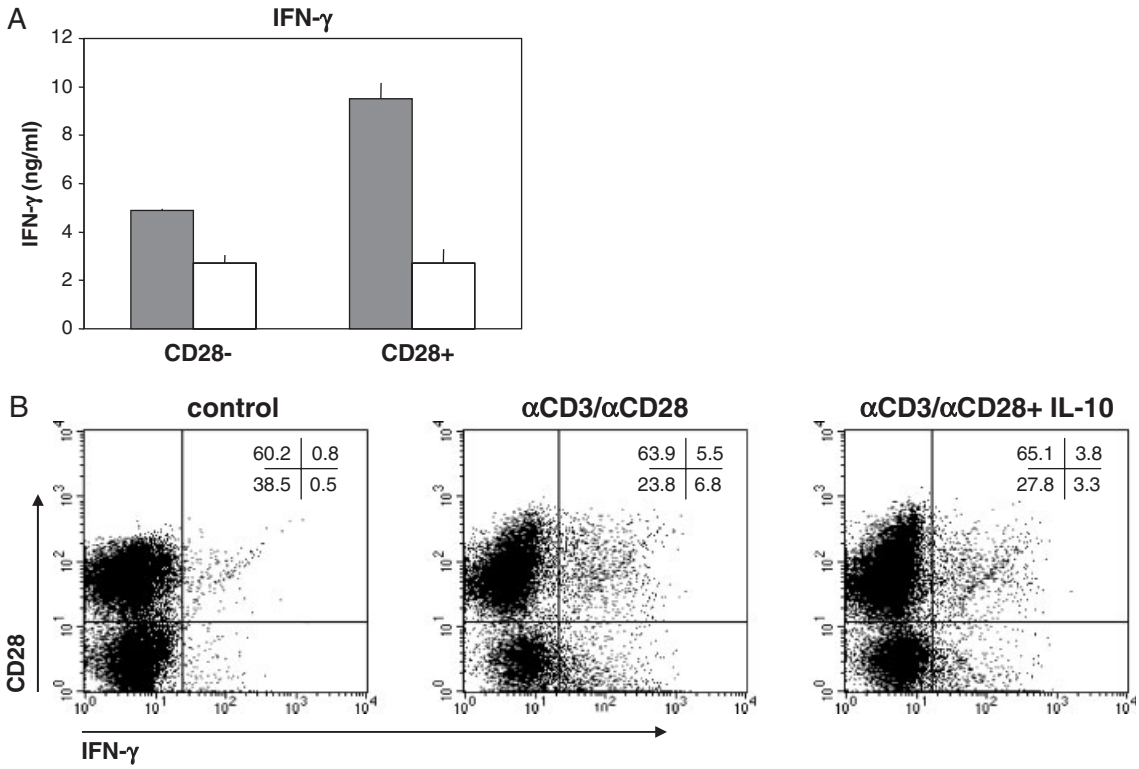

Figure 4. IL-10 inhibits TCR-induced IFN-γ production independently from CD28 expression. (A) Antigen-primed CD28$^-$ T cells were isolated by a two-step separation protocol. First, CD14$^+$ cells were depleted from PBMC and then CD28$^+$ cells were depleted from the remaining cells. The CD28$^+$ fraction was eluted for comparison. Then cytokine production was induced by immobilized anti-CD3/anti-CD28 (each 1 μg/mL) and IL-2 (100 U/mL) in the presence (white bars) or absence (gray bars) of IL-10 (10 ng/mL). Results shown are averages from three independent experiments (±SD). (B) CD14-depleted PBMC were stimulated for 30 h by immobilized anti-CD3 and anti-CD28 (each 1 μg/mL) and IL-2 (100 U/mL) in the presence or absence of IL-10 (10 ng/mL). After addition of Brefeldin A 6 h prior to the end of culture, cells were stained for surface anti-CD3 and anti-CD28 and intracellular IFN-γ expression and analyzed by flow cytometry. CD3-gated T cells are depicted from one out of two experiments. Control cells incubated with IL-10 only did not show IFN-γ production (data not shown).

© 2009 WILEY-VCH Verlag GmbH & Co. KGaA, Weinheim

experiments. Interestingly, non-stimulated T cells produced large amounts of IFN-γ in the presence of the inhibitor. In contrast, TCR-induced IFN-γ production was reduced to levels of IL-10 inhibition which both made it very difficult to interpretate these results (data not shown).

We therefore next used the specific, irreversible SHP-1 inhibitor sodium stibogluconate [26] to interfere only with SHP-1 activity. PBMC treated with this inhibitor did not produce IFN-γ spontaneously and responded normally toward TCR-stimulation. Inhibition of SHP-1 did not overcome the effect of IL-10 on TCR-induced IFN-γ production (Fig. 5A). This was the case for TCR-stimulation with anti-CD3 alone, as well as in the presence of additional co-stimulation with anti-CD28 (Fig. 5A). Even higher concentrations of sodium stibogluconate (50 μg/mL) did not abrogate the IL-10 inhibitory effect (data not shown). The activity of the inhibitor was shown by enhancement of IFN-α-induced STAT-1 activation in T-cells (Fig. 5B). These data suggest that IL-10 uses a SHP-1-independent mechanism for inhibiting TCR-induced IFN-γ production.

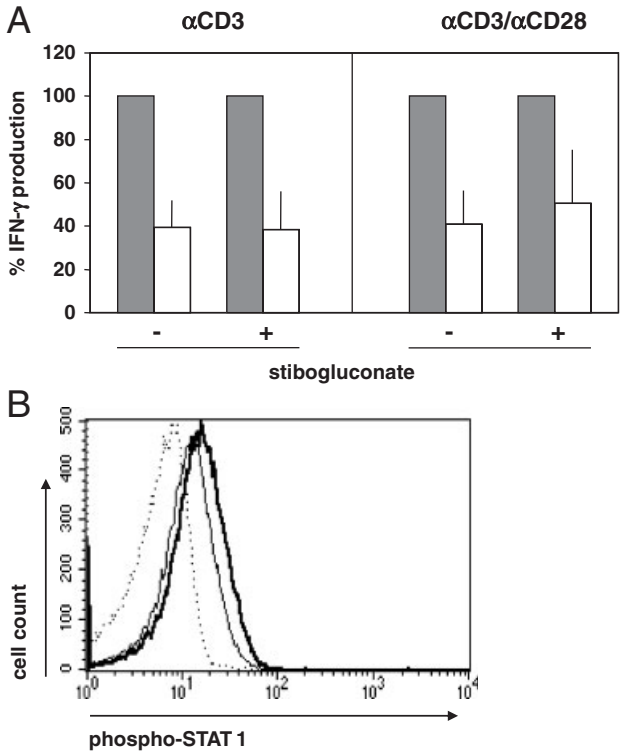

Figure 5. Inhibition of SHP-1 does not abolish IL-10-induced inhibition on TCR-stimulated IFN-γ production. (A) Human PBMC from healthy blood donors were left untreated or incubated with the irreversible SHP-1 inhibitor sodium stibogluconate (10 μg/mL) for 10 min. The cells were then activated with immobilised anti-CD3/anti-CD28 mAb (1 μg/mL each) or anti-CD3 (1 μg/mL) and IL-2 (100 U/mL) for 24 h in the presence (white bars) or absence (gray bars) of IL-10 (10 ng/mL). Supernatants were collected thereafter and IFN-γ analyzed by ELISA. Because of donor-specific differences for absolute cytokine levels, the amount of IFN-γ after anti-CD3/anti-CD28 or anti-CD3 treatment was set to 100% for each individual donor and IL-10 inhibition related to this. In the absence of IL-10, the absolute values for IFN-γ following anti-CD3 stimulation ranged from 3 to 31.5 ng/mL and similar values were obtained with anti-CD3/anti-CD28 stimulation and in the presence of stibogluconate, respectively. Results shown are averages from four independent experiments (±SD). (B) Freshly isolated PBMC were either left untreated (thin line) or pre-incubated with the SHP-1 inhibitor sodium stibogluconate (10 μg/mL; bold line) for 10 min and then treated with IFN-α for 2 h. PBMC without IFN-α treatment served as control (dotted line). Cells were then fixed and lysed and STAT1-phosphorylation was assessed by flow cytometry after co-staining of surface CD3 expression and intracellular staining of p-STAT1.

IL-10 inhibition of IFN-γ is lost by *in vitro* culture despite intact signalling

Next, we wondered whether recently activated T cells, which occur in acute infection and to an even greater extent in chronic inflammation, are susceptible to the inhibitory effect of IL-10 on IFN-γ production. It has been suggested that IL-10RI expression is down-regulated after TCR activation [14], which should lead to a loss of IL-10 responsiveness in recently activated T cells. Therefore, we incubated PBMC for 24–48 h in the presence of anti-CD3/anti-CD28 mAb and IL-2 to achieve pre-activation, and then studied the influence of IL-10 on IFN-γ production after re-stimulation with anti-CD3 and anti-CD28 mAb. In agreement with other reports, we did not observe an inhibitory effect of IL-10 on IFN-γ production by these freshly pre-activated T cells (Fig. 6A). Surprisingly, T cells cultured *in vitro* without pre-stimulation also lost their responsiveness toward IL-10. This led us to the conclusion that the unresponsiveness to the inhibitory effect of IL-10 on freshly pre-activated T cells is likely to be an *in vitro*-culture artifact rather than a stimulation-induced effect. Interestingly, despite the lack of an effect of IL-10 on IFN-γ production, the *in vitro* pre-activated T cells responded normally to IL-10-induced SOCS-3 mRNA induction (Fig. 6B) and STAT3 activation (Fig. 6C).

Th17 cells have intact IL-10 signalling

As we could observe an inhibitory effect of IL-10 on IFN-γ but not on IL-17 production from freshly isolated antigen experienced T cells, we next wondered whether Th17 cells might be unresponsive to IL-10 because they would have, *e.g.* lost IL-10 receptor expression during differentiation. We tried to address this question by measuring STAT3 activation in Th17 cells by intracellular FACS-staining with phospho-specific antibodies after 20 min of IL-10 stimulation. Several surface markers have been described to identify human Th17 cells with the IL-23 receptor expressing CCR4/CCR6 double-positive T cells being highly specific for IL-17 production [27–29]. We used therefore either antibodies against surface IL-23 receptor on $CD3^+$ T cells or gated for CCR4/CCR6 double-positive T cells to measure intracellular STAT3 activation in Th17 cells by IL-10. Surprisingly, Th17 cells mounted a normal STAT3 activation upon IL-10 stimulation (Fig. 7A). In order to analyze IL-10 target gene expression in Th17 cells, we enriched for Th17 cells by magnetic beads with

© 2009 WILEY-VCH Verlag GmbH & Co. KGaA, Weinheim

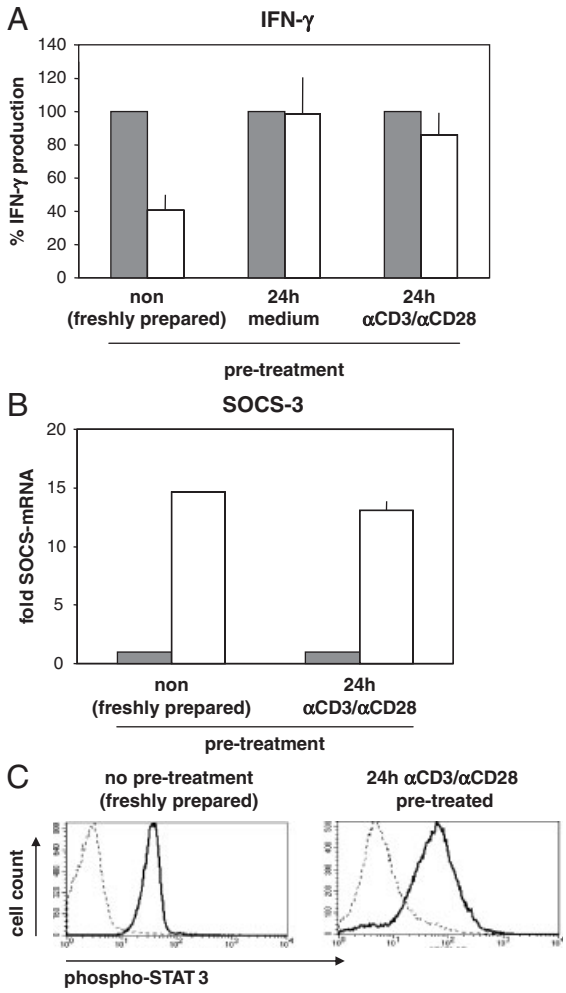

Figure 6. Loss of IFN-γ inhibitory effect of IL-10 after *in vitro* culture. (A) PBMC were either left untreated for 24 h (24 h medium) or pre-activated with immobilised anti-CD3/anti-CD28 mAb (1 μg/mL each) and IL-2 (100 U/mL) for 24 h (24 h anti-CD3/anti-CD28) followed by overnight starvation in 0.5% FCS-containing medium and washing. Production of IFN-γ was induced by immobilised 24 h anti-CD3/anti-CD28 mAb (1 μg/mL each) or anti-CD3 (1 μg/mL) and IL-2 (100 U/mL) for 24 h in the presence (white bars) or absence (gray bars) of IL-10 (10 ng/mL). As a positive control, freshly isolated PBMC from the same donor were stimulated directly. Supernatants were collected thereafter and IFN-γ measured by ELISA. The amount of IFN-γ after 24 h anti-CD3/anti-CD28 or anti-CD3 treatment was set to 100% for each individual donor and IL-10 inhibition was related to this. The absolute values for IFN-γ ranged from 9 to 115 ng/mL in the absence of IL-10 and were similar between freshly prepared and pre-treated cells. Results shown are averages from three independent experiments (±SD). (B) CD14-depleted PBMC were either used freshly prepared or pre-activated (24 h anti-CD3/anti-CD28) as described in (A). The cells were then either left untreated (gray bars) or incubated with IL-10 (10 ng/mL) for 1 h (white bars). Afterwards, $CD3^+$ cells were isolated and RNA was extracted from these cells. SOCS-3 levels were determined using Real-Time RT-PCR with HPRT as reference panel. The SOCS-3 mRNA levels of cells in the absence of IL-10 were set as 1 and the IL-10 induction of SOCS-3 related to this. Results shown are averages from two independent experiments (±SD). (C) Freshly isolated or 24 h anti-CD3/anti-CD28 pre-activated CD14-depleted PBMC as described in (A) were either left untreated (dotted lines) or incubated with IL-10 (10 ng/mL) in serum-free medium for 5 min (bold lines). Cells were then fixed and lysed and STAT3-phosphorylation was assessed by flow cytometry after co-staining of surface CD4 expression and intracellular staining of p-STAT3.

anti-IL-23R after CD14 depletion. Intracellular FACS-staining revealed that indeed these $CD3^+$ IL-$23R^+$ T cells are producers of IL-17 and that they produce little, if any, IFN-γ (Fig. 7B). In line with the observation that IL-10 is able to induce STAT3 activation in Th17 cells, we also observed an induction of its target gene SOCS-3 in these IL-23R-enriched T cells (Fig. 7C). These results together suggest that Th17 cells are fully responsive toward IL-10 but this does not result in inhibition of IL-17 production.

Discussion

The anti-inflammatory properties of IL-10 have been well described in the past. It targets the induction of various pro-inflammatory mediators as well as antigen presentation and thereby indirectly inhibits T-cell responses. *In vivo*, the lack of IL-10 in IL-10-deficient mice leads to the development of chronic inflammation in the form of colitis [30]. Because of its potent anti-inflammatory properties, IL-10 was used with high expectations in therapeutic trials for a number of chronic inflammatory diseases, which were thought to be driven by an excessive Th1 response (reviewed in [13]). However, despite some beneficial effects – particularly in psoriasis [31]– IL-10 therapy did not compare favorably to other biologicals, such as for example, anti-TNF-α therapy. This was rather surprising because IL-10 targets a wide range of inflammatory mediators in addition to TNF-α.

However, most *in vitro* studies have described inhibitory effects of IL-10 on the induction of an inflammatory immune response, but not on an ongoing or chronic inflammation. We therefore wanted to analyze whether IL-10 is able to inhibit an already established memory or effector T-cell response. In contrast to naïve T cells, memory and effector T cells respond to TCR engagement in the absence of co-stimulation. Furthermore, effector cytokine production occurs rapidly within 24 h after stimulation, because necessary epigenetic changes have already been established [32, 33]. To our surprise, IL-10 was able to directly inhibit TCR-induced IFN-γ production in memory T cells. This was evident from several observations: (i) The time frame for IFN-γ production in our direct TCR-triggered model was 24 h. Within this time frame, mainly memory and effector T cells respond, because naïve T cells have to proliferate first before they can produce IFN-γ. (ii) In contrast to previous reports on proliferation [11, 12], IL-10 inhibited IFN-γ production induced by anti-CD3 cross-linking without co-stimulation – a condition where only memory T cells should respond. (iii) In agreement with this, under the same conditions, isolated memory T cells (either $CD4^+$ $CD45RO^+$ T cells or $CD28^-$ effector/effector memory T cells) were inhibited by IL-10. (iv) Intracellular staining for IFN-γ production revealed that all of the investigated T-cell subsets were susceptible to inhibition by IL-10, including T cells with activation and memory markers. The latter is especially interesting with respect to $CD28^-$ T cells, as uncoupling of CD28 signaling has been suggested to mediate the direct inhibitory effect of IL-10 on T cells [11, 12]

© 2009 WILEY-VCH Verlag GmbH & Co. KGaA, Weinheim

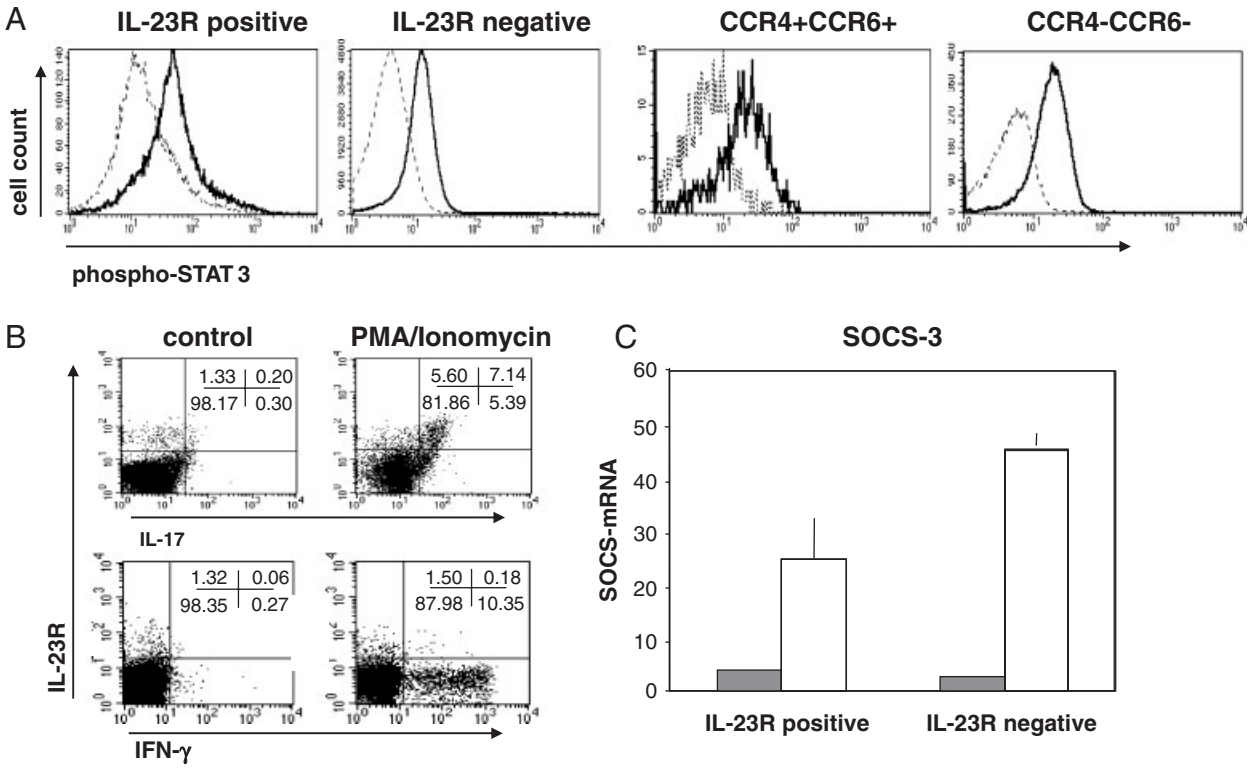

Figure 7. IL-10 induces STAT3 activation in Th17 cells. (A) Freshly isolated PBMC were either left untreated (dotted lines) or incubated with IL-10 (10 ng/mL) in serum-free medium for 20 min (bold lines) at 37°C. STAT3-phosphorylation was assessed by flow cytometry after co-staining of surface CD3 and IL-23R or CCR4 and CCR6 expression and intracellular staining of p-STAT3. Results are depicted in a histogram, which represents one out of three independent experiments. (B) Freshly isolated PBMC were either left unstimulated or stimulated with PMA and ionomycin for 15 h. The production of IFN-γ and IL-17 was assessed by flow cytometry after co-staining of surface CD3 and IL-23R expression and intracellular staining of IFN-γ and IL-17. CD3-gated T cells are depicted from one out of three experiments. (C) CD14-depleted and then IL-23 receptor-positive separated PBMC were either left untreated (gray bars) or incubated with IL-10 (10 ng/mL) for 1 h (white bars). Afterwards, RNA was extracted from these cells. SOCS-3 levels were determined using Real-Time RT-PCR with HPRT as reference panel. Results shown are averages from two independent experiments (±SD).

We furthermore showed that inhibition of anti-CD3-induced IFN-γ production by IL-10 (i) is independent from APC, which is in contrast to IL-12/IL-18-induced IFN-γ production [8], and (ii) is independent from IL-2 inhibition which was suggested to be another mechanism by which IL-10 directly inhibited T cells [9, 10, 34]. Fitting to the missing effect of IL-10 on IL-17 production (see below), receptor-proximal signaling events by IL-10 were not abrogated by the selective SHP-1 inhibitor stibogluconate, and we hypothesize a specific direct inhibitory mechanism of IL-10 on TCR-mediated IFN-γ production independent from (i) CD28 signaling, and (ii) inhibition of IL-2 production, which remains to be elucidated.

In contrast to IFN-γ, TCR-induced IL-17 production was unaffected by IL-10. Interestingly, Th17 cells did respond toward IL-10 stimulation with the activation of STAT3 excluding general unresponsiveness of Th17 cells toward IL-10. It has remained elusive why IL-10 therapy in chronic inflammatory diseases has been rather disappointing. In recent years, evidence is emerging that IL-17 production by Th17 cells, rather than IFN-γ production by Th1 cells, greatly accounts for the pathology in chronic inflammation (reviewed in [17, 18]). Our data suggest that the ability of IL-10 to stop a chronic inflammation caused by Th17 memory cells might be limited. However, it is well established that IL-10 can repress the production of major inducers of a Th17 response. IL-10 inhibits IL-6 expression [6] and the expression of the common p40 subunit [7] shared by IL-12 and IL-23 [35]. Interestingly, colitis caused by IL-10 deficiency can be prevented by depleting IL-23 [36] demonstrating that IL-10 can control the induction of an inflammatory IL-17 response. In contrast to IL-6 and IL-23, IL-10 does not inhibit TGF-β production but rather induces its activity [37, 38] and TGF-β has been associated with the generation of regulatory T cells (reviewed in [39]). Thus we speculate that although IL-10 may only partly be able to interfere with an already established inflammatory process, it may favor the induction of regulatory T cells instead of Th17 cells in the primary response to an inflammatory stimulus. Compatible with this hypothesis are findings in psoriatic patients treated with IL-10 for relapse prevention: a significant, decreased relapse rate could be seen, indicating that IL-10 application may be successful

© 2009 WILEY-VCH Verlag GmbH & Co. KGaA, Weinheim

in preventing rather than in reverting an already established inflammatory immune response [40].

In conclusion, our results suggest that in contrast to inhibition of Th1 responses, IL-10 has its limitation in inhibiting an already established and ongoing Th17-driven chronic inflammation. Taken together with data published by other groups, IL-10 however may be able to prevent the induction of a Th17 response. These results should have implications for the therapeutic use of IL-10 in inflammatory diseases. Firstly, they suggest that IL-10 therapy should be promising for inflammatory diseases that are solely caused by an ongoing excessive Th1 response. Secondly, it might be still possible to use IL-10 in Th17-driven diseases, but only in combination with conventional or anti-TNF therapy stopping the ongoing inflammatory process. In that case, IL-10 should be able to prevent a relapse.

Materials and methods

Cell culture and stimulation

Human PBMC were isolated from citrate anti-coagulated blood of healthy volunteers by Ficoll-Paque density gradient centrifugation and cultured at a cell density of 1×10^6 cells/mL in *Roswell Park Memorial Institute* 1640 medium supplemented with FCS (10% v/v), L-glutamine (2 mM) and penicillin/streptomycin (each at 10 000 U/mL) (all Biochrom KG, Germany). All healthy volunteers participated on a voluntary basis and gave written informed consent.

Antigen-dependent stimulation of cytokine production was performed by stimulating PBMC (2×10^6/mL) with *C. albicans* (dilution of 1/1000; Stallergenes GmbH, Germany) in the presence or absence of IL-10 (10 ng/mL; R&D Biosystems, Germany). After 72 h, supernatants were harvested and IFN-γ and IL-17 concentrations were determined using commercially available ELISA (R&D Biosystems). For TCR-induced cytokine production, PBMC or isolated T cells (1×10^6 cells/mL) were stimulated with plate-bound anti-CD3 (OKT3, 1 μg/mL; Jansen-Cilag GmbH, Germany) alone or when indicated in combination with plate-bound anti-CD28 (L293, 1 μg/mL; BD Bioscience, Germany) and IL-2 (100 IU/mL; R&D Biosystems) in the presence or absence of IL-10 (10 ng/mL). After 24 h, supernatants were harvested and IFN-γ and IL-17 concentrations were determined using commercially available ELISA (R&D Biosystems).

If pre-activated PBMC were used, PBMC were pre-stimulated for 24 h with immobilized anti-CD3/anti-CD28 mAb (1 μg/mL each) and IL-2 (100 IU/mL). They were then washed and starved overnight in *Roswell Park Memorial Institute* medium containing 0.5% FCS v/v before being re-stimulated with anti-CD3/anti-CD28 mAb in the presence or absence of IL-10 (10 ng/mL). As control, instead of pre-stimulation, cells were left untreated for 24 h and then re-stimulated under the same conditions. Twenty-four hours after re-stimulation, cells were harvested and supernatants were analyzed for IFN-γ or IL-17 production by ELISA.

Cell separation

Monocytes were depleted from PBMC by using anti-CD14-coated magnetic MACS™ beads (Miltenyi Biotech GmbH, Germany) following the manufacturer's protocol. Cell purity was confirmed by flow cytometry ($CD14^+$ cells < 0.5%). For highly purified $CD4^+$ T cells, CD14-depleted PBMC were re-purified with anti-CD4-coated MACS™ beads (Miltenyi Biotech GmbH). Purity of $CD4^+$ T cells was > 99% in the life cell gate. For isolation of $CD4^+$ memory T cells, first $CD4^+$ T cells were separated from PBMC with CD4-untouched MACS™ beads and then further separated either for $CD45RO^+$ cells (memory $CD4^+$ T cells) *via* depletion of $CD45RA^+$ cells or for $CD45RA^+$ cells (naïve $CD4^+$ T cells) *via* depletion of $CD45RO^+$ cells using the MACS™ system (Miltenyi Biotech GmbH). Separation of $CD28^-$ and $CD28^+$ cells was performed with anti-CD28-coated MACS™ beads (Miltenyi Biotech GmbH) after CD14 depletion from PBMC. Separation of IL-$23R^+$ cells was performed with anti-FITC-coated MACS™ beads (Miltenyi Biotech GmbH) after CD14 depletion from PBMC and labeling with anti-IL-23R-FITC antibody (R&D Biosystems).

Measurement of PBMC proliferation with CFSE

PBMC were re-suspended at 1×10^7 cells/mL in PBS containing 5 μM CFSE (Molecular Probes/Invitrogen, USA). After 5 min incubation at room temperature, cells were washed twice with culture medium. Then cells were stimulated at a concentration of 1×10^6 cells/mL with immobilized anti-CD3 Ab (1 μg/mL) and anti-CD28 Ab (1 μg/mL), with or without IL-2 (100 U/mL), in the presence or absence of IL-10 (10 ng/mL) for 5 days. Cells were finally analyzed using a FACScalibur flow cytometer (Becton Dickinson, Germany) and CellQuest software (Becton Dickinson).

Analysis of intracellular cytokine production by flow cytometry

PBMC (2×10^6) or respective isolated T-cell subsets were stimulated with immobilized anti-CD3/anti-CD28 (each at 1 μg/mL) and IL-2 (100 U/mL), in the presence or absence of IL-10 (10 ng/mL) for 30 h. After 24 h, Brefeldin A (10 μg/mL; Sigma, Germany) was added for the last 6 h. For analysis of IL-$23R^+$ T cells, PBMC were stimulated with PMA (10 ng/mL; Sigma), ionomycin (0.5 μg/mL; Sigma) and Brefeldin A for 15 h. Following stimulation, cells were harvested, washed in PBS and incubated for 30 min at 4°C in the dark with the following monoclonal antibodies: anti-HLA-DR (L243; Becton Dickinson), anti-CD3 (SK7; Becton Dickinson), anti-CD8 (SK1; Becton Dickinson), anti-CD25 (2A3; Becton Dickinson), anti-CD57 (NC1; Beckman-Coulter), anti-CD28 (CD28.2; Beckman-Coulter), anti-CD4 (SK3; Becton Dickinson), anti-CD45RO (Leu-45RO; Becton Dickinson), anti-CD45RA (HI100; Becton Dickinson), anti-IL-23R (R&D Biosystems). Fluorochrome

© 2009 WILEY-VCH Verlag GmbH & Co. KGaA, Weinheim

combinations were chosen to allow for analysis of co-staining of respective antigens. All antibodies were used in saturating amounts. Cells were then washed once in PBS containing 2% v/v FCS and 0.1% w/v NaN_2 prior to fixation and permeabilization with 500 μL Cytofix/Cytoperm solution (Becton Dickinson) for 10 min at room temperature in darkness. Cells were washed once again and incubated with blocking buffer (100 μL PBS/10% v/v human AB serum; both Sigma) for 20 min at 4°C in the dark to prevent unspecific binding of the anti-cytokine monoclonal antibody. After another washing step, 10 μL of anti-IFN-γ-FITC (25723.11; Becton Dickinson) or anti-IL-17A-PE (eBio64DEC17; eBioscience, Germany) were added and cells were incubated for 30 min at 4°C in darkness followed by a final washing step prior to measurement. Measurement was done using four-color flow cytometry on a FACS Calibur (Becton Dickinson; at least 50 000 $CD3^+$ lymphocytes were collected). Data were analyzed using CellQuest (Becton Dickinson). T-cell gating was done using side scatter and CD3-staining properties.

Analysis of phospho-STAT3 and phospho-STAT1 induction by flow cytometry

Freshly isolated PBMC or pre-activated PBMC (of the same donor) were incubated for 20 min with or without IL-10 (10 ng/mL). Then cells were stained with anti-IL-23 R-FITC and fixed with Cytofix Buffer (Becton Dickinson) for 10 min at 37°C and permeabilized with Phosflow Perm Buffer (Becton Dickinson) for 30 min on ice. For surface staining of CCR4 and CCR6, PBMC were first stained with anti-CCR6-PE (11A9, Becton Dickinson) and anti-CCR4-FITC (R&D Biosystems) and then incubated for 20 min with or without IL-10 (10 ng/mL), fixed with Cytofix Buffer for 10 min at 37°C and permeabilized with Phosflow Perm Buffer for 30 min on ice.

For induction of STAT1 tyrosine phosphorylation, PBMC were incubated with IFN-α2a (0.1 ng/mL; Miltenyi Biotech GmbH) for 2 h, then fixed with Cytofix Buffer for 10 min at 37°C and permeabilized with Phosflow Perm Buffer for 30 min on ice. Cells were washed and anti-CD3-PerCP (SK7, Becton Dickinson) and anti-Stat3 (pY705)-PE (4/P Stat3, Becton Dickinson) or anti-Stat3 (pY705)-FITC (4/P Stat3, Becton Dickinson) or anti-Stat1 (pY701)-FITC (Becton Dickinson) were added and incubated for 30 min at room temperature in the dark. Cells were analyzed using a FACS Calibur flow cytometer and CellQuest software.

Analysis of cytokine and SOCS-3 mRNA induction

Total RNA was isolated for cytokine mRNA quantification with Absolute mRNA Micro Kits (Stratagene, Germany) after 24 h of TCR-stimulation by immobilized anti-CD3/anti-CD28 (each 1 μg/mL) in the presence or absence of IL-10 (10 ng/mL). mRNA was transcribed into cDNA with Moloney murine leukemia virus Reverse Transcriptase (Gibco BRL, US) and oligodT Primers (GE Healthcare, Germany). Quantitative Real-Time RT-PCR for IFN-γ and IL-17 was performed with specific primers and probes from Applied Biosystems (Germany) using the ABI prism 7700 sequence detector (Applied Biosystems) and hypoxanthine phosphoribosyltransferase (HPRT) as reference panel. For analysis of SOCS-3 induction, PBMC were stimulated with anti-CD3/anti-CD28 (1 μg/mL) and IL-2 (100 U/mL) for 24 h. They were then washed and starved overnight before stimulation with anti-CD28 and/or anti-CD3 mAb in the presence or absence of IL-10 (10 ng/mL). Cells were harvested after 1 h, $CD3^+$ cells were isolated by magnetic MACS™ beads and total RNA was extracted from these cells. For analysis of SOCS-3 induction in separated IL-23R^+ cells, the cells were stimulated with anti-CD3/anti-CD28 mAb in the presence or absence of IL-10 (10 ng/mL) for 1 h and then total RNA was extracted. SOCS levels were determined after reverse transcription by Real-Time RT-PCR with HPRT as reference panel. SOCS-3 sense: ctttctgatccgcgacagct, SOCS-3 anti-sense: tcacactggatgcgcaggt, SOCS-3 probe: ccagcgccacttcttcacgctcag.

Statistical analysis

If not stated otherwise, data are presented as mean ± SD values. For ELISA data, cytokine production of TCR-stimulated cells was set at 100% in each individual experiment. All other samples from the same experiment were expressed as percentages relating to this. This was done because of large inter-individual variations in absolute cytokine levels. The average and standard deviation was determined from 3–5 independent experiments. Statistical analysis was done for experiments with at least five independent donors by using the Wilcoxon matched-pairs signed-ranked test and SPSS software (USA). *p*-values (two-tailed) below 0.05 were considered as significant.

Acknowledgements: We would like to thank Christian Meisel and Wolf-Dietrich Döcke for helpful discussions. This work was supported in part by the Deutsche Forschungsgemeinschaft (DFG), SFB421-TPB2 and B9. Nimisha Suman was funded by a Ph.D. fellowship of the Charité-Universitätsmedizin Berlin.

Conflict of interest: The authors declare no financial or commercial conflict of interest.

References

1 **Fiorentino, D. F., Zlotnik, A., Vieira, P., Mosmann, T. R., Howard, M., Moore, K. W. and O'Garra, A.,** IL-10 acts on the antigen-presenting cell to inhibit cytokine production by Th1 cells. *J. Immunol.* 1991. **146**: 3444–3451.

2 **de Waal Malefyt, R., Haanen, J., Spits, H., Roncarolo, M., te Velde, A., Figdor, C., Johnson, K. *et al.*,** Interleukin 10 (IL-10) and viral IL-10 strongly

© 2009 WILEY-VCH Verlag GmbH & Co. KGaA, Weinheim

reduce antigen-specific human T cell proliferation by diminishing the antigen-presenting capacity of monocytes via downregulation of class II major histocompatibility complex expression. *J. Exp. Med.* 1991. **174**: 915–924.

3 **Ding, L., Linsley, P., Huang, L., Germain, R. and Shevach, E.,** IL-10 inhibits macrophage costimulatory activity by selectively inhibiting the up-regulation of B7 expression. *J. Immunol.* 1993. **151**: 1224–1234.

4 **Willems, F., Marchant, A., Delville, J. P., Gerard, C., Delvaux, A., Velu, T., de Boer, M. and Goldman, M.,** Interleukin-10 inhibits B7 and intercellular adhesion molecule-1 expression on human monocytes. *Eur. J. Immunol.* 1994. **24**: 1007–1009.

5 **de Waal Malefyt, R., Abrams, J., Bennett, B., Figdor, C. G. and de Vries, J. E.,** Interleukin 10(IL-10) inhibits cytokine synthesis by human monocytes: an autoregulatory role of IL-10 produced by monocytes. *J. Exp. Med.* 1991. **174**: 1209–1220.

6 **Fiorentino, D. F., Zlotnik, A., Mosmann, T. R., Howard, M. and O'Garra, A.,** IL-10 inhibits cytokine production by activated macrophages. *J. Immunol.* 1991. **147**: 3815–3822.

7 **D'Andrea, A., Aste-Amezaga, M., Valiante, N. M., Ma, X., Kubin, M. and Trinchieri, G.,** Interleukin 10 (IL-10) inhibits human lymphocyte interferon gamma-production by suppressing natural killer cell stimulatory factor/IL-12 synthesis in accessory cells. *J. Exp. Med.* 1993. **178**: 1041–1048.

8 **Schroder, M., Meisel, C., Buhl, K., Profanter, N., Sievert, N., Volk, H. D. and Grutz, G.,** Different modes of IL-10 and TGF-beta to inhibit cytokine-dependent IFN-gamma production: consequences for reversal of lipopolysaccharide desensitization. *J. Immunol.* 2003. **170**: 5260–5267.

9 **Taga, K., Mostowski, H. and Tosato, G.,** Human interleukin-10 can directly inhibit T-cell growth. *Blood* 1993. **81**: 2964–2971.

10 **de Waal Malefyt, R., Yssel, H. and de Vries, J. E.,** Direct effects of IL-10 on subsets of human CD4+T cell clones and resting T cells. Specific inhibition of IL-2 production and proliferation. *J. Immunol.* 1993. **150**: 4754–4765.

11 **Joss, A., Akdis, M., Faith, A., Blaser, K. and Akdis, C. A.,** IL-10 directly acts on T cells by specifically altering the CD28 co-stimulation pathway. *Eur. J. Immunol.* 2000. **30**: 1683–1690.

12 **Taylor, A., Akdis, M., Joss, A., Akkoc, T., Wenig, R., Colonna, M., Daigle, I. *et al.*,** IL-10 inhibits CD28 and ICOS costimulations of T cells via src homology 2 domain-containing protein tyrosine phosphatase 1. *J. Allergy Clin. Immunol.* 2007. **120**: 76–83.

13 **Asadullah, K., Sterry, W. and Volk, H. D.,** Interleukin-10 therapy – review of a new approach. *Pharmacol. Rev.* 2003. **55**: 241–269.

14 **Liu, Y., Wei, S. H., Ho, A. S., de Waal Malefyt, R. and Moore, K. W.,** Expression cloning and characterization of a human IL-10 receptor. *J. Immunol.* 1994. **152**: 1821–1829.

15 **Sawitzki, B., Kingsley, C. I., Oliveira, V., Karim, M., Herber, M. and Wood, K. J.,** IFN-gamma production by alloantigen-reactive regulatory T cells is important for their regulatory function in vivo. *J. Exp. Med.* 2005. **201**: 1925–1935.

16 **Feuerer, M., Eulenburg, K., Loddenkemper, C., Hamann, A. and Huehn, J.,** Self-limitation of Th1-mediated inflammation by IFN-gamma. *J. Immunol.* 2006. **176**: 2857–2863.

17 **Kikly, K., Liu, L., Na, S. and Sedgwick, J. D.,** The IL-23/Th(17) axis: therapeutic targets for autoimmune inflammation. *Curr. Opin. Immunol.* 2006. **18**: 670–675.

18 **Bettelli, E., Oukka, M. and Kuchroo, V. K.,** T(H)-17 cells in the circle of immunity and autoimmunity. *Nat. Immunol.* 2007. **8**: 345–350.

19 **Stumhofer, J. S., Laurence, A., Wilson, E. H., Huang, E., Tato, C. M., Johnson, L. M., Villarino, A. V. *et al.*,** Interleukin 27 negatively regulates the development of interleukin 17-producing T helper cells during chronic inflammation of the central nervous system. *Nat. Immunol.* 2006. **7**: 937–945.

20 **Elias, K. M., Laurence, A., Davidson, T. S., Stephens, G., Kanno, Y., Shevach, E. M. and O'Shea, J. J.,** Retinoic acid inhibits Th17 polarization and enhances FoxP3 expression through a Stat-3/Stat-5 independent signaling pathway. *Blood* 2008. **111**: 1013–1020.

21 **Akdis, C. A., Joss, A., Akdis, M., Faith, A. and Blaser, K.,** A molecular basis for T cell suppression by IL-10: CD28-associated IL-10 receptor inhibits CD28 tyrosine phosphorylation and phosphatidylinositol 3-kinase binding. *FASEB J.* 2000. **14**: 1666–1668.

22 **Hodge, D. L., Martinez, A., Julias, J. G., Taylor, L. S. and Young, H. A.,** Regulation of nuclear gamma interferon gene expression by interleukin 12 (IL-12) and IL-2 represents a novel form of posttranscriptional control. *Mol. Cell. Biol.* 2002. **22**: 1742–1753.

23 **Sawitzki, B., Kieselbach, B., Fisser, M., Meisel, C., Vogt, K., Gaestel, M., Lehmann, M. *et al.*,** IFN-gamma regulation in anti-CD4 antibody-induced T cell unresponsiveness. *J. Am. Soc. Nephrol.* 2004. **15**: 695–703.

24 **Appay, V., Dunbar, P. R., Callan, M., Klenerman, P., Gillespie, G. M., Papagno, L., Ogg, G. S. *et al.*,** Memory CD8+T cells vary in differentiation phenotype in different persistent virus infections. *Nat. Med.* 2002. **8**: 379–385.

25 **Amyes, E., McMichael, A. J. and Callan, M. F.,** Human CD4+T cells are predominantly distributed among six phenotypically and functionally distinct subsets. *J. Immunol.* 2005. **175**: 5765–5773.

26 **Pathak, M. K. and Yi, T.,** Sodium stibogluconate is a potent inhibitor of protein tyrosine phosphatases and augments cytokine responses in hemopoietic cell lines. *J. Immunol.* 2001. **167**: 3391–3397.

27 **Acosta-Rodriguez, E. V., Rivino, L., Geginat, J., Jarrossay, D., Gattorno, M., Lanzavecchia, A., Sallusto, F. and Napolitani, G.,** Surface phenotype and antigenic specificity of human interleukin 17-producing T helper memory cells. *Nat. Immunol.* 2007. **8**: 639–646.

28 **Cosmi, L., De Palma, R., Santarlasci, V., Maggi, L., Capone, M., Frosali, F., Rodolico, G. *et al.*,** Human interleukin 17-producing cells originate from a CD161+CD4+T cell precursor. *J. Exp. Med.* 2008. **205**: 1903–1916.

29 **Annunziato, F., Cosmi, L., Santarlasci, V., Maggi, L., Liotta, F., Mazzinghi, B., Parente, E. *et al.*,** Phenotypic and functional features of human Th17 cells. *J. Exp. Med.* 2007. **204**: 1849–1861.

30 **Kuhn, R., Lohler, J., Rennick, D., Rajewsky, K. and Muller, W.,** Interleukin-10-deficient mice develop chronic enterocolitis. *Cell* 1993. **75**: 263–274.

31 **Asadullah, K., Sterry, W., Stephanek, K., Jasulaitis, D., Leupold, M., Audring, H., Volk, H. D. and Docke, W. D.,** IL-10 is a key cytokine in psoriasis. Proof of principle by IL-10 therapy: a new therapeutic approach. *J. Clin. Invest.* 1998. **101**: 783–794.

32 **Lohning, M., Richter, A. and Radbruch, A.,** Cytokine memory of T helper lymphocytes. *Adv. Immunol.* 2002. **80**: 115–181.

33 **Wilson, C. B., Makar, K. W., Shnyreva, M. and Fitzpatrick, D. R.,** DNA methylation and the expanding epigenetics of T cell lineage commitment. *Semin. Immunol.* 2005. **17**: 105–119.

34 **Taga, K. and Tosato, G.,** IL-10 inhibits human T cell proliferation and IL-2 production. *J. Immunol.* 1992. **148**: 1143–1148.

35 **Oppmann, B., Lesley, R., Blom, B., Timans, J. C., Xu, Y., Hunte, B., Vega, F. *et al.*,** Novel p19 protein engages IL-12p40 to form a cytokine, IL-23, with

© 2009 WILEY-VCH Verlag GmbH & Co. KGaA, Weinheim

biological activities similar as well as distinct from IL-12. *Immunity* 2000. **13**: 715–725.

36 **Yen, D., Cheung, J., Scheerens, H., Poulet, F., McClanahan, T., McKenzie, B., Kleinschek, M. A. *et al.*,** IL-23 is essential for T cell-mediated colitis and promotes inflammation via IL-17 and IL-6. *J. Clin. Invest.* 2006. **116**: 1310–1316.

37 **Fuss, I. J., Boirivant, M., Lacy, B. and Strober, W.,** The interrelated roles of TGF-beta and IL-10 in the regulation of experimental colitis. *J. Immunol.* 2002. **168**: 900–908.

38 **Ruiz, P. A., Shkoda, A., Kim, S. C., Sartor, R. B. and Haller, D.,** IL-10 gene-deficient mice lack TGF-beta/Smad signaling and fail to inhibit proinflammatory gene expression in intestinal epithelial cells after the colonization with colitogenic *Enterococcus faecalis*. *J. Immunol.* 2005. **174**: 2990–2999.

39 **Li, M. O., Wan, Y. Y., Sanjabi, S., Robertson, A. K. and Flavell, R. A.,** Transforming growth factor-beta regulation of immune responses. *Annu. Rev. Immunol.* 2006. **24**: 99–146.

40 **Friedrich, M., Docke, W. D., Klein, A., Philipp, S., Volk, H. D., Sterry, W. and Asadullah, K.,** Immunomodulation by interleukin-10 therapy decreases the incidence of relapse and prolongs the relapse-free interval in Psoriasis. *J. Invest. Dermatol.* 2002. **118**: 672–677.

Abbreviation: **HPRT:** hypoxanthine phosphoribosyltransferase

Full correspondence: Dr. Gerald Grütz, Charité – Universitätsmedizin Berlin CC12, Institute of Medical Immunology, CCM, Charitéplatz 1, 10117 Berlin, Germany
Fax: +49-30-450-524932
e-mail: gerald.gruetz@charite.de

Received: 31/7/2008
Revised: 2/12/2008
Accepted: 19/1/2009

© 2009 WILEY-VCH Verlag GmbH & Co. KGaA, Weinheim

ORIGINAL ARTICLE

The Role of Mitogen-Activated Protein Kinase-Activated Protein Kinase 2 in the p38/TNF-α Pathway of Systemic and Cutaneous Inflammation

Arndt J. Schottelius[1], Ulrich Zügel[2], Wolf-Dietrich Döcke[3], Thomas M. Zollner[3], Lars Röse[3], Anne Mengel[4], Bernd Buchmann[4], Andreas Becker[5], Gerald Grütz[6], Sandra Naundorf[6], Anke Friedrich[6], Matthias Gaestel[7] and Khusru Asadullah[3]

Mitogen-activated protein kinase-activated protein kinase 2 (MK2) is a downstream molecule of p38, involved in the production of TNF-α, a key cytokine, and an established drug target for many inflammatory diseases. We investigated the role of MK2 in skin inflammation to determine its drug target potential. MK2 deficiency significantly decreased plasma TNF-α levels after systemic endotoxin application. Deficient mice showed decreased skin edema formation in chronic 2-*O*-tetradecanoylphorbol-13-acetate (TPA)-induced irritative dermatitis and in subacute 2,4-dinitrofluorobenzene (DNFB)-induced contact hypersensitivity. Surprisingly, MK2 deficiency did not inhibit edema formation in subacute 2,4-dinitrochlorobenzene (DNCB)-induced contact allergy and even increased TNF-α and IL-1β levels as well as granulocyte infiltration in diseased ears. Ear inflammation in this model, however, was inhibited by TNF-α neutralization as it was in the subacute DNFB model. MK2 deficiency also did not show anti-inflammatory effects in acute DNFB-induced contact hypersensitivity, whereas the p38 inhibitor, SB203580, ameliorated skin inflammation supporting a pathophysiological role of p38. When evaluating possible mechanisms, we found that TNF-α production in MK2-deficient spleen cells was strongly diminished after TLR stimulation but less affected after T-cell receptor stimulation. Our data suggest that MK2, in contrast to its downstream effector molecule, TNF-α, has a rather elusive role in T-cell-dependent cutaneous inflammation.

Journal of Investigative Dermatology (2010) **130,** 481–491; doi:10.1038/jid.2009.218; published online 6 August 2009

INTRODUCTION

Mitogen-activated protein kinase (MAPK)-activated protein kinase 2 (MK2) is one of several kinases that are regulated exclusively through direct phosphorylation by p38 MAP kinase in response to stress stimuli (Gaestel, 2006). The role of the stress-activated p38 MAPK protein kinase cascade in inflammation was defined several years ago by the anti-inflammatory effect of the p38 inhibitor, SB203580, and related compounds (Lee *et al.*, 1994; Jackson *et al.*, 1998). Accordingly, it was expected that several components of this kinase cascade may have been essential for early signaling in the inflammatory response and therefore yielded targets for anti-inflammatory therapy. Targeted disruption of p38 in mice results in embryonic lethality and impaired interleukin (IL)-1 signaling (Allen *et al.*, 2000). Deletion of one of the two known specific upstream activators of p38, the dual-specific MAPK kinase 3 (MKK3), leads to a reduction in IL-12 production (Lu *et al.*, 1999) and impaired tumor necrosis factor (TNF)-alpha-induced cytokine expression (Wysk *et al.*, 1999), and heterozygosity for p38α reduces ear swelling and cell infiltration in acute DNFB-induced contact allergy (Takanami-Ohnishi *et al.*, 2002).

Mice deficient in MK2 showed a reduction in bacterial lipopolysaccharide (LPS)-induced biosynthesis of TNF-α, interferon (IFN)-γ, IL-1β, IL-6, and nitric oxide, suggesting a critical role of MK2 in inflammatory cytokine production and inflammation (Kotlyarov *et al.*, 1999). It was later shown that MK2 regulates biosynthesis of IL-6 at the levels of mRNA stability and of TNF-α mainly through an AU-rich element-dependent translational control (Neininger *et al.*, 2002). The

[1]*MorphoSys AG, Martinsried, Germany;* [2]*Common Mechanism Research Early Projects, Global Drug Discovery, Bayer Schering Pharma AG, Berlin, Germany;* [3]*Target Discovery, Global Drug Discovery, Bayer Schering Pharma AG, Berlin, Germany;* [4]*Medicinal Chemistry, Global Drug Discovery, Bayer Schering Pharma AG, Berlin, Germany;* [5]*Protein Supply, Global Drug Discovery, Bayer Schering Pharma AG, Berlin, Germany;* [6]*Institute of Medical Immunology, Charité University Medicine, Berlin, Germany and* [7]*Center for Biochemistry/Institute of Biochemistry, Medical School of Hannover, Hannover, Germany*

Correspondence: Dr Arndt J. Schottelius, MorphoSys AG, D-82152 Planegg/Martinsried, Germany. E-mail: arndt.schottelius@morphosys.com

Abbreviations: DNCB, 2,4-dinitrochlorobenzene; DNFB, 2,4-dinitrofluorobenzene; IFN, interferon; IL, interleukin; LPS, lipopolysaccharide; MAPK, mitogen-activated protein kinase; MAPKAP, mitogen-activated protein kinase-activated protein; MK2, mitogen-activated protein kinase-activated protein kinase 2; TCR, T-cell receptor; TLR, toll-like receptor; TNF, tumor necrosis factor; TPA, 12-O-tetradecanoylphorbol-13-acetate

Received 8 August 2008; revised 29 May 2009; accepted 14 June 2009; published online 6 August 2009

© 2010 The Society for Investigative Dermatology

crucial role for MK2 in regulating TNF-α and IL-6 production was also shown in a mouse arthritis model. MK2-deficient mice had significantly lower LPS-induced TNF-α and IL-6 serum levels when compared with wild-type controls and were resistant to induction of collagen-induced arthritis (Hegen *et al.*, 2006). Moreover, deficiency of MK2 has been shown to markedly reduce infarct size following cerebral ischemic injury in mice. This protective effect was attributed to significantly lower expression of IL-1β, but not TNF-α mRNA (Wang *et al.*, 2002).

A series of pyridinyl imidazole compounds, exemplified by SB203580, have been developed as specific p38 inhibitors (Badger *et al.*, 1996). *In vivo* studies using some of these compounds have suggested that they might be useful in the treatment of several inflammatory conditions including immunologically driven and irritant-associated airway inflammation, rheumatoid arthritis, and psoriasis (Badger *et al.*, 1996; Jackson *et al.*, 1998). However, the preclinical efficacy of SB203580 has been associated with potential adverse events (Rogers and Giembycz, 1998; Dambach, 2005), and targeting p38 directly might thus have liabilities for drug development. Although p38-deficient mice are lethal, MK2 knockout mice are viable and show a normal phenotype (Allen *et al.*, 2000).

Taken together, targeting MK2 as a downstream kinase in the p38 pathway might have advantages over targeting p38 directly. Moreover, in contrast for example to TNF-α, MK2 as a kinase is considered as a molecular target druggable by small molecules (Gaestel *et al.*, 2007), an attractive characteristic that is also reflected by the fact that a number of pharmaceutical companies are pursuing drug discovery and development programs with MK2 (Anderson *et al.*, 2007; Gaestel *et al.*, 2007).

The aim of this study was (i) to determine the biological role of MK2 in skin inflammation models mainly by comprehensively comparing wild-type *versus* knockout mice responses in several models of cutaneous and systemic inflammation and (ii) to determine whether MK2 represents a promising drug target for the treatment of inflammatory skin diseases.

RESULTS

MK2 is involved in acute, systemic inflammation after endotoxin challenge in mice

As TNF-α is a key mediator of inflammation and a well-established drug target in skin inflammation (Schottelius *et al.*, 2004), we wanted to test the effect of MK2 deficiency on plasma levels of TNF-α in the model of LPS-induced systemic inflammation. As expected, homozygous MK2 deficiency resulted in significantly reduced TNF-α serum levels following a systemic LPS challenge in comparison with wild-type mice ($P<0.05$) (Figure 1). Partial deficiency of MK2 (MK2 heterozygous mice) also strongly reduced TNF-α serum levels, but the reduction did not reach statistical significance. These data confirm a report published earlier (Kotlyarov *et al.*, 1999) and show that the MK2-deficient mice we used for our studies displayed a similar phenotype as described.

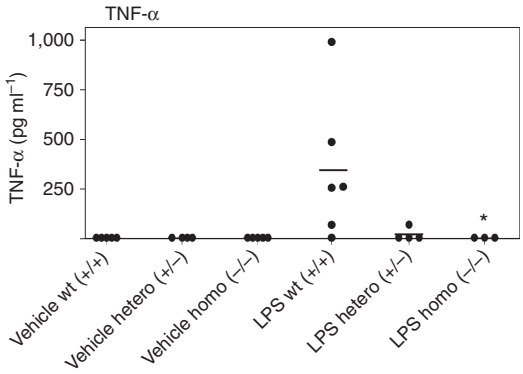

Figure 1. MK2 deficiency results in suppression of TNF-α production after systemic LPS exposure. Wild-type, MK2-heterozygous, and MK2-deficient mice were left untreated (NaCl control) or intraperitoneally challenged with LPS from *E. coli* (5 mg kg^{-1}). TNF-α serum levels as determined by Luminex measurement were strongly and significantly elevated at 1.5 hours after LPS challenge in wild-type mice ($n=6$), but were completely suppressed in mice heterozygous for MK2 ($n=4$) and in MK2-deficient mice ($n=3$; $^*P<0.05$, Mann–Whitney *U*-test).

To investigate the pathophysiological role of MK2 in skin disease, we tested MK2-deficient and wild-type mice in models of skin inflammation, which display characteristics of chronic, subacute, and acute skin inflammation.

Impact of MK2 deficiency on the chronic TPA-induced skin inflammation model in mice

MK2 knockout mice and wild-type controls were subjected to chronic 12-*O*-tetradecanoylphorbol-13-acetate (TPA)-induced irritative skin inflammation. Inflammatory edema formation after repeated TPA exposure was significantly decreased in MK2-deficient mice on days 5 ($P<0.001$) and 10 ($P<0.05$) (Figure 2a). Moreover, a significant reduction of neutrophil infiltration, as assessed by neutrophil elastase activity in skin homogenates, could be observed in MK2 knockout *versus* wild-type mice ($P<0.05$) (Figure 2c). Overall granulocyte infiltration, as assessed by peroxidase activity, however, was not different in MK2 knockout mice *versus* wild-type controls (Figure 2b).

Impact of MK2 deficiency on subacute DNFB- and DNCB-induced contact allergy models in mice

On repeated challenges with contact allergy-inducing haptens, DNFB (dinitrofluorobenzene)- or DNCB (dinitrochlorobenzene)-sensitized mice develop a T-cell-dependent skin inflammation of a pronounced Th1 phenotype. Owing to the subacute regimen with repeated challenges, these models may be particularly relevant for inflammatory skin diseases, such as psoriasis (Zollner *et al.*, 2004) in which TNF-α protein expression in lesional skin is suggested to be post-transcriptionally regulated by activated MK2 (Johansen *et al.*, 2006).

First, we tested MK2 knockout mice in a subacute model of DNFB-induced contact allergy. A significant reduction of ear edema formation was observed for MK2-deficient mice compared with the respective wild-type controls with the strongest reduction seen on day 8 (day 7 $P<0.05$; day 8

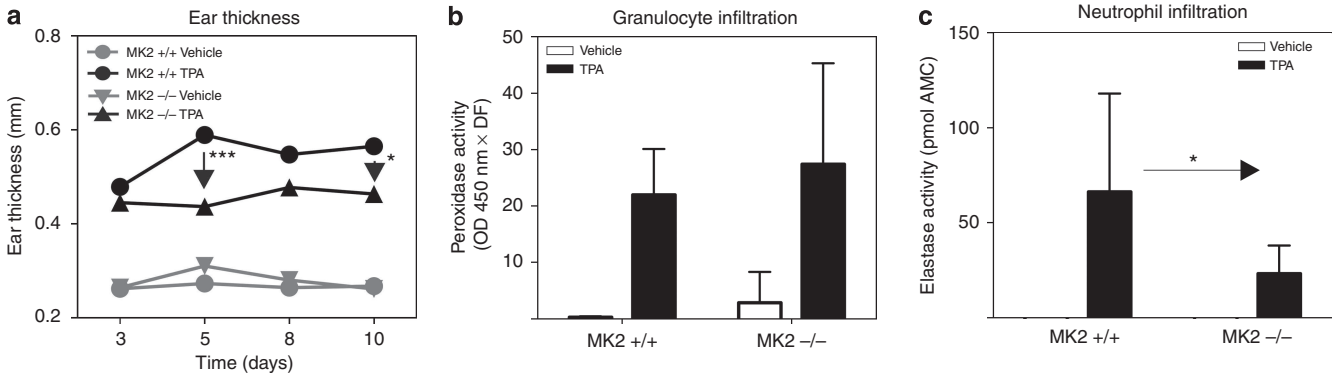

Figure 2. Skin inflammation is reduced in MK2-deficient mice in the chronic TPA-induced irritative dermatitis model. MK2-deficient and wild-type mice ($n=10$ per group) were subjected to TPA-induced skin inflammation. Mice ears were treated with TPA on days 1, 3, 5, 8, and 10 and killed on day 10 at 6 hours after the last TPA application. (**a**) The kinetics of ear thickness was assessed with a caliper. Skin inflammation was significantly decreased on days 5 and 10 in MK2-deficient mice compared with wild-type mice (***$P<0.001$ day 5, *$P<0.05$ day 10, Mann–Whitney *U*-test) after sensitization with TPA, whereas skin inflammation was not significantly decreased on days 3 and 8 in MK2-deficient mice. Moreover, although there was a significant reduction of neutrophil infiltration as assessed by elastase activity in ear homogenates on day 10 (*$P<0.05$) (**c**), peroxidase activity as a parameter for overall granulocyte infiltration was not significantly different in MK2 knockout mice compared with wild-type controls. (**b**) DF, dilution factor.

$P<0.001$) (Figure 3a). Interestingly, as in TPA-induced chronic skin inflammation, the reduction of edema formation was not accompanied by a consistent reduction in cutaneous granulocyte infiltration. Peroxidase activity in skin homogenates, as a parameter for overall granulocyte infiltration, was even significantly increased ($P<0.05$, Figure 3b), whereas neutrophil elastase activity, as a parameter for neutrophil infiltration, was significantly decreased ($P<0.05$, Figure 3c) in MK2-deficient animals compared with wild-type controls.

To elucidate whether inflammation in the subacute DNFB model is driven by TNF-α, we tested TNF-α expression at the mRNA and protein levels and the effect of neutralization with an anti-TNF-α antibody. The TNF-α mRNA levels were significantly upregulated following repeated challenges with DNFB in this model peaking at day 8 ($P<0.05$ day 8 *vs* day 5) (Figure 3d, left panel). IL-1β mRNA levels also increased steadily up to day 8, but the increase was not statistically significant (Figure 3d, right panel). Neutralization of TNF-α with two different anti-TNF-α antibodies significantly reduced ear edema in this model ($P<0.05$ for hamster anti-mouse TNF-α *versus* hamster control on day 8; $P<0.05$ for rabbit anti-mouse TNF-α *versus* rabbit control on days 7 and 8) (Figure 3e) and also strongly and significantly suppressed protein levels of TNF-α and IL-1β ($P<0.01$ *versus* control for both) (Figure 3f). These data suggest that the pathophysiology of the subacute DNFB contact allergy model is mainly driven by the inflammatory effects of TNF-α and that MK2-deficiency leads to a significant reduction in ear inflammation, potentially through TNF-α suppression in this model.

In contrast, the formation of ear edema 8 or 9 days post challenge was not reduced when MK2 knockout mice were tested in the subacute DNCB-induced contact allergy model (Figure 4a). Surprisingly, in this model, the infiltration of inflammatory cells was even strongly and significantly increased in MK2-deficient mice compared with wild-type controls ($P<0.001$ for cutaneous peroxidase and elastase activity) (Figure 4b and c). To further investigate whether the increase of cellular infiltration in MK2-deficient mice in DNCB-induced contact allergy was accompanied by changes in cutaneous cytokine production, we analyzed ear homogenates of DNCB-challenged mice for the presence of inflammatory cytokines. TNF-α and IL-1β levels were increased at 24 hours after the last DNCB challenge in both MK2 wild-type and deficient mice compared with unchallenged mice (Figure 4d). However, MK2 knockout mice produced significantly higher levels of TNF-α and IL-1β after repeated challenges with DNCB when compared with wild-type controls ($P<0.05$ for TNF-α, $P<0.001$ for IL1β). Increased infiltration of inflammatory cells in MK2 knockout mice in DNCB-induced contact allergy was thus accompanied by a higher production of TNF-α and IL-1β.

As MK2 deficiency caused different effects on skin inflammation in DNFB- *versus* DNCB-induced contact allergy, we further wanted to elucidate whether TNF-α also has a pathophysiological role in the subacute DNCB-induced contact allergy model, that is, whether TNF-α levels are incrementally increased and whether neutralization of TNF-α would reduce inflammation equally in this model. In line with the results from the subacute DNFB model, we observed increasing TNF-α and IL-1β mRNA expression in the subacute DNCB model ($P<0.05$ for TNF-α for days 7 and 9 *vs* day 6 and for IL-1β for day 9 *vs* day 6) (Figure 4e). Most importantly, neutralization of TNF-α with an anti-TNF-α antibody reduced ear thickness significantly and with comparable efficacy as in subacute DNFB-induced contact allergy (Figure 3e) in the subacute DNCB-induced contact allergy ($P<0.05$ for days 7, 8, and 9) (Figure 4f). Also, in the DNCB-induced contact allergy model, neutralization of TNF-α strongly and significantly suppressed protein levels of TNF-α and IL-1β ($P<0.01$ for TNF-α and $P<0.05$ for IL-1β) (Figure 4g).

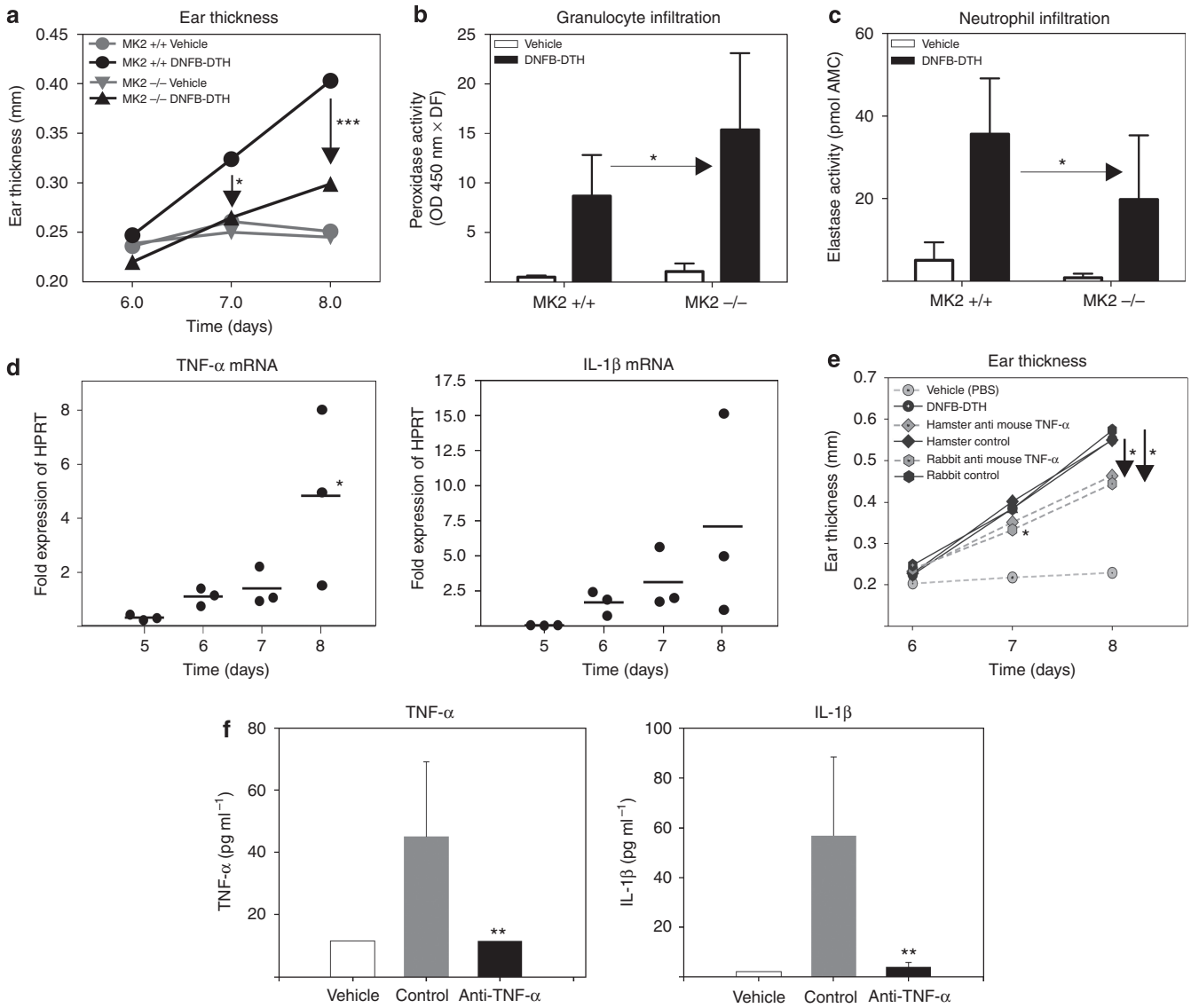

Figure 3. MK2-deficient mice show decreased skin inflammation in the subacute model of DNFB-induced contact allergy. MK2-deficient and wild-type mice ($n=10$ per group) were challenged on the ears with DNFB on days 5, 6, and 7 after sensitization. (**a**) Ear thickness was measured with a caliper on days 6, 7, and 8 after DNFB sensitization. MK2-deficient mice developed significantly less ear edema when compared with wild-type controls (*$P<0.05$ day 7; ***$P<0.001$ day 8, Mann–Whitney *U*-test). (**b**, **c**) Ears were homogenized on day 8 after sensitization and assayed for peroxidase activity as a parameter for granulocyte infiltration (**b**) and elastase activity for neutrophil infiltration (**c**). Both parameters were significantly increased after challenge with DNFB. Although granulocyte infiltration was significantly increased (*$P<0.05$), neutrophil infiltration was significantly decreased in MK2-deficient *versus* wild-type mice (*$P<0.05$, Mann–Whitney *U*-test). The subacute model of DNFB-induced contact allergy is mainly driven by TNF-α. (**d**) Wild-type mice were challenged with DNFB on days 5, 6, and 7 after DNFB sensitization. mRNA was extracted from ear homogenates of mice killed on days 5, 6, 7, and 8 after sensitization ($n=3$ for each time point). TNF-α and IL-1β mRNA levels steadily increased up to day 8 (*$P<0.05$ day 8 *vs* day 5 for TNF-α, Mann–Whitney *U*-test). (**e**, **f**) Treatment with either hamster or rabbit anti-mouse TNF-α antibodies before challenges (day 5) significantly reduced ear inflammation in subacute DNFB-induced contact allergy in C57Bl/6 wild-type mice ($n=7$ for anti-TNF-α antibodies; $n=10$ for control IgGs). (**e**) TNF neutralization significantly diminished ear thickness on day 7 (*$P<0.05$ for rabbit anti-mouse TNF-α *versus* rabbit control, Mann–Whitney *U*-test) and on day 8 after sensitization (*$P<0.05$ for hamster anti-mouse TNF-α *versus* hamster control and for rabbit anti-mouse TNF-α *versus* rabbit control, Mann–Whitney *U*-test). (**f**) Neutralization of TNF-α by hamster anti-mouse TNF-α significantly reduced protein levels of TNF-α and IL-1β (**$P<0.01$ *versus* hamster control IgG, Mann–Whitney *U*-test) in ear homogenates on day 8 after DNFB sensitization. DF, dilution factor.

Taken together, our data establish the central role of TNF-α in the pathogenesis of both the subacute DNFB- and DNCB-induced contact allergy models and further show that the differential functional effects of MK2-deficiency in these models cannot be explained by the lack of a role for TNF-α in inducing inflammation in one model *versus* the other.

Differing effect of MK2 deficiency and p38 inhibition on the acute DNFB-induced contact allergy model in mice

As MK2 knockout mice showed the most prominent and significantly reduced ear edema formation in the subacute DNFB contact allergy model, we wanted to investigate whether this anti-inflammatory effect of MK2-deficiency

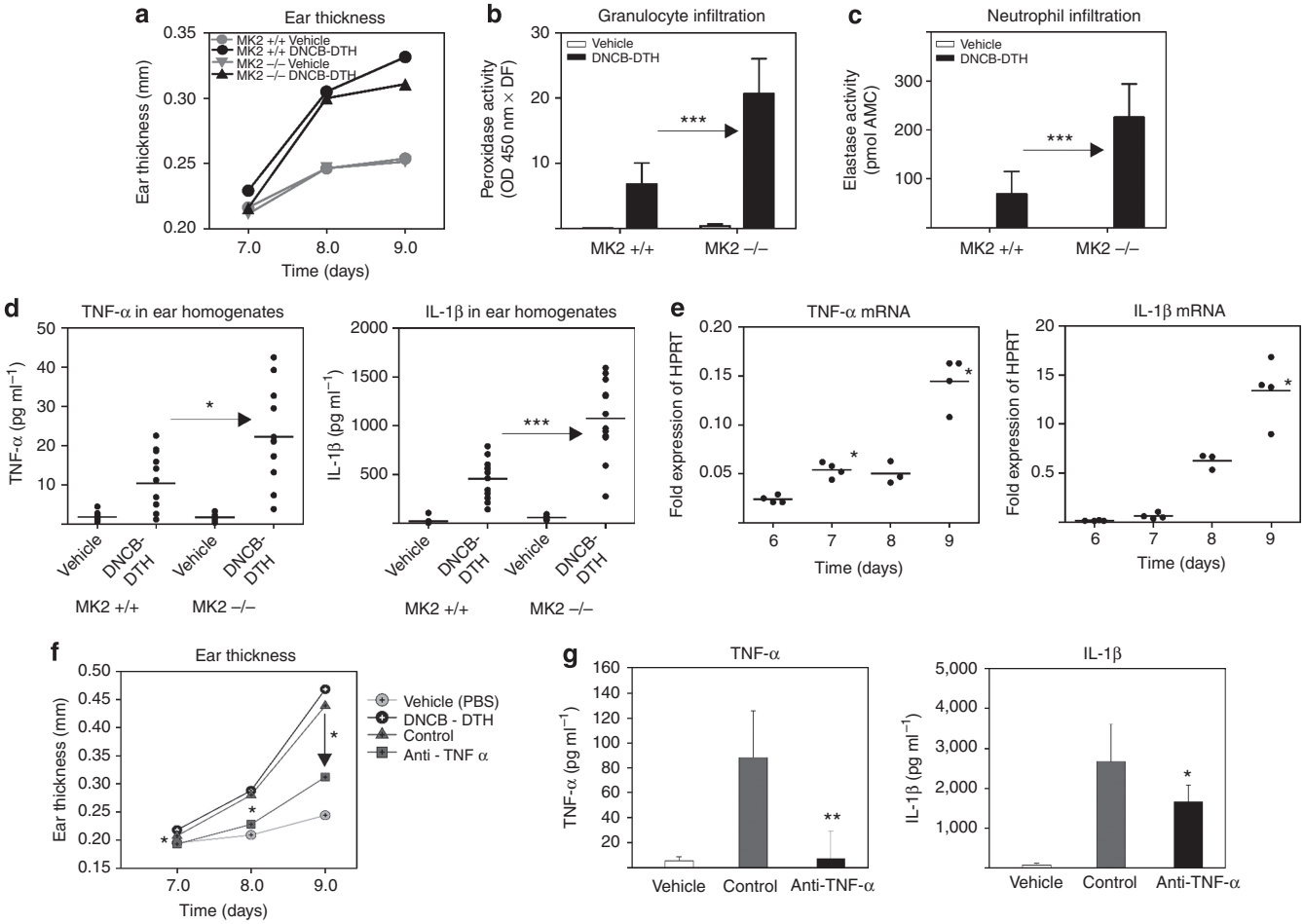

Figure 4. Skin inflammation is not reduced in MK2-deficient mice in the subacute DNCB-induced contact allergy model. MK2-deficient and wild-type mice ($n=10$ per group) were challenged with DNCB on days 6, 7, and 8 after sensitization. (**a**) Ear thickness was measured with a caliper on days 7, 8, and 9 after DNCB sensitization. No significant differences in ear thickness were detected between MK2-deficient and wild-type mice. (**b**, **c**) Ears were homogenized on day 9 after sensitization and assayed for peroxidase activity as a parameter for granulocyte infiltration (**b**) and elastase activity for neutrophil infiltration (**c**). Both parameters were significantly strongly increased in MK2-deficient compared with wild-type mice (***$P<0.001$ for granulocyte and neutrophil infiltration, Mann–Whitney *U*-test). (**d**) TNF-α and IL-1β protein levels in ear homogenates were determined on day 9 after sensitization ($n=6$–12 for each group). Both TNF-α and IL-1β were significantly increased in MK2-deficient compared with wild-type mice (*$P<0.05$ for TNF-α, ***$P<0.001$ for IL1β). The subacute model of DNCB-induced contact allergy is driven by TNF-α. (**e**) Wild-type mice were challenged with DNCB on days 6, 7, and 8 after DNCB sensitization. mRNA was extracted from ear homogenates of mice killed on days 6, 7, 8, and 9 after sensitization ($n=4$ for each time point). TNF-α and IL-1β mRNA levels steadily increased up to day 9 (*$P<0.05$ days 7 and 9 *vs* day 6 for TNF-α and day 9 *vs* day 6 for IL-1β, Mann–Whitney *U*-test). (**f**, **g**) C57Bl/6 wild-type mice ($n=10$ for rabbit anti-TNF-α and $n=8$ for rabbit IgG controls) were challenged with DNCB on days 6, 7, and 8 after sensitization. Treatment with rabbit anti-mouse TNF-α antibodies was performed before the challenges (day 6). (**f**) TNF-α neutralization significantly reduced ear inflammation as assessed by ear thickness (*$P<0.05$ *versus* rabbit IgG control on days 7, 8, and 9, Mann–Whitney *U*-test). (**g**) TNF-α neutralization significantly reduced protein levels of TNF-α and IL-1β (**$P<0.01$ and *$P<0.05$ *versus* rabbit IgG control, respectively, Mann–Whitney *U*-test) in ear homogenates on day 9 after sensitization. DF, dilution factor.

could also be observed in the acute model of DNFB-induced contact allergy using a single challenge of the same hapten in sensitized mice. In contrast to the effects seen in the subacute DNFB-induced contact allergy model after 3 DNFB challenges, no significant anti-inflammatory effect was seen in MK2 knockout mice in the acute DNFB contact allergy model compared with controls (Figure 5a–c). Comparable induction of ear edema formation (Figure 5a) and granulocyte (Figure 5b) as well as neutrophil infiltration (Figure 5c) was seen in MK2 knockout and wild-type mice in this model.

To further explore whether the p38 axis has any role in the pathophysiology of this acute contact allergy model, we tested the effects of the potent p38 inhibitor, SB203580, in MK2 wild-type mice compared with the potent glucocorticoid, dexamethasone, as a positive control. The pharmacological inhibition of p38 strongly and dose-dependently decreased skin inflammation and blocked ear edema formation and cell infiltration as potently as dexamethasone ($P<0.01$ for 0.3 and 1 mg kg^{-1} dexamethasone and for 3 and 10 mg kg SB203580; inhibition of granulocyte infiltration: $P<0.01$ for 1 mg kg^{-1} dexamethasone and for 3 and 10 mg kg^{-1} SB203580; inhibition of neutrophil infiltration: $P<0.05$ for 1 mg kg^{-1} dexamethasone and $P<0.01$ for 3 and 10 mg kg^{-1} SB 203580) (Figure 6a–c), showing that the p38

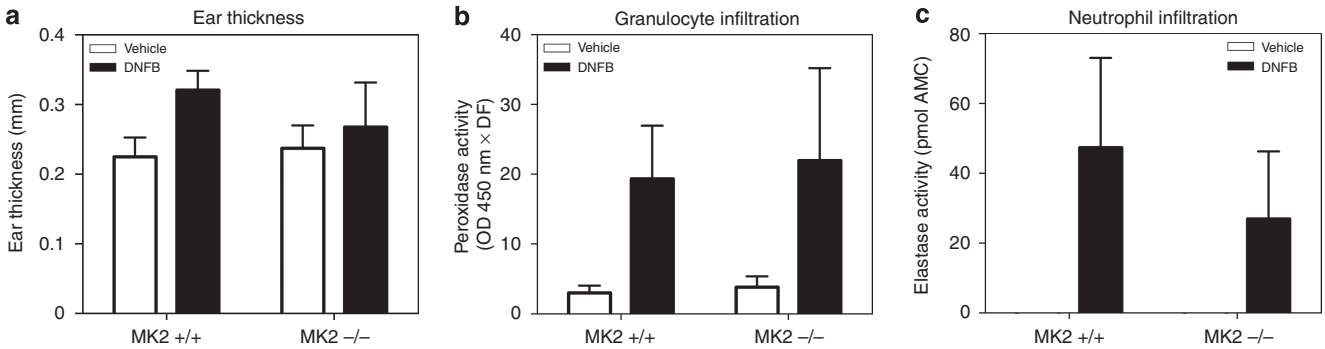

Figure 5. Skin inflammation is not reduced in MK2-deficient mice in the acute model of DNFB-induced contact allergy. MK2-deficient mice (vehicle $n=6$, DNFB $n=6$) and wild-type mice (vehicle $n=10$, DNFB $n=11$) were challenged on the ears with DNFB on day 5 after sensitization and killed on day 6. (**a**) As assessed by the ear thickness measurements with a caliper, MK2-deficient and wild-type mice developed similar degrees of ear edema. Moreover, cell infiltration was not different between MK2-deficient and wild-type mice as determined by peroxidase (**b**) and elastase (**c**) activities in ear homogenates as parameters for granulocyte and neutrophil infiltration, respectively. DF, dilution factor.

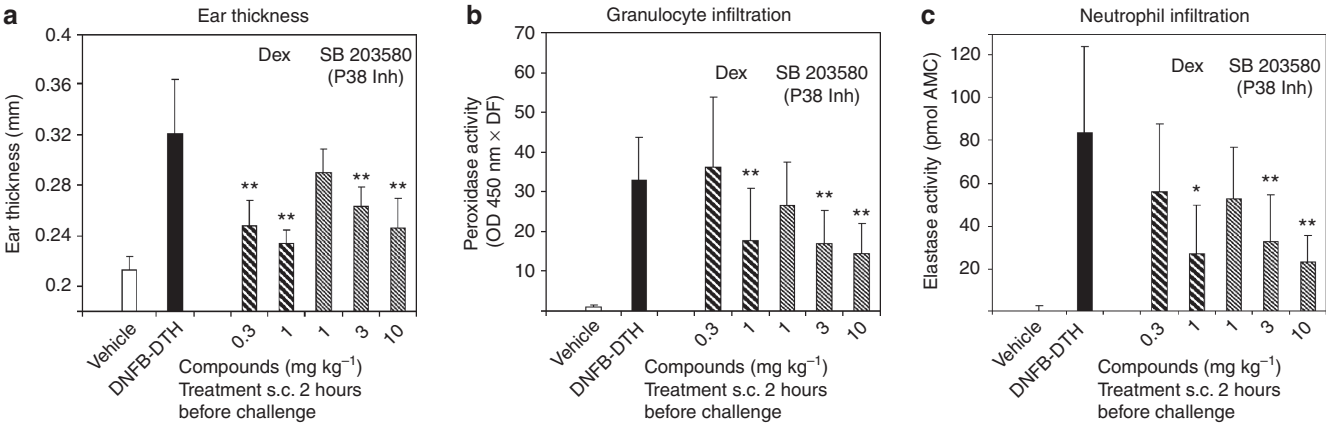

Figure 6. Pharmacological inhibition of p38 strongly and dose-dependently inhibits skin inflammation in the acute DNFB-induced contact allergy model in wild-type mice. DNFB-sensitized female NMRI mice ($n=10$ per group) were s.c. treated with different dosages of the p38 inhibitor, SB 203580, or vehicle at 2 hours before DNFB challenge on both ears at day 5 after sensitization and killed on day 6. Treatment with the glucocorticoid dexamethasone (Dex) served as positive control. Both compounds, SB 203580 and dexamethasone, significantly and dose-dependently inhibited (**a**) ear edema formation as determined by caliper measurement on day 6 after DNFB sensitization (**$P<0.01$ for 0.3 & 1 mg kg^{-1} dexamethasone and for 3 and 10 mg kg^{-1} SB203580, Mann–Whitney *U*-test) as well as (**b**) granulocyte infiltration (peroxidase activity) (**$P<0.01$ for 1 mg kg^{-1} dexamethasone and for 3 and 10 mg kg^{-1} SB203580, Mann–Whitney *U*-test) and (**c**) neutrophil infiltration (elastase activity in ear homogenates) (*$P<0.05$ for 1 mg kg^{-1} dexamethasone and **$P<0.01$ for 3 and 10 mg kg^{-1} SB 203580, Mann–Whitney *U*-test). DF, dilution factor.

axis needs to be intact for inflammation to develop in acute DNFB-induced contact allergy.

Collectively, these data show that specific MK2 deficiency does not exert a significant anti-inflammatory effect in this model of DNFB-induced acute skin inflammation, whereas the upstream regulatory molecule p38 is clearly involved, showing the relevance of the p38 pathway in this acute contact allergy model.

The TNF-α regulatory role of MK2 is consistent for TLR stimulation but may be restricted in T-cell stimulation

For a better mechanistic understanding of the observed differential *in vivo* effects, we further wanted to elucidate the role of MK2 signaling for the production of TNF-α in the most prominent pathways in relevant immune cells *ex vivo/in vitro*. Stimulation of different toll-like receptors (TLRs) in splenocytes with their respective ligands led to a strong induction of TNF-α, which was consistently and significantly reduced in the absence of MK2 ($P<0.01$ for LPS, $P<0.05$ for zymosan and imiquimod) (Figure 7a). The LPS *in vitro* data are consistent with our results observed in the model of LPS-induced systemic inflammation (Figure 1). Moreover, *in vitro* TNF-α production was comparably inhibited after the pharmacological blockade of p38 in wild-type splenocytes as in MK2-deficient splenocytes.

Remarkably, a quite similar inhibition of TNF-α production was seen in splenocytes stimulated with LPS alone or in combination with IFN-γ or anti-CD40 co-stimulation ($P<0.05$ for all stimuli) (Figure 7b, left panel) showing the robustness of the effects. However, in isolated splenic CD4$^+$

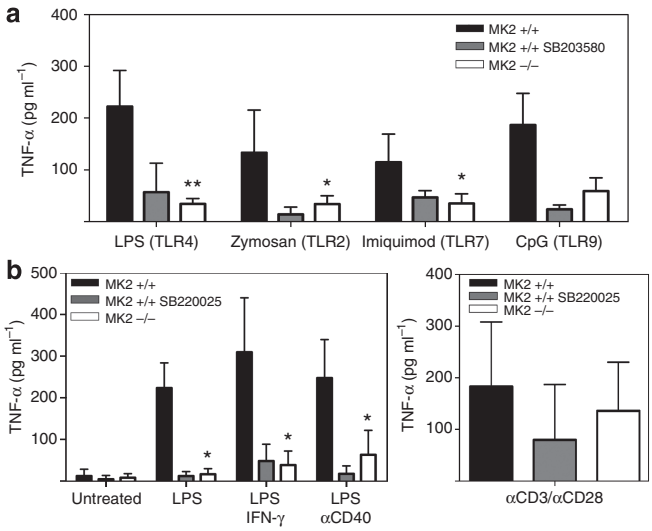

Figure 7. (a) TNF-α secretion after stimulation with different TLR stimuli is MK2-dependent. Spleen cells (5×10^6 ml^{-1}) from C57Bl/6 mice (wt; dark gray bars) or MK2-deficient mice (white bars) were stimulated for 4 hours with several TLR stimuli (LPS at 5 μg ml^{-1}, zymosan at 10 μg ml^{-1}, imiquimod at 1 μg ml^{-1}, or CpG ODNs at 10 μg ml^{-1}) as indicated. As a control, wild-type spleen cells were also stimulated in the presence of the p38 MAP kinase inhibitor, SB203580, at 10 μM (light gray bars). TNF-α content in supernatants was determined by ELISA. Absolute values are depicted from two (CpG) or 3–6 (all others) mice as means with error bars indicating SD. Significant differences between cell cultures from wild-type and MK2-deficient mice were determined by the Mann–Whitney *U*-test (*$P<0.05$, **$P<0.01$). (**b**) MK2 deficiency significantly diminishes TNF-α secretion after LPS stimulation with and without co-stimuli, but not after TCR stimulation. Splenocytes from C57Bl/6 (dark gray bars) and MK2-deficient mice (white bars) were left untreated or activated with LPS alone or in combination with co-stimulation (IFN-γ or anti-CD40) for 4 hours (left panel). As a control, wild-type spleen cells were also stimulated in the presence of the p38 MAP kinase inhibitor, SB220025, at 10 μM (light gray bars). TNF-α levels in supernatants were analyzed by ELISA, and the results are shown as the means from four mice (±SD). CD4$^+$ T cells separated from the spleens of either C57Bl/6- (dark gray bars) or MK2-deficient mice (white bars) were activated with plate-bound anti-CD3 and anti-CD28 antibodies for 72 hours (right panel). As a control, wild-type CD4+ T cells were also stimulated in the presence of the p38 MAP kinase inhibitor, SB220025, at 10 μM (light gray bars). TNF-α levels in supernatants were analyzed by ELISA. Results are shown as the means from four mice (±SD). Significant differences between cell cultures from wild-type and MK2-deficient mice were determined by Mann–Whitney *U*-test (*$P<0.05$).

T cells stimulated with anti-CD3/anti-CD28 antibodies, MK2 deficiency did not significantly alter the production of TNF-α (Figure 7b, right panel).

In summary, these *in vitro* data show that the p38/MK2 axis has a pivotal role in TLR-stimulated production of TNF-α in splenocytes, whereas anti-CD3/anti-CD28-driven TNF-α production in splenic T cells appears to be less dependent on MK2 signaling.

DISCUSSION

The p38 MAP kinase pathway has been shown to be a central regulator of inflammation (Lee *et al.*, 1994). MK2 is exclusively regulated by p38 and controls key inflammatory cytokines such as TNF-α and IL-6 (Kotlyarov *et al.*, 1999; Neininger *et al.*, 2002) as well as chemokines and adhesion molecules (Gorska *et al.*, 2007). Both kinases have thus been identified as potentially promising drug targets and have become the focus of several drug discovery programs (Gaestel, 2006; Duraisamy *et al.*, 2008). Targeting MK2 as a downstream kinase in the p38 pathway might have advantages over targeting p38 directly, because pharmacological inhibition of p38 was implicated with potential adverse events (Dambach, 2005). The relevance of MK2 as a drug target was elucidated for certain inflammatory diseases such as rheumatoid arthritis in relevant animal models (Hegen *et al.*, 2006); however, its target relevance in inflammatory skin disease has remained elusive. Although a recent report shows a role of MK2 in the oxazolone-induced contact allergy model (Funding *et al.* 2009), here, we provide a comprehensive characterization of the pathophysiological role of MK2 in a broad panel of murine models of skin inflammation, contributing to its evaluation as a drug target in inflammatory skin disease.

Here, we show that MK2 deficiency exerts anti-inflammatory effects in chronic TPA-induced irritative skin inflammation and in the subacute model of DNFB-induced contact allergy leading to a significant reduction in the development of ear edema (Figures 2a and 3a). However, the reduction in edema formation was accompanied by an only partial reduction of inflammatory cell infiltration parameters in these models. Although neutrophil infiltration, assessed by elastase activity, was significantly reduced in MK2-deficient mice (Figures 2c and 3c), general granulocyte infiltration, as assessed by cutaneous peroxidase activity, was in tendency or significantly enhanced (Figures 2b and 3b, respectively). Moreover, we did not observe any inhibitory effect of MK2 deficiency on inflammation in the subacute DNCB contact allergy model. Here, a lack of significant inhibition of ear edema formation was accompanied by even significantly increased cell infiltration parameters (Figure 4a–c). It is noted that this increase in cutaneous cell infiltration in MK2 knockout mice was also accompanied by a significant increase in TNF-α and IL-1β production in the inflammatory skin lesions of MK2-deficient mice compared with wild-type controls (Figure 4d). This result was surprising, because experiments with MK2 knockout mice used in our studies were able to confirm that LPS-induced plasma levels of TNF-α were drastically reduced as reported earlier (Figure 1) (Kotlyarov *et al.*, 1999).

Remarkably, the differential effects of MK2 deficiency in the subacute DNFB- *versus* the subacute DNCB-induced contact allergy model cannot be explained by a different role for TNF-α in the pathogenesis of these models, because in both models cutaneous TNF-α expression significantly increased with inflammation (Figures 3d and 4e) and neutralization of TNF-α exerted a potent and comparable anti-inflammatory effect (Figures 3e and 4f). Although both DNFB and DNCB are considered Th1-inducing haptens, a variety of studies have shown a number of differences in the cellular and molecular mechanisms elicited by these compounds, all of which may have contributed to the

differential effects observed in contact allergy in mice in the absence of MK2, namely the different effects on CD86 and HLA-DR expression in dendritic cells (Manome *et al.*, 1999) indicating a more potent role of DNCB over DNFB in dendritic cells and the distinct ability of DNFB to induce IL-10-producing mast cells and NK cell-mediated memory responses (O'Leary *et al.*, 2006; Grimbaldeston *et al.*, 2007) where the p38/MK2 pathway may have a differential role *versus* contact allergy elicited by DNCB.

When tested in the acute model of DNFB-induced contact allergy, MK2 knockout mice did not develop significantly less skin inflammation than their wild-type controls (Figure 5a–c). In contrast, the pharmacological inhibition of p38 potently and dose-dependently abrogated both edema formation and infiltration of inflammatory cells in acute DNFB-induced contact allergy (Figure 6a–c). These results confirm the reported role of p38 MAP kinase in the pathophysiology of acute DNFB-induced contact hypersensitivity (Takanami-Ohnishi *et al.*, 2002). The lack of a significant anti-inflammatory effect by MK2 deficiency in acute DNFB-induced contact allergy thus cannot be attributed to a lesser pathophysiological role of the p38 pathway in this skin inflammation model. The p38 kinase has also been shown to be activated in lesional psoriatic skin (Johansen *et al.*, 2005), supporting its relevance in human inflammatory skin disease.

One possible explanation for the inconsistent impact of MK2 deficiency in T-cell-dependent contact allergy models might be provided by the results of our mechanistic studies in mouse splenocytes. We show that, as *in vivo*, MK2 has a pivotal role in TLR-triggered TNF-α production in splenocytes. In contrast, however, the CD3/CD28-mediated TNF-α production in splenic T cells appears to be less dependent on MK2 signaling.

The fact that TLR-dependent, but not TCR-dependent, TNF production is significantly decreased in MK2-deficient and SB22025-treated splenocytes is in agreement with the established role of the p38/MK2 module in signal transduction located directly downstream to the canonical TLR4/IRAK4/TAK1/MKK3/6 pathway (summarized in Gaestel, Kotlyarov, and Kracht, 2009). In contrast, stimulation of TNF-α production in response to TCR stimulation could proceed in a non-canonical manner through non-receptor protein tyrosine kinases, such as Lck (Salvador *et al.*, 2005), Itk, or Syk, in a more p38/MK2-independent manner. This non-canonical stimulation of TNF-α generation downstream of TCR stimulation could in turn explain that the pharmacological blockade of p38 by the compound SB220025 and MK2 deficiency shows much lesser effects on TNF production in splenocytes on anti-CD3/anti-CD28 stimulation.

One could further hypothesize that the autoimmune suppressor Gadd45a may have some function in the differentiated role of TCR-mediated TNF production in splenocytes. Gadd45a can inhibit p38 Tyr323 phosphorylation, which is specific for the non-canonical or alternative pathway of p38 activation in T cells (Salvador *et al.*, 2005).

Taken together, our results confirm the crucial function of MK2 in LPS-induced TNF-α production in systemic inflammation and further support the observation that this axis has distinct roles for different inflammatory pathways in different cell types and target organs.

Here, we show that MK2 deficiency exerts limited anti-inflammatory effects or can even enhance inflammation in specific, more chronic mouse models of skin inflammation in which TNF-α has a central role in the development of disease, and, in contrast to p38 inhibition, did not exert inhibitory effects in an acute T-cell-dependent DNFB-induced contact allergy model. These results may indicate that MK2 is bypassed in skin inflammation or that MK2 function is compensated for by a different kinase. One such kinase candidate may be MK3, another MAPKAP kinase downstream of p38, which has been described to be also involved in TNF-α production and which might compensate for the function of MK2 (Hegen *et al.*, 2006; Ronkina *et al.*, 2007).

Our results are in partial contrast to other reports that concluded a general potent anti-inflammatory effect of MK2 inhibition, based on MK2 deficiency in other cytokine-driven diseases such as LPS-induced systemic inflammation or mouse arthritis models (Kotlyarov *et al.*, 1999; Hegen *et al.*, 2006) and also on a recent report showing that MK2 deficiency diminishes inflammation in an oxazolone-induced acute allergic contact dermatitis model (Funding *et al.* 2009). Interestingly, MK2 deficiency has been shown to exacerbate TNF-dependent inflammatory bowel disease in the mouse (Kontoyiannis *et al.*, 2002). The observed differences may be based on the distinct role for the p38/MK2/TNF-α axis in the pathogenesis of these different inflammation models in different target organs.

From a methodological point of view, our data show that drawing general conclusions from a single skin inflammation model alone may not be reliable. The data we obtained in the subacute DNFB-induced contact allergy (and also the chronic TPA-induced irritative skin inflammation model), suggesting an impact of MK2 in skin inflammation, were neither confirmed in a different subacute contact allergy model nor in the acute DNFB model, when the hapten was applied in a more acute setting. Therefore, both the kinetics of the model (acute *versus* subacute) and the resulting dominating stimulatory pathways (for example, TCR stimulation *versus* cytokine stimulation) as well as the choice of hapten (DNFB *versus* DCNB) appear to have an impact on the biological role of MK2 in skin inflammation and its downstream effects on TNF-α. Investigating the effects of compounds or genetic alterations in several different contact allergy models comprehensively may thus be required before general conclusions can be drawn from a data set.

In conclusion, our studies confirm the role of MK2 in an acute TLR-driven systemic inflammation, whereas MK2 seems to have at least a less prominent and more complex role in skin inflammation. However, the entire role of MK2 in chronic relapsing T-cell-dependent skin diseases in man is still not fully understood and awaits further analysis. As expression analysis of MK2 in human lesional skin from patients with chronic plaque-type psoriasis revealed an activation of MK2 protein in inflamed psoriatic skin (Johansen

et al., 2006), the role of MK2, for example, in psoriasis, is still subject to further investigations.

As neutralization or inhibition of TNF-α has been validated as a potent therapy for rheumatoid arthritis, inflammatory bowel disease, and psoriasis in the clinic (Schottelius *et al.*, 2004), disruption or dampening of TNF-α production would be expected to yield good therapeutic effects. It would thus seem conceivable that MK2 is an attractive target for a pharmacological inhibition in treating a variety of inflammatory diseases. With the data available to date, including our findings reported here, this approach might yield more therapeutic promise in rheumatoid arthritis than in inflammatory skin diseases such as psoriasis or atopic dermatitis. Future studies with MK2-deficient mice in other animal models of disease may be able to further elucidate the role of MK2 for other inflammatory conditions such as Crohn's disease or ulcerative colitis.

MATERIALS AND METHODS

Mice

C57Bl/6 mice (purchased from Charles River, Sulzfeld, Germany), NMRI female mice (from ''Schoenwalde NMRI colonies'' exclusively bred for Bayer Schering Pharma AG at Charles River, Germany), and MK2 knockout mice (provided from Hannover Medical School, Hannover, Germany) in the age group of 8–12 weeks were housed in the animal facility at the Bayer Schering Pharma AG. All animal studies were approved by the competent authority for labor protection, occupational health, and technical safety for the state and city of Berlin, Germany, and were performed in accordance with the ethical guidelines of Bayer Schering Pharma AG.

Systemic endotoxin-induced inflammation in mice

C57Bl/6 wild-type, MK2-heterozygous, and MK2-deficient mice were treated by intraperitoneal injection with 5 mg kg^{-1} LPS (*E. coli* 0111:B4; Sigma L-4391, Steinheim, Germany) or NaCl control. At 1.5 hours after LPS challenge, the mice were killed, and the serum levels of TNF-α were determined by Luminex assay (Biorad, Munich, Germany).

Acute DNFB-induced contact allergy model

For sensitization, female WT and MK2-deficient mice were topically treated on day 0 and day 1 with 25 μl of 0.5% (w/v) 2,4-dinitrofluorobenzene (DNFB) (Sigma) in acetone/olive oil 4:1 (v/v) on the shaved abdomen. After 5 days, groups of 10 mice were challenged by the topical application of 20 μl of 0.3% (w/v) DNFB in acetone/olive oil 4:1 (v/v) on both sides of one ear. Small molecule inhibitors were applied subcutaneously (s.c.) in a volume of 0.1 ml per 20 g body weight in 0.9% NaCl solution containing 0.085% Myrj 53 (ICI, UK) and 5% ethanol 2 hours before DNFB challenge of the animals on day 5. On day 6 (24 hours after challenging animals), the thickness of the inflamed ears were determined, and myeloperoxidase (for granulocyte infiltration) and granulocyte elastase activities (a parameter for neutrophil infiltration) were measured in homogenates of inflamed ears as described earlier (Schottelius *et al.*, 2002; Zugel *et al.*, 2002).

Subacute DNFB- and DNCB-induced contact allergy models

To examine the role of MK2 in the subacute DNFB model, female and male WT and MK2 knockout mice were topically sensitized on day 0 and day 1 with 25 μl of a 0.5% (w/v) DNFB (Sigma) solution in acetone/olive oil 4:1 (w/v) on the shaved abdomen. On days 5, 6, and 7, contact allergy was induced by repeated challenge of the ears with topically applied DNFB (10 μl of a 0.15% [w/v] DNFB solution in acetone/olive oil 4:1 [w/v]). Ear thickness was monitored during the study as follows: day 0, day 5 (before challenge), day 6 (24 hours after first challenge), day 7 (24 hours after second challenge), and day 8 (24 hours after third challenge). In the subacute DNCB model, female and male WT and MK2 knockout mice were topically sensitized on day 0 with 25 μl of a 0.5% (w/v) 2,4-dinitrochlorobenzene (DNCB) (Merck, Darmstadt, Germany) in acetone/olive oil 4:1 (w/v) on the shaved abdomen. On days 6, 7, and 8, contact allergy was induced by repeated challenge of the ears with topically applied DNCB (10 μl of a 0.15% [w/v] DNCB solution in acetone/olive oil 4:1 [w/v]). Ear thickness was monitored during the study as follows: day 0, day 6 (before challenge), day 7 (24 hours after first challenge), day 8 (24 hours after second challenge), and day 9 (24 hours after third challenge). On day 8 (DNFB) or day 9 (DNCB), animals were killed, and peroxidase activity (for granulocyte infiltration) and elastase activity (a parameter for neutrophil infiltration) were measured in homogenates of inflamed ears as described earlier (Schottelius *et al.*, 2002; Zugel *et al.*, 2002). Genders have been combined in all figures as no significant gender differences have been observed for any of the skin inflammation models investigated.

TNF-α neutralization in subacute DNFB- and DNCB-induced contact allergy

Female C57Bl/6 mice were sensitized with 25 μl of 1% DNCB in acetone/olive oil (4:1) on the shaved flank skin on day 0. Challenges with 10 μl 1% DNCB in acetone/olive oil (1:9) on the dorsum of both ears were performed on days 6, 7, and 8. As treatment in both contact allergy models purified rabbit polyclonal anti-mouse-TNF-α antibodies (endogen) and in an additional treatment group in the subacute DNFB model purified hamster polyclonal anti-mouse TNF-α (Abcam Cambridge, UK) and as isotype controls purified rabbit and purified hamster IgG (AbD Serotec, Munich, Germany) was used.

The proteins were prepared for *in vivo* use with SLIDE-A-LYZER dialysis cassettes (Serotec). Treatment was applied 1 hour before the first challenge i.p. Ear thickness was determined over the time course with a custom-built automated caliper/micrometer (Bayer Schering Pharma AG, Berlin, Germany). At day 9, animals were killed and the ears were cut, weighed, and mechanically homogenized in 2 ml homogenization buffer (hexadecyltrimethylic ammonium bromide/morpholinopropan sulfonic acid (Sigma)), centrifuged at 25,000 *g* for 20 minutes at 12°C, and the supernatant was used for determination of immune mediators. Cutaneous granulocyte infiltration was assessed by myeloperoxidase activity assay in ear homogenates as described earlier (Schottelius *et al.*, 2002). Cytokine levels in ear homogenates were measured using MSD 96-Well MULTY-ARRAY and MULTI-SPOT technology (Meso Scale Discovery, Gaithersburg, MD) according to the manufacturer's instructions.

Chronic TPA-induced skin inflammation model

Ten microliters of the phorbol ester TPA (0.01 w/v) were applied to the inner and outer surfaces of each mouse ear using a micropipette. TPA was applied over a 10-day course on alternate days (days 1, 3, 5, 8, and 10). Ear thickness was assessed with a caliper starting

6 hours after TPA application (Alford *et al.*, 1992). Animals were killed on day 10 at 6 hours after last TPA application, and their ears were cut off, snap frozen, and later analyzed for peroxidase and elastase activity as described above.

Determination of elastase and peroxidase activities in ear homogenates

Peroxidase activity assay. Peroxidase activity as a measure of total granulocyte infiltration was measured as described earlier (Schottelius *et al.*, 2002). Briefly, tetramethylbenzidine (TMB) dihydrochloride was used as a sensitive chromogenic substrate for peroxidase. To convert TMB into TMB dihydrochloride, 34 μl of 3.7% hydrochloric acid (equimolar) was added to 5 mg of TMB. Then, 1 ml of DMSO was added. This stock solution was slowly added to sodium acetate–citric acid buffer (0.1 mol l^{-1}, pH 6.0) in a ratio of 1:100. Two hundred microliters of this TMB solution, 40 μl of the homogenized sample, and 25 μl of 1 mM H_2O_2 were added to a microtiter plate to start the reaction. The reaction was stopped after 30 minutes with 45 μl of 1 N H_2SO_4. Changes in OD were monitored at 450 nm at 25°C against the mixture of all solutions without the added sample homogenate. Absolute extinction numbers multiplied by respective dilution factors were used to express peroxidase activity.

Elastase activity assay. Elastase activity was measured by fluorescence of 7-amino-4-methyl-coumarin (AMC) that is released from the substrate MeO-Succ-Ala-Ala-Pro-Val-AMC (Bachem, Torrance, CA). Homogenized samples in HTAB were diluted 1/10 in cetrimide buffer (0.3% cetrimide, 0.1 M Tris, and 1 M NaCl, pH 8.5). The substrate MeO-Succ-Ala-Ala-Pro-Val-AMC (300 mM in DMSO) was diluted 1/100 in cetrimide buffer to a working concentration of 3 mM. In cetrimide buffer, diluted samples were pipetted in multiwell plates, and the reaction was started by addition of the AMC substrate at 37 °C. The reaction was stopped after 1 hour with ice-cold 100 mM Na_2CO_3, and samples were measured in a Spectra Max Gemine (Molecular Devices, Menlo Park, CA) at 380 nm and compared against a standard curve with the AMC standard 7-amino-4-methylcoumarin (5 mM in ethanol).

Cytokine analyses in serum from LPS-triggered systemic inflammation model and in ear homogenates from skin inflammation models

Inflamed ears from mouse skin inflammation models were mechanically homogenized in 2 ml homogenization buffer (hexadecyltrimethylic ammonium bromide/morpholinopropan sulfonic acid, Sigma, Deisenhofen, Germany), centrifuged at 25,000 *g* for 20 minutes at 12 °C, and supernatants were used for determination of immune mediators. Cytokine levels in ear homogenates were determined using a multiplex chemiluminescence method and MesoScale SI 6000 equipment (MesoScale Discovery, Gaithersburg, MD).

Gene expression analyses in mouse skin

For purification of RNA from mouse skin, ears were homogenized in 800 μl lysis buffer and digested with 2 mg ml^{-1} Proteinase K (BD Biosciences, Erembodegem, Belgium) for 1 hour. Purified RNA from mouse skin was qualified with the Agilent Bioanalyzer 2100 system with RNA 6000 Nano Assay Kit (Agilent Technologies, Santa Clara, CA). cDNA was synthesized using Reverse Transcription Reagents and GeneAmp PCR System 9700 (Applied Biosystems, Foster City, CA). RT-PCR was performed in 12.5 μl using a universal PCR Master Mix without UNG (Eurogentec, Cologne, Germany) on a 7900 HT Sequence Detection System (Applied Biosystems) under thermal conditions: 40 cycles at 95°C for 10 minutes, 95°C for 15 seconds, and 60°C for 1 minute. Expression of target genes was quantified as the fold expression of the housekeeping gene, hypoxanthine phosphoribosyltransferase (HPRT). The expression of the following mouse genes was determined in triplicated analyses using Assays on demand from Applied Biosystems: IL-1β (Mm 00434228_m1) and TNF-α (Mm 00443258_m1).

Cell culture

Spleen cells from C57Bl/6 wild-type or Mapkapk2^{tm1Mgl} (C57Bl/6) mice were brought into suspension after squeezing through a cell strainer in RPMI-1640 and supplemented with 10% FCS, 1 mM L-glutamine, 100 U ml^{-1} penicillin, and 100 μg ml^{-1} streptomycin at a density of 5×10^6 cells per ml. For TLR stimulation, cells were then directly stimulated for 4 hours with either 5 μg ml^{-1} LPS (TLR4 grade, Alexis, Lörrach, Germany) alone or in combination with co-stimulation: either 10 ng ml^{-1} of IFN-γ (R&D Systems, Wiesbaden, Germany) or activating anti-CD40 antibody (clone 3/23, 1 μg ml^{-1}; BD Bioscience, Heidelberg, Germany). Furthermore, splenocytes were stimulated for 4 hours with other TLR stimuli such as 10 μg ml^{-1} zymosan (Sigma, Steinheim, Germany), 1 μg ml^{-1} imiquimod (Sequoia Research Product, Reading, UK), or 10 μg ml^{-1} CpG ODN (R&D Systems, Germany). As a control, wild-type spleen cells were treated additionally with p38 MAP kinase inhibitors SB203580 (10 μM; Merck Biosciences, Darmstadt, Germany) or SB220025 (10 μM; Axxora, Lörrach, Germany), respectively.

For TCR stimulation, CD4+ T cells were positively separated from splenocytes by using anti-CD4 (L3T4)-coated magnetic MACS beads (Miltenyi Biotech, Bergisch Gladbach, Germany) following the manufacturer's protocol. T cells were cultured at a density of 2×10^6 cells per ml in RPMI-1640 medium supplemented with FCS (10% v/v), L-glutamine (2 mM), and penicillin/streptomycin (each at 10,000 U ml^{-1}) (all Biochrom KG, Berlin, Germany) and stimulated with plate-bound anti-CD3 (clone 17A2, 10 μg ml^{-1}; BD Bioscience) and anti-CD28 (clone 37.51, 10 μg ml^{-1}; BD Bioscience). As a control, wild-type spleen cells were treated additionally with SB203580 (Merck Biosciences) at a concentration of 10 μM.

Supernatants were collected after stimulation of the respective cells and cytokine concentrations were determined with TNF-α ELISA (OptEIA set; BD Biosciences) according to the manufacturer's description.

Statistical methods

Statistical methods used for murine skin inflammation models (comparison of groups in kinetic measurements of skin thickness) were the Kruskal–Wallis and Mann–Whitney *U*-tests by SPSS software (SPSS). Statistics for end point parameters were collected by Fieller's test using a program from Bayer Schering Pharma AG based on the SAS System for Windows 6.12 (SAS Institute) (Schottelius *et al.*, 2002). Statistical methods used for *ex vivo* and *in vitro* investigations were the Mann–Whitney *U*-test and Wilcoxon's matched-pairs signed-ranks test, respectively, using SPSS software. If not otherwise indicated, mean values ± SD are shown. Statistical significances at $P<0.05$, <0.01, and <0.001 are indicated by one, two, and three asterisks, respectively.

CONFLICT OF INTEREST

The authors UZ, WDD, TMZ, LR, AM, BB, AB, and KA are employees and shareholders of Bayer Schering AG. Bayer Schering Pharma AG is not actively pursuing MK2.

ACKNOWLEDGMENTS

We thank Detlef Opitz, Christian Okon, Michaela Nieter, and Antje HaeuBler-Quade for excellent technical assistance. All data for this publication have been generated at Bayer Schering Pharma AG.

REFERENCES

Alford JG, Stanley PL, Todderud G, Tramposch KM (1992) Temporal infiltration of leukocyte subsets into mouse skin inflamed with phorbol ester. *Agents Actions* 37:260–7

Allen M, Svensson L, Roach M, Hambor J, McNeish J, Gabel CA (2000) Deficiency of the stress kinase p38alpha results in embryonic lethality: characterization of the kinase dependence of stress responses of enzyme-deficient embryonic stem cells. *J Exp Med* 191:859–70

Anderson DR, Meyers MJ, Vernier WF, Mahoney MW, Kurumbail RG, Caspers N *et al.* (2007) Pyrrolopyridine inhibitors of mitogen-activated protein kinase-activated protein kinase 2 (MK-2). *J Med Chem* 50:2647–54

Badger AM, Bradbeer JN, Votta B, Lee JC, Adams JL, Griswold DE (1996) Pharmacological profile of SB 203580, a selective inhibitor of cytokine suppressive binding protein/p38 kinase, in animal models of arthritis, bone resorption, endotoxin shock and immune function. *J Pharmacol Exp Ther* 279:1453–61

Dambach DM (2005) Potential adverse effects associated with inhibition of p38alpha/beta MAP kinases. *Curr Top Med Chem* 5:929–39

Duraisamy S, Bajpai M, Bughani U, Dastidar SG, Ray A, Chopra P (2008) MK2: a novel molecular target for anti-inflammatory therapy. *Expert Opin Ther Targets* 12:921–36

Funding AT, Johansen C, Gaestel M, Bibby BM, Lilleholt LL, Kragballe K *et al.* (2009) Reduced oxazolone-induced skin inflammation in MAPKAP kinase 2 knockout mice. *J Invest Dermatol* 129:891–8

Gaestel M (2006) MAPKAP kinases – MKs – two's company, three's a crowd. *Nat Rev Mol Cell Biol* 7:120–30

Gaestel M, Mengel A, Bothe U, Asadullah K (2007) Protein kinases as small molecule inhibitor targets in inflammation. *Curr Med Chem* 14:2214–34

Gaestel M, Kotlyarov A, Kracht M (2009) Targeting innate immunity protein kinase signaling in inflammtion. *Nat Rev Drug Discov* 8:480–99

Gorska MM, Liang Q, Stafford SJ, Goplen N, Dharajiya N, Guo L *et al.* (2007) MK2 controls the level of negative feedback in the NF-kappaB pathway and is essential for vascular permeability and airway inflammation. *J Exp Med* 204:1637–52

Grimbaldeston MA, Nakae S, Kalesnikoff J, Tsai M, Galli SJ (2007) Mast cell-derived interleukin 10 limits skin pathology in contact dermatitis and chronic irradiation with ultraviolet B. *Natu Immunol* 8:1095–104

Hegen M, Gaestel M, Nickerson-Nutter CL, Lin LL, Telliez JB (2006) MAPKAP kinase 2-deficient mice are resistant to collagen-induced arthritis. *J Immunol* 177:1913–7

Jackson JR, Bolognese B, Hillegass L, Kassis S, Adams J, Griswold DE *et al.* (1998) Pharmacological effects of SB 220025, a selective inhibitor of P38 mitogen-activated protein kinase, in angiogenesis and chronic inflammatory disease models. *J Pharmacol Exp Ther* 284:687–92

Johansen C, Funding AT, Otkjaer K, Kragballe K, Jensen UB, Madsen M *et al.* (2006) Protein expression of TNF-alpha in psoriatic skin is regulated at a posttranscriptional level by MAPK-activated protein kinase 2. *J Immunol* 176:1431–8

Johansen C, Kragballe K, Westergaard M, Henningsen J, Kristiansen K, Iversen L (2005) The mitogen-activated protein kinases p38 and ERK1/2 are increased in lesional psoriatic skin. *Br J Dermatol* 152:37–42

Kontoyiannis D, Boulougouris G, Manoloukos M, Armaka M, Apostoloki M, Pizarro T *et al.* (2002) Genetic dissection of the cellular pathways and signaling mechanisms in modeled tumor necrosis factor-induced Crohn's like inflammatory bowel disease. *J Exp Med* 196:1563–74

Kotlyarov A, Neininger A, Schubert C, Eckert R, Birchmeier C, Volk HD *et al.* (1999) MAPKAP kinase 2 is essential for LPS-induced TNF-alpha biosynthesis. *Nat Cell Biol* 1:94–7

Lee JC, Laydon JT, McDonnell PC, Gallagher TF, Kumar S, Green D *et al.* (1994) A protein kinase involved in the regulation of inflammatory cytokine biosynthesis. *Nature* 372:739–46

Lu HT, Yang DD, Wysk M, Gatti E, Mellman I, Davis RJ *et al.* (1999) Defective IL-12 production in mitogen-activated protein (MAP) kinase kinase 3 (Mkk3)-deficient mice. *EMBO J* 18:1845–57

Manome H, Aiba S, Tagami H (1999) Simple chemicals can induce maturation and apoptosis of dendritic cells. *Immunology* 98:481–90

Neininger A, Kontoyiannis D, Kotlyarov A, Winzen R, Eckert R, Volk HD *et al.* (2002) MK2 targets AU-rich elements and regulates biosynthesis of tumor necrosis factor and interleukin-6 independently at different post-transcriptional levels. *J Biol Chem* 277:3065–8

O'Leary JG, Goodarzi M, Drayton DL, von Andrian UH (2006) T cell- and B cell-independent adaptive immunity mediated by natural killer cells. *Nat Immunol* 7:507–16

Rogers DF, Giembycz MA (1998) Asthma therapy for the 21st century. *Trends Pharmacol Sci* 19:160–4

Ronkina N, Kotlyarov A, Dittrich-Breiholz O, Kracht M, Hitti E, Milarski K *et al.* (2007) The mitogen-activated protein kinase (MAPK)-activated protein kinases MK2 and MK3 cooperate in stimulation of tumor necrosis factor biosynthesis and stabilization of p38 MAPK. *Mol Cell Biol* 27:170–81

Salvador JM, Mittelstadt PR, Guszczynski T, Copeland TD, Yamaguchi H, Appella E *et al.* (2005) Alternative p38 activation pathway mediated by T cell receptor-proximal tyrosine kinases. *Nat Immunol* 6:390–95

Schottelius AJ, Giesen C, Asadullah K, Fierro IM, Colgan SP, Bauman J *et al.* (2002) An aspirin-triggered lipoxin A4 stable analog displays a unique topical anti-inflammatory profile. *J Immunol* 169:7063–70

Schottelius AJ, Moldawer LL, Dinarello CA, Asadullah K, Sterry W, Edwards CK III (2004) Biology of tumor necrosis factor-alpha- implications for psoriasis. *Exp Dermatol* 13:193–222

Takanami-Ohnishi Y, Amano S, Kimura S, Asada S, Utani A, Maruyama M *et al.* (2002) Essential role of p38 mitogen-activated protein kinase in contact hypersensitivity. *J Biol Chem* 277:37896–903

Wang X, Xu L, Wang H, Young PR, Gaestel M, Feuerstein GZ (2002) Mitogen-activated protein kinase-activated protein (MAPKAP) kinase 2 deficiency protects brain from ischemic injury in mice. *J Biol Chem* 277:43968–72

Wysk M, Yang DD, Lu HT, Flavell RA, Davis RJ (1999) Requirement of mitogen-activated protein kinase kinase 3 (MKK3) for tumor necrosis factor-induced cytokine expression. *Proc Natl Acad Sci USA* 96:3763–8

Zollner T, Igney FH, Asadullah K (2004) Acute and chronic models of allergic contact dermatitis: advantages and limitations. In: *Animal Models of T Cell-Mediated Skin Diseases.* (Zollner T, Renz H, Asadullah K, eds). Springer Berlin, Heidelberg, New York, ISBN: 3-540-21067-9, 255–75

Zugel U, Steinmeyer A, Giesen C, Asadullah K (2002) A novel immunosuppressive 1alpha,25-dihydroxyvitamin D3 analog with reduced hypercalcemic activity. *J Invest Dermatol* 119:1434–42

nature COMMUNICATIONS

ARTICLE

DOI: 10.1038/s41467-017-01538-9 OPEN

Longitudinal intravital imaging of the femoral bone marrow reveals plasticity within marrow vasculature

David Reismann[1], Jonathan Stefanowski[1,2], Robert Günther[1], Asylkhan Rakhymzhan[1], Romano Matthys[3], Reto Nützi[3], Sandra Zehentmeier[1,2,6], Katharina Schmidt-Bleek[4], Georg Petkau[1], Hyun-Dong Chang[1], Sandra Naundorf[1], York Winter[5], Fritz Melchers[1], Georg Duda[4], Anja E. Hauser[1,2] & Raluca A. Niesner[1]

The bone marrow is a central organ of the immune system, which hosts complex interactions of bone and immune compartments critical for hematopoiesis, immunological memory, and bone regeneration. Although these processes take place over months, most existing imaging techniques allow us to follow snapshots of only a few hours, at subcellular resolution. Here, we develop a microendoscopic multi-photon imaging approach called LIMB (longitudinal intravital imaging of the bone marrow) to analyze cellular dynamics within the deep marrow. The approach consists of a biocompatible plate surgically fixated to the mouse femur containing a gradient refractive index lens. This microendoscope allows highly resolved imaging, repeatedly at the same regions within marrow tissue, over months. LIMB reveals extensive vascular plasticity during bone healing and steady-state homeostasis. To our knowledge, this vascular plasticity is unique among mammalian tissues, and we expect this insight will decisively change our understanding of essential phenomena occurring within the bone marrow.

[1] Deutsches Rheuma-Forschungszentrum, A Leibniz Institute, Charitéplatz 1, 10117 Berlin, Germany. [2] Immune Dynamics, Charité—Universitätsmedizin, Charitéplatz 1, 10117 Berlin, Germany. [3] RISystem AG, Talstraße 2A, 7270 Davos Platz, Switzerland. [4] Julius Wolff Institute, Charité—Universitätsmedizin, Augustenburger Platz 1, 13353 Berlin, Germany. [5] Humboldt-Universität zu Berlin, Unter den Linden 6, 10099 Berlin, Germany. [6] Present address: Department of Immunobiology, Yale University School of Medicine, New Haven, CT 06519, USA. David Reismann and Jonathan Stefanowski contributed equally to this work. Anja E. Hauser and Raluca A. Niesner jointly supervised this work. Correspondence and requests for materials should be addressed to A.E.H. (email: hauser@drfz.de) or to R.A.N. (email: niesner@drfz.de)

The bone marrow is the birthplace of hematopoietic cells in adult mammals. As such, it is a highly dynamic environment, where new blood cells are constantly generated from proliferating hematopoietic precursors and exit the bone marrow into the circulation[1]. At the same time, the bone marrow serves as a harbor for memory cells of the immune system, which reside in the various subtly different microenvironments that support specific immune cell types[2]. These microenvironments are characterized by specialized stromal cell populations, which compose stable components of the niches[3] and provide essential signals for the differentiation and survival of the hematopoietic cells that occupy these niches.

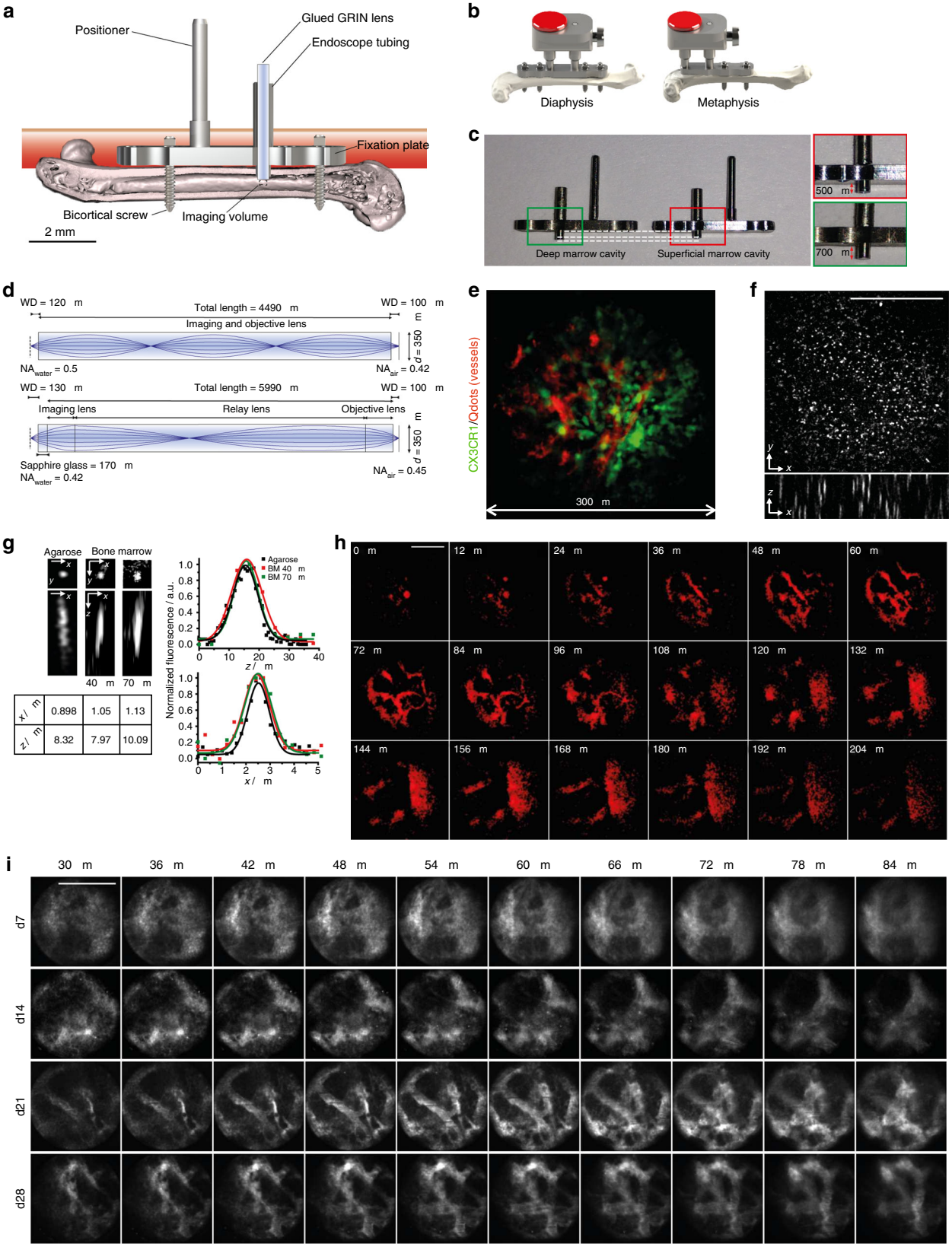

In order to fulfill these functions, the bone marrow tissue is traversed by a dense system of blood vessels comprising arteries, distal arterioles, and sinusoids. These are responsible for transporting cells entering and exiting the bone marrow[4, 5], and also for delivering oxygen, nutrients, and growth factors[1]. The marrow vasculature plays a key role in the regulation of hematopoiesis[6], and hematopoietic stem cell niches are located perivascularly. Recently, a strong link between angiogenesis and osteogenesis, mediated by a defined vessel subtype, characterized by $CD31^{hi}Emcn^{hi}$ (type H) endothelium has been described in the bone marrow. This finding revealed a previously unknown heterogeneity among blood vessels in the bone marrow, supporting the notion of tight functional interactions between marrow and bone[7].

In the recent decade, intravital two-photon microscopy has significantly advanced our understanding of dynamic processes within the immune system. Within the bone marrow, intravital microscopy has helped to elucidate mechanisms of hematopoiesis[8], mobilization of hematopoietic cells[5, 9], and the maintenance of immunological memory[3, 10]. In mice, intravital imaging of bone marrow in areas close to the bone cortex has been performed either in the calvarium[11–13], in the tibia[3, 14], or in the femur[15, 16]. The calvarial preparation takes advantage of the thin sheet of flat bone covering the marrow in this area. Imaging the bone marrow of long bones is more invasive, as it requires the surgical ablation of cortical bone. Both methods have been used mainly as terminal procedures, although imaging at multiple time points has been used for intravital microscopy of both calvarium[17, 18] and long bones (femur and tibia) for imaging durations of hours, over a maximum of 40 days[15, 16]. Nevertheless, up to now there is no available method enabling longitudinal intravital microscopy of the deeper marrow regions in long bones, at sub-cellular resolution, over the time course of several weeks or even months, i.e., both during bone healing and during homeostasis. In order to understand the cellular dynamics occurring in those marrow regions over longer periods of time, an intravital imaging approach allowing longitudinal observation of a fixed region within the bone marrow in one and the same subject is needed.

The development of permanent windows for the brain cortex[19] or of the spinal cord[20] solved the challenge of longitudinal imaging, but limitations regarding the accessibility of deep tissue areas still remained. An elegant solution for this problem was provided by the lab of Marc Schnitzer[21], who used gradient refractive index (GRIN) endoscopic lenses implanted into the brain cortex in order to image deep cortical layers over several weeks. An endoscopic approach was also used previously for single-photon imaging in the femur, by introducing a fiber-optic probe into the femoral cavity through the knee area. This method was used for imaging within a single-plane circular field of view of 300 µm diameter and at a lateral resolution of 3.3 µm. The imaged tissue areas were located at 10–15 µm distance from the endoscope tip[22].

Here, we present a novel method called longitudinal intravital imaging of the bone marrow (LIMB), which allows repeated imaging of the same tissue region in the bone marrow of living mice over the time course of up to 115 days. The approach enables sub-cellular resolution multi-photon imaging of cylindrical tissue volumes ($300 \times 300 \times 200\ \mu m^3$) and is based on the use of a GRIN endoscopic lens mounted on a specialized holder that is surgically fixated to the femur of the mouse. By 28 days post-surgery, reactive processes of the organism to the implant completely cease, and the tissue reaches equilibrium. Using our technique, we are able to demonstrate a high degree of structural plasticity of deep bone marrow vessels not only during bone healing following lens implantation, but also in steady-state homeostasis, with implications for the concepts of micro-environmental stability and niche formation.

Results

Characterization and optical performance of the LIMB implant. In order to understand tissue and cellular dynamics in the bone marrow on a longer time scale, we developed a biocompatible implant—the LIMB implant, which allows micro-endoscopic imaging of the femoral bone marrow.

The implant is based on a fixation plate originally developed to stabilize the mouse femur after osteotomy[23]. Based on the principles of low contact plates developed for fracture healing[23–27], stability is achieved via two angle-stable bi-cortical screws (Fig. 1a, Supplementary Fig. 1d), which fix the plate in a "bridging" position above the bone, to avoid direct contact to the bone surface. This prevents any compression of the bone.

In order to allow repeated intravital imaging deep within the femoral bone marrow, a titanium alloy tube of 600 µm outer diameter and 450 µm inner diameter is mounted onto the fixation plate (Fig. 1a; Supplementary Fig. 1). To account for tissue heterogeneity and to visualize the different bone marrow areas of the femur, two types of implants were designed, allowing us to access either diaphyseal or metaphyseal regions (Fig. 1b). By varying the length of the endoscopic tubing in the marrow cavity (e.g., 500 vs. 700 µm, Fig. 1c), we can image pericortical tissue areas or areas deep in the marrow. For instance, by using a long microendoscopic tubing, we can visualize the endosteum on the opposite side of the bone cortex, in a contact-free manner.

A GRIN lens (Fig. 1d) is positioned in the endoscope tubing and used as a lens for imaging. We use two GRIN lens designs,

Fig. 1 LIMB allows murine long bone imaging in various locations with high resolution. **a** Design and positioning of LIMB implant for longitudinal bone marrow imaging. The LIMB implant is fixed onto the femur using bi-cortical angle-stable screws. GRIN lens systems are placed within the endoscope tubing for imaging and sealed to ensure sterility. The positioner allows adjustment and alignment of GRIN and microscope optical axes. **b** In order to account for tissue heterogeneity, i.e., metaphyseal vs. diaphyseal regions, alternative LIMB designs have been developed. LIMB fixation with four screws allows higher bone stability after osteotomies. **c** Tubing lengths of 500 and 700 µm, respectively, allow access to either peri-cortical or deep marrow regions. **d** Two GRIN lens systems are used for imaging. The single GRIN lens (upper panel) combines the imaging and objective lens function and is glued into the endoscope tubing. The symmetric triple GRIN lens (lower panel) is exchangeable and a sapphire window seals the endoscope tubing. **e** 3D fluorescence image of the bone marrow of a *CX_3CR1:GFP* mouse using the single GRIN lens (myeloid *CX_3CR1^+* cells - green; vasculature labeled by Qdots - red). The maximum field of view is circular, with 280 µm diameter. **f** The PSF was measured on 100 nm beads ($\lambda_{em} = 605$ nm, $\lambda_{exc} = 850$ nm) in agarose, using the single GRIN lens. No significant wave-front distortions affecting the PSF are observed. **g** Qdots are used to estimate PSF in marrow tissue. They reveal slight resolution deterioration with increasing imaging depth. **h** 2D fluorescence images of Qdots-labeled femoral vasculature, 35 days post-surgery, at various *z*-positions between the surface of the single GRIN lens and 204 µm tissue depth. They reveal fine vascularization in the upper layers and a large blood vessel (~100 µm diameter) with emerging branches in the deep marrow. **i** 2D fluorescence images of femoral vasculature acquired at various depths and time points post-surgery, using the triplet GRIN lens. The tissue at the contact surface with the window is characterized by de novo micro-vascularization, i.e., granulation tissue. Its thickness varies between individuals and decreases over time after implantation. Scale bars = 100 µm

both with a diameter of 350 µm. The first design (Fig. 1d, upper panel) consists of one single GRIN lens of 4.49 mm in length, a numerical aperture (NA) of 0.5 at the object side and a field of view of 280 µm in diameter (Fig. 1e). The lens is permanently and stably glued into the tubing, thereby sealing it to maintain sterility within the marrow cavity and ensuring fixed positioning of the optical path. The second design (Fig. 1d, lower panel) consists of a system of three GRIN lenses with NA 0.42 at the object side, 5.99 mm in length and a field of view of 150 µm diameter. This GRIN system requires a 170 µm thick sapphire window for optimal optical performance, which is attached to the tubing and seals the implant. Thus, this design allows flexible replacement of the GRIN lens system for applications requiring different optical properties. A 45° prism can be glued at the end of the GRIN lens to achieve a side view of the marrow tissue and access additional tissue areas.

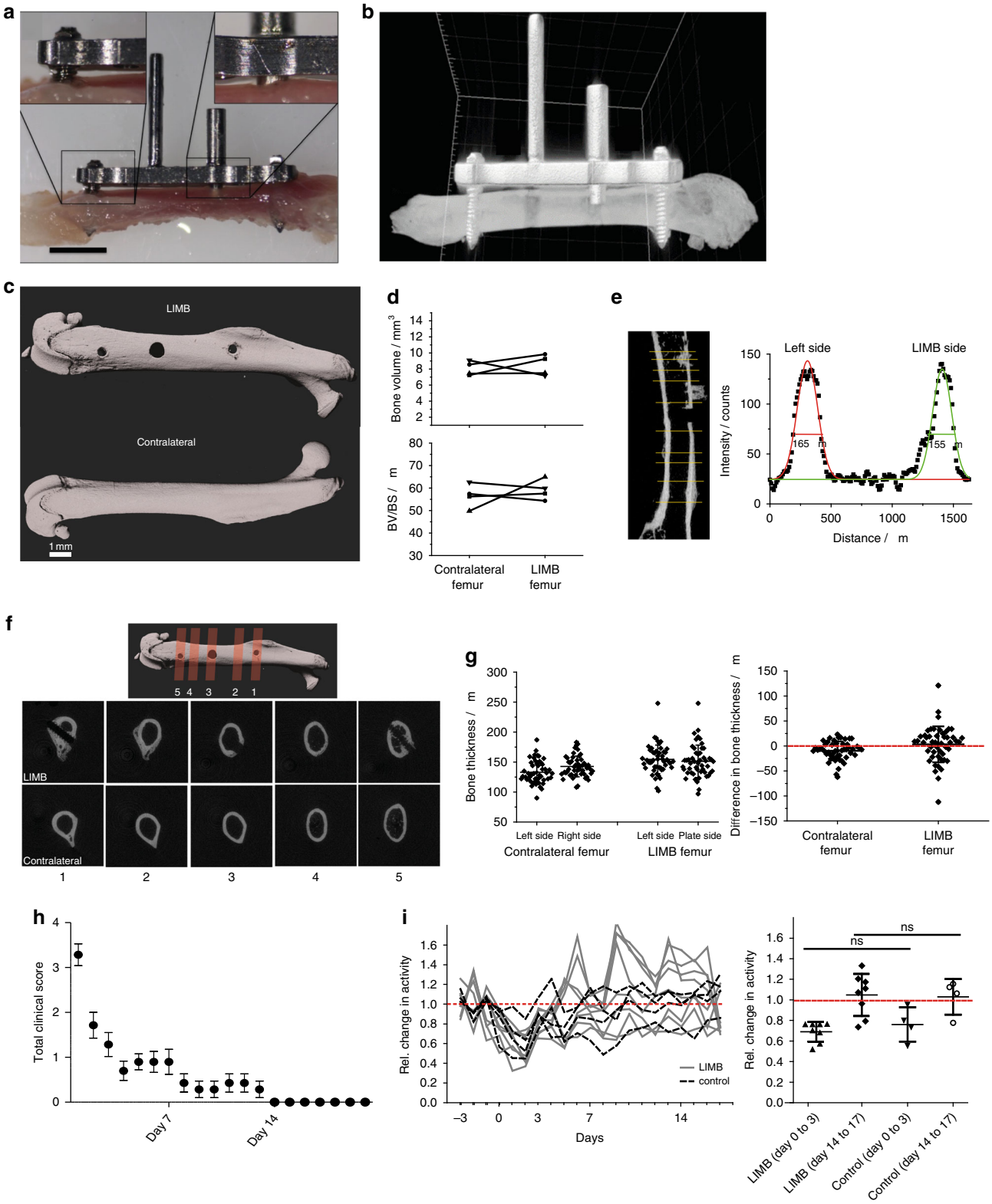

The LIMB implant is surgically fixated onto the right femur of mice (Supplementary Figs. 2b, 3) to intravitally visualize tissue dynamics by multi-photon microscopy. The use of multi-photon excitation permits imaging deep into tissue. The implant is completed by a titanium-alloy reference plate (Fig. 1b, Supplementary Figs. 1, 2a) mounted onto the positioner and the endoscope tubing, which allows stable, reproducible positioning of the mice under the microscope. This reference plate couples with a custom-built adapter used to align the optical axes of the microscope objective lens (20×, NA 0.45) and of the GRIN lens, thereby transferring the focus from the microscope objective through the GRIN lens into the marrow tissue (Supplementary Figs. 2b, 3h).

To characterize the optical properties of LIMB, we first determined the point spread function (PSF) of the GRIN lens systems using 100 nm fluorescent beads (emission at 605 nm, excitation at 850 nm) in agarose. Using the one-lens GRIN design, the spatial resolution was 0.8 ± 0.1 µm (s.d.) laterally and 5.2 ± 0.5 µm axially, corresponding to theoretical values for NA 0.5 ($n = 23$ beads). The three-dimensional PSF was not distorted by optical aberrations over the entire field of view (Fig. 1f). Using the three-lens GRIN system with the sapphire glass window, we measured a spatial resolution of 0.9 ± 0.2 µm laterally and 8.0 ± 1.1 µm axially (Fig. 1g), also corresponding to the theoretical values for NA 0.42 ($n = 18$ beads).

Within the bone marrow, the spatial resolution was evaluated using quantum dots 655 (Qdots). While most of these nanoparticles remained within the blood vessels, some Qdots entered the parenchyma due to the fenestrated sinusoids of the bone marrow and were observed as single fluorescent spheres of sub-resolution sizes. Typically, resolution values of 1.0 ± 0.1 µm laterally and 7.4 ± 1.6 µm axially were achieved within the imaging volume between 40 and 70 µm distance from the surface of the GRIN lens (at each depth, $n = 8$ Qdots).

The maximum extent of the imaging volume within the bone marrow using the one-lens GRIN system started from the endoscope surface at 0 µm and reached down to 204 µm within the bone marrow (Fig. 1h). It included regions with superficial small sinusoids and arterioles, as well as deeper-laying large blood vessels including the central sinus. We reliably achieved a signal-to-noise ratio of at least 5, independent of inter-individual variance and of the imaging time point after surgery.

At early time points post-surgery, we typically visualized granulation tissue, characterized by a tight network of small blood vessels within a large area in the imaging volume (~30–85 µm in depth). Over time, this granulation tissue retracted to the area next to the GRIN optics and was replaced by normal-appearing bone marrow vasculature, resembling the vasculature as observed by calvarial and tibial imaging preparations. At late time points post-surgery, from 28 days onwards, we observed complete resolution of this granulation layer (Fig. 1i).

Local and overall tissue recovery after implantation. First, we determined to what extent the surgical procedure and the presence of the implant itself affected the mice and impacted on bone physiology. As shown in Fig. 2a, b and Supplementary Movie 1, we confirmed that the low contact plate design does not compress the bone, instead, a gap of at least 100 µm remained between bone surface and plate. After removal of the plate (day 7 post-implantation), reconstructed µCT images of the bone surface appeared smooth in the area where the plate had been, comparable to the surface of contralateral bones (Fig. 2c). Furthermore, no differences in bone volume, ratio of bone volume to bone surface (BV/BS), bone shape or thickness were found between the LIMB-implanted and contralateral femurs (Fig. 2d–g). In order to determine the impact of the surgery on the mice, we clinically scored the animals immediately after LIMB implantation, taking parameters such as weight, general appearance, and vitality into account. The data recorded from 79 mice indicate that the animals reached a low level of burden (as reflected in a score of 1) by post-surgical day 3, and normal values for all parameters were reached within 14 days after surgery (Fig. 2h). In addition, the general activity of mice that received the LIMB implant was recorded, starting 3 days pre-surgery until 18 days post-surgery (Fig. 2i, left panel). By transponder-based tracking, we recorded the movement of each mouse, thereby generating individual motility profiles of LIMB-implanted and co-housed mice, which had undergone sham treatment (without implantation). The mean activity levels dropped to a similar extent in both implanted and sham-treated groups within 3 days post-surgery, when compared to pre-surgical levels. By day 14 after surgery, at a time point when clinical scores were normal again (Fig. 2h), the activity of the mice in both groups also returned to pre-surgical levels (Fig. 2i, right panel). Interestingly, at both early and late time points post-surgery, there were no significant differences between sham-treated and LIMB-implanted mice. In order to analyze the effects of the surgical intervention and of the implant on the gait of the animals, the open-field behavior of the mice was recorded (Supplementary Movie 2) at day 2, 6, 9, 13, and 21 post-surgery. No severe gait abnormalities were observed at any time ($n = 79$).

In order to assess the effects of the LIMB implant on the bone with respect to post-surgical inflammation and bone formation adjacent to the LIMB microendoscope, we performed immunofluorescence and histochemical analysis (Fig. 3a–c). The most striking changes within the marrow of the implant-bearing

Fig. 2 Effect of LIMB implantation on bone tissue, general health, and activity of the mice. **a** Picture of an explanted femur including the LIMB implant shows the fixation plate bridging between the angle-stable screws, thereby preventing direct contact to the bone surface/periosteum. Scale bar = 2 mm. **b** 3D reconstructed µCT images of a femur bearing the LIMB implant confirm no direct contact between bone and fixation plate. Shadows below the positioner are beam hardening artifacts of the high attenuation titanium alloy. **c** 3D reconstructed µCT images of an intact femur (lower panel) and a femur after removal of the LIMB implant (upper panel). Bone surface under the fixation plate 7 days after implantation appears similar to the bone surface of the intact femur. Bone growth is observed only around the bicortical screws. **d** Total bone volume (upper panel) and BV/BS (lower panel) of LIMB and contralateral femur, respectively ($n = 4$ mice). **e** Longitudinal cross-section through a µCT reconstruction of a femur after implant removal (left panel). Yellow lines represent the positions chosen to measure the bone thickness. For each position, the intensity profile was approximated with two Gaussian curves as indicated in the left graph. **f** 3D reconstruction of µCT data showing the planes of transverse cross-sections displayed in the lower two panels. At day 21 after implantation, calcified bone forms around the bicortical screws, but not around the endoscope tubing. Cross-section µCT images at the sites of the screws show enough space for the bone marrow tissue to connect the diaphysis with the metaphysis. **g** No differences in bone thickness between contralateral and LIMB femurs are measured ($n = 5$ mice). **h** Total clinical score over 3 weeks post-surgery based on behavior and appearance of the individual mice ($n = 79$ mice). **i** Physical activity of LIMB implanted mice, pre-surgery and post-surgery, and of co-housed control mice. The LIMB-implanted mice reach their pre-surgical activity level within the same time as sham-treated controls (right graph) (two independent experiments; $n = 8$

femurs were an accumulation of CD45$^+$ cells, and enhanced expression of the extracellular matrix (ECM) component laminin in tissue regions around the implant, peaking at day 3 post-surgery. Some of the cells with hematopoietic morphology were Sca-1$^+$ckit$^+$ and may represent progenitors (Supplementary Fig. 4a). We also detected CD45$^-$Sca-1$^+$ cells in elongated structures surrounded by laminin, likely representing arterioles sprouting into the injured area (Supplementary Fig. 4b). These changes occurred around the sides of the implanted tube and in front of the sapphire glass window, reaching a depth of up to 400 µm. By day 7, the inflamed area as indicated by laminin, Sca-1 and CD45 shrunk to a thickness of ~100 µm. The tissue structure further normalized at day 14 and by day 28, the area in front of the imaging window typically consisted of laminin$^+$ vessels

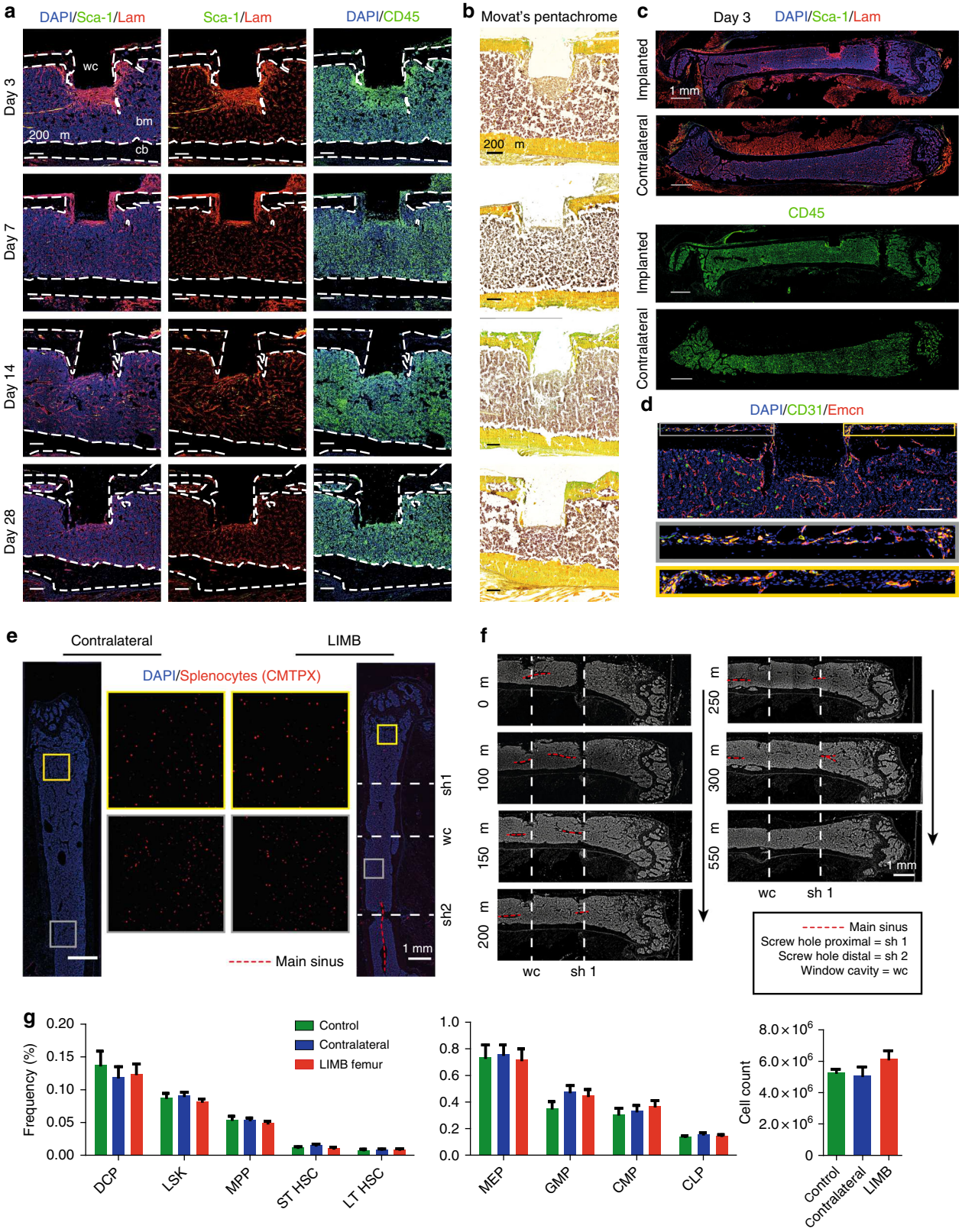

surrounded by CD45$^+$ hematopoietic parenchyma, in a pattern resembling the other regions of the bone marrow and the contralateral (non-implant-bearing) femur. Movat's pentachrome staining showed that, although in some mice bone formation occurred lateral to the implanted tube emanating from the cortex, no new bone formed in front of the imaging window. Besides these changes in the tissue occurring adjacent to the implant and screws, the overall structure of the bone marrow was unaltered with respect to the overall distribution of leukocytes, ECM components, and vessels when compared to the contralateral bone (Fig. 3c). At the site of the periosteum, vascularization was detected (Fig. 3d). In order to test whether the implant impairs blood flow throughout the bone, we adoptively transferred CMTPX-labeled splenocytes via the tail vein, harvested the bones 4 h later and analyzed the distribution of CMTPX$^+$ cells by fluorescence histology. In histological sections, CMTPX$^+$ cells were distributed throughout the marrow in both the contralateral and the LIMB-implanted femurs (Fig. 3e). Importantly, engraftment occurred on both sides of the bicortical screws. Consistent with this observation, longitudinal serial sections showed clearly that the bicortical screw did not completely separate the bone marrow and did not impair the blood flow in any part of the marrow. Additionally, we performed μCT of implanted bones, which also showed clearly that the bone marrow was not completely separated by the bicortical screws (Fig. 3f and Supplementary Movie 1). In order to verify whether hematopoiesis within the bone marrow was altered, we performed flow cytometry on bone marrow cells of LIMB-implanted mice, and quantified the major hematopoietic progenitor populations. No significant differences in the frequencies or total cell counts of the analyzed populations were observed compared to bone marrow from contralateral femurs or bone marrow from non-treated mice (Fig. 3g and Supplementary Fig. 5).

B lymphocyte motility in femur, calvarium, and tibia. In order to observe the dynamics of B-lineage cells within the femoral marrow, we chose *CD19:tdRFP* mice as recipients of the LIMB implant. In these mice, Cre recombinase activity in CD19-expressing cells leads to the removal of a STOP cassette and expression of tdRFP in the B cell lineage, starting in the late pro-B cell stage. The vasculature was labeled using Qdots. Mice were imaged starting at day 7 (Fig. 4a; Supplementary Movies 3, 5–7), up to maximally day 115 post-surgery (Supplementary Movie 12).

Using LIMB in *CD19:tdRFP* mice, under homeostatic conditions, i.e., at day 60 or 90 post-surgery, we found that tdRFP$^+$ cells of various volumes displayed different motility patterns. We distinguished the subtypes of B lymphocytes based on their size, and tracked them to assess their velocity and displacement rate. A maximum diameter of 10 μm corresponds to a spherical volume of ~500 μm^3, therefore these cells presumably represent B cells, displaying a high degree of directed motility, in line with previous reports[5]. Larger tdRFP$^+$ cells in this system represent rather static plasma cells, consistent with the concept of their residence in bone marrow niches (Fig. 3c) and with our previous work[3]. In order to compare the motility of B-lineage cells in the femur to other bone marrow compartments, we performed intravital imaging of calvaria and tibia of *CD19:tdRFP* mice. Notably, we found no significant differences in the motility of bone marrow B and plasma cells when comparing femur (LIMB), calvarium, and tibia (Supplementary Movies 4, 8, 9; Fig. 4b–e).

Long-term stability of the LIMB implant. In order to test the positional stability of the LIMB implant, the microendoscope was implanted in mice ubiquitously expressing photoactivatable green fluorescent protein (paGFP). Prior to photoactivation, paGFP is non-fluorescent upon 940 nm illumination. Photoactivation at 840 nm leads to 100-fold increase in green fluorescence upon excitation at 940 nm[28]. *PaGFP* mice were injected with Qdots to label the vasculature and were imaged before and after photoactivation (Fig. 5a, two upper rows). The photoactivation area was either 75 × 75 or 100 × 100 μm^3 positioned within the center of the field of view (Supplementary Fig. 6). We analyzed paGFP fluorescence by repeated imaging every 6–12 h (Fig. 5a, third to last row) and detected paGFP fluorescence at the same area at least 36 h after photoactivation. Thus, we confirmed the high positioning stability of the LIMB implant with respect to the implantation/imaging site in the bone. The fluorescence signal of paGFP decreases over the time span of hours/days due to the emigration of hematopoietic cells out of the photoactivated region (Supplementary Movies 9, 10) and due to protein turnover, causing fluorescent paGFP to be replaced by newly synthesized, non-fluorescent paGFP. The imaging data acquired in *paGFP* mice reveal that while the field of view labeled by photoactivation remains stable, morphological changes of the vascular system do not cease after day 28 post-surgery and seem to depend on the vessel diameter (Fig. 5a). In order to exclude that such changes are caused by the LIMB implant itself, we performed longitudinal imaging in the calvarium of *paGFP* mice, over a volume of 500 × 500 × 66 μm^3. We were able to repeatedly detect paGFP fluorescent areas in the calvarial marrow islets for up to 72 h after photoactivation, and observed paGFP cells leaving this area. Similarly to LIMB, we also detected drastic changes in the marrow vasculature, most prominent in smaller vessels (Fig. 5b; Supplementary Fig. 7).

Fig. 3 The bone marrow within the imaging volume reaches steady-state comparable to homeostasis 28 days after LIMB implantation. **a** Immunofluorescence analysis of bone sections after removal of the LIMB implant over the time course of 4 weeks. ECM formation was identified by the marker Laminin (Lam). Stem-cell antigen 1 (Sca-1) is highly expressed in arterioles. The leukocyte marker CD45 indicates localization of inflammatory cells adjacent to the window cavity (wc). Lam is highly expressed around the implant during the first week and completely normalizes after 2–4 weeks. CD45$^+$ cell accumulations are found during the first weeks in proximity to the wc. **b** Movat's pentachrome stain detects connective tissues and reveals remodeling of bone primarily on the periosteal interface near the fixation plate. **a**, **b** Images are representative for 3–5 mice per time point post-surgery. **c** Overview immunofluorescence images of the femoral bones from an individual mouse 3 days post-surgery. Note the specific reaction to the implant-bone marrow interfaces indicated by accumulations of CD45$^+$ cells, and Lam$^+$ and Sca1$^+$ arteries (yellow). bm bone marrow, cb cortical bone. **d** Immunofluorescence image of the region around the endoscope tubing in a LIMB-implanted femur 7 days post-surgery, including the bone cortex and periosteum under the plate. The presence of various blood vessel subsets indicated by CD31 and Emcn demonstrates intact blood supply to the periosteum and to the bone. Scale bar = 100 μm. **e** Blood supply is intact throughout the marrow cavity, indicated by CMTPX-labeled splenocytes, which localize in the bone marrow 4 h after transplantation in both contralateral and LIMB-implanted femurs at 42 days post-surgery ($n = 3$ mice). **f** Histological DAPI stain (gray) shows intact tissue structure, with no separation of the bone marrow and the vasculature by the screws or endoscope tubing. **g** Flow cytometry analysis of femurs with the LIMB implant, their contralateral femurs and femurs of control mice. Similar frequencies and cell counts of various cell populations shows no effect of the LIMB implant on bone marrow cell composition ($n = 8$ LIMB-implanted mice, $n = 8$ controls, two independent experiments). Error bars represent s.e.m. values. Statistical analysis was performed using *t*-test

Vascular plasticity during healing phase and homeostasis. Using LIMB, we observed drastic changes in the vascular morphology within the femoral marrow after implantation, both during the healing phase and after reaching steady-state. These changes were not caused by instability of the microendoscope or by inaccuracy during repeated selection of the imaging volume, as demonstrated by the results of our photoactivation experiments.

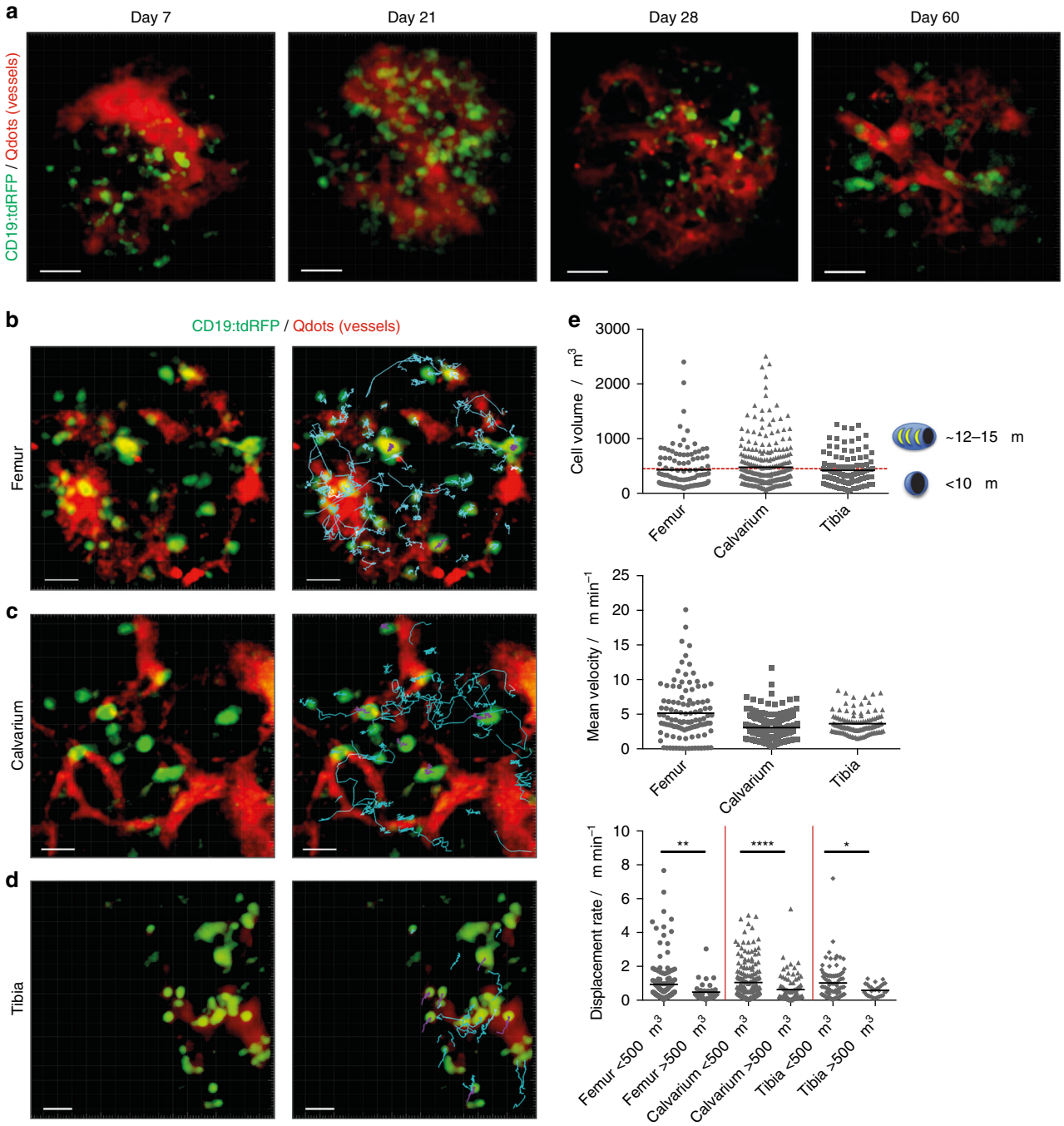

Fig. 4 Immune cell dynamics in different bone types show comparable motility patterns. **a** 3D fluorescence images acquired by LIMB in the femoral marrow of a *CD19:tdRFP* mouse at day 7, day 14, day 28, and day 60 after surgery. Mature B lymphocytes express tdRFP and are displayed in green, whereas the vasculature was labeled with Qdots and is displayed in red. Scale bar = 50 μm. All images are snapshots of 45 min movies, with images acquired every 30 s. The movies are provided as Supplementary Material. **b** Time-lapse 3D fluorescence image acquired by LIMB in the bone marrow of a *CD19:tdRFP* mouse at day 90 post-surgery. The tracks of the B lymphocytes smaller than 500 μm^3 (defined as B cells with a maximum diameter of 10 μm) are shown in cyan, whereas those with a volume larger than 500 μm^3 (defined as plasma cells) are shown in violet. Scale bar = 30 μm. **c** Similar to **b**, time lapse 3D image of the bone marrow of a *CD19:tdRFP* mouse with corresponding tracks of B and plasma cells in the calvarium and **d** the tibia. Scale bar = 30 μm. Representative movies with cell motility tracks for LIMB, calvarial, and tibial imaging are provided as Supplementary Material. **e** Quantification of cell volumes, mean velocities, and displacement rates of B lymphocytes from movies acquired by LIMB ($n = 4$ mice), within the calvarial bone ($n = 3$ mice), and the tibia ($n = 2$ mice). Similar cell subset frequencies and mean velocities of B lymphocytes were measured by LIMB in the femoral bone marrow, by calvarial imaging as well as by tibial imaging. We statistically analyzed the data in **e** using *t*-test (*$p < 0.05$; **$p < 0.01$; ***$p < 0.001$)

As expected, we observed dynamic blood vessel re-organization between day 7 and 21 post-surgery. Interestingly, even between day 27 and 60, a time span in which the tissue composition in front of the microendoscope is comparable to non-implanted bone marrow (Figs. 2, 3), the vasculature continued to change massively (Fig. 6a). Starting from day 27 post-surgery, with a time

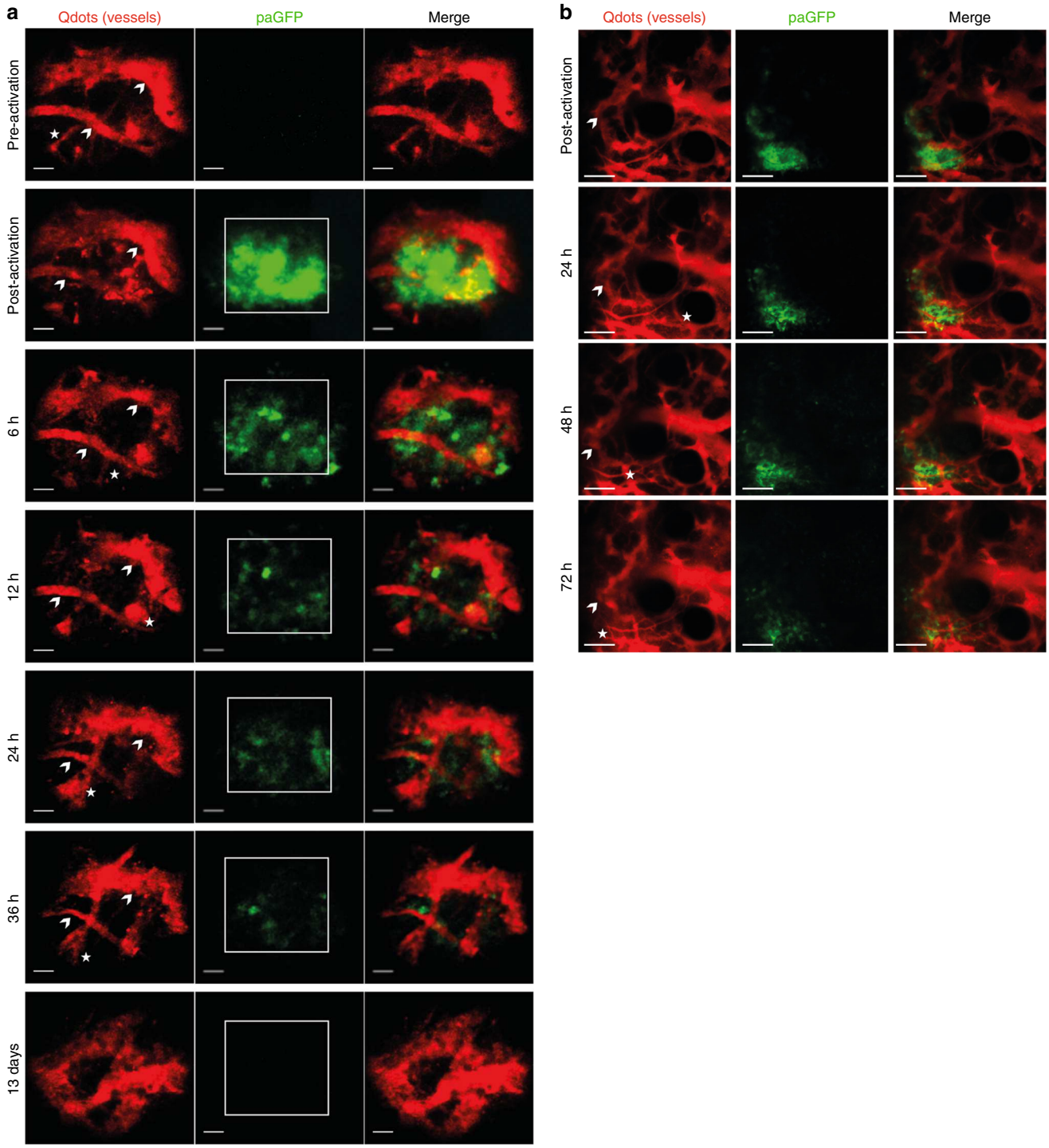

Fig. 5 Imaging of locally activated paGFP in murine deep femoral marrow reveals high positioning stability of the LIMB implant. **a** *paGFP* mice were implanted with a LIMB microendoscope ($n = 3$ mice). After 35 days, the mice were injected intravenously with Qdots to label the vasculature. Photoactivation of paGFP was performed at a wavelength of 840 nm in a $75 \times 75 \times 30\ \mu m^3$ square area in the center of the field of view. Additional injections of Qdots were given before each recording. We performed the described photoactivation experiments repeatedly, up to three times in the same animal at day 27, 35, and 56 post-surgery, during homeostasis with similar results. Blood vessels which could be observed over the whole period of 36 h are indicated by arrowheads, whereas those that appear or disappear within this time period are labeled by asterisks. Scale bar = 30 μm. **b** Similarly to **a**, photoactivation of a $150 \times 150 \times 9\ \mu m^3$ region within the $500 \times 500 \times 66\ \mu m^3$ field of view in a *paGFP* mouse with a permanent calvarial imaging window let us easily identify the photoactivated area. The paGFP fluorescence could be visualized over several imaging sessions. Scale bar = 100 μm. During these time windows we observed changes of the vasculature in both, the deep femoral marrow and bone marrow islets of the calvarium

resolution of 7 days between imaging sessions, the pattern of large blood vessels (>50 µm) changed between consecutive time points, making their use as tissue landmarks impossible (Fig. 6b). Only by further increasing the time resolution in LIMB, during the homeostatic phase, i.e., shortening the interval between imaging sessions to every 6–24 h (Fig. 6c), were the vessels stable enough to be used for orientation. We found that blood vessels with diameters in the range of 5–15 µm had the highest degree of volume change within the time span of 24 h (Fig. 6d, Supplementary Movie 13). Within the same period, large blood vessels (>35 µm) changed rather slowly, whereas middle-sized blood vessels with a diameter between 15–35 µm displayed an

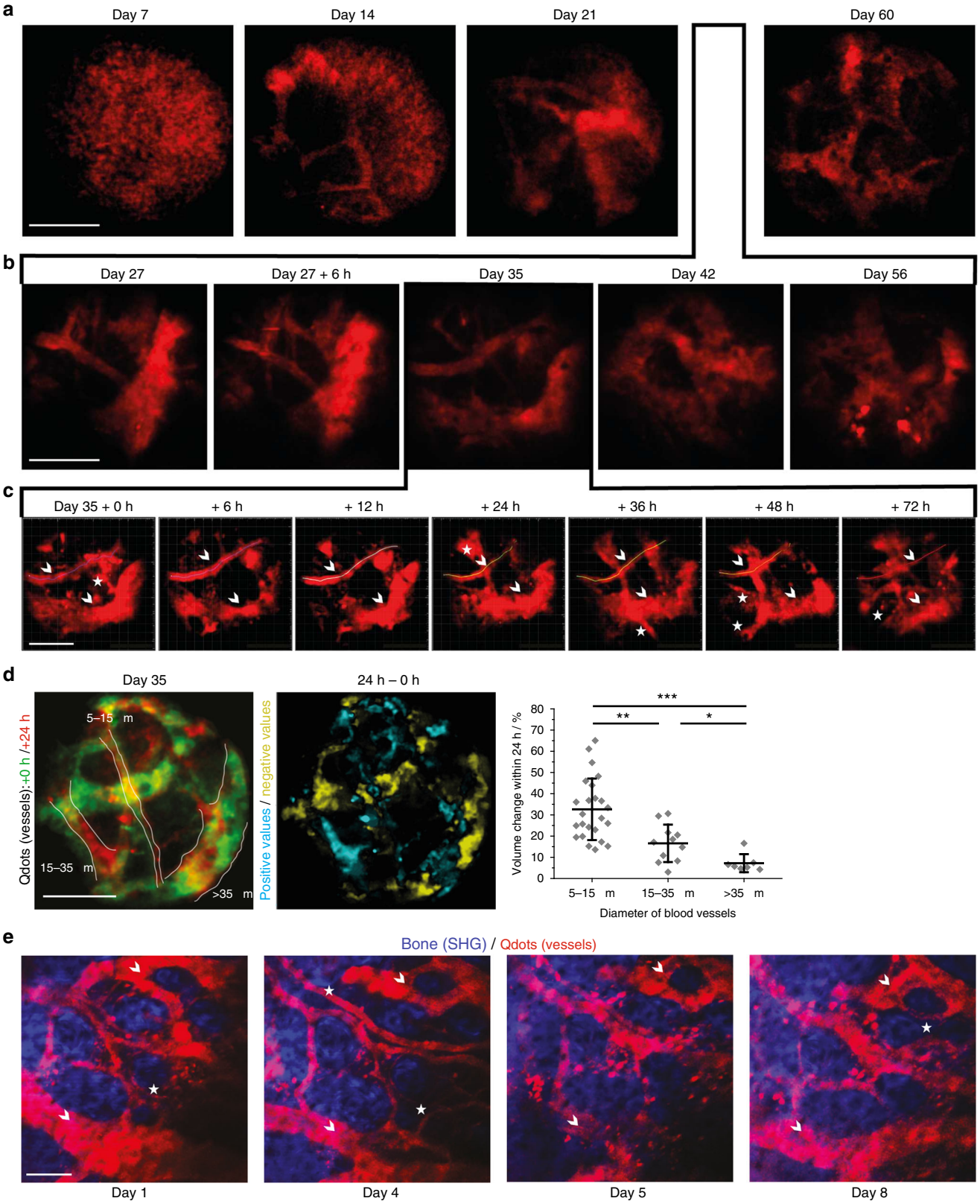

intermediate degree of remodeling. Notably, we observed a comparable remodeling in the vascular compartment of the marrow islets of the calvarium, over a time course of 8 days (Fig. 6e). As the surgery for longitudinal calvarial imaging does not disrupt the integrity of the bone, we can rule out that the vascular plasticity was an effect caused by the femoral implant and confirm the physiological nature of this vascular remodeling. However, due to the fact that calvarial marrow islets are rather small as compared to the cortical bone areas, the dramatic vascular plasticity remained underestimated until now. Only by using LIMB, we were able to observe and quantify these changes.

Possible mechanisms of femoral vascular plasticity. In order to investigate whether vascular remodeling was the result of active angiogenesis related to de novo bone formation, we performed immunofluorescence analysis of bone sections (Fig. 7). A recent publication described CD31^{hi} Endomucin (Emcn)^{hi} (type H) bone marrow endothelium to be involved in osteogenesis-related angiogenesis in the bone marrow[7]. In line with previous reports[29], we found type H vessels to be abundant at the growth plate of young mice, but only few type H vessels were present in aged mice (Supplementary Fig. 8a). In contrast, type H vessels close to the bone cortex were found at all ages (Supplementary Fig. 8a), consistent with age-independent bone remodeling at this site. We examined the bone marrow for the presence of type H vessels following implantation (Fig. 7a) and detected them during the early healing phase (days 3–14) in tissue areas next to the microendoscope. At day 28 post-surgery, only few type H vessels were found in proximity of the microendoscope and their shape and abundance were comparable to the vessels present at bone–bone marrow interfaces. Together, this indicates a state of homeostasis, consistent with the previously observed time course of regeneration (Fig. 3).

In line with the vascular remodeling within the bone marrow, we observed marked changes in the stromal network in *Prx-1:YFP* mice (Supplementary Fig. 9). During homeostasis, the stromal network remodeling continues, similar to the vascular reorganization. Repeated imaging experiments in *paGFP* mice every 6–12 h after photoactivation, over a total time of 36 h (Fig. 5), revealed fluorescent cells, presumably stromal cells, persisting over the whole time span of 36 h, as well as highly motile fluorescent cells, presumably hematopoietic cells, leaving the photoactivated volume. Over the course of these 36 h the vasculature continuously changed its shape. In order to assess whether the remodeling process involves proliferation of the endothelial cells, we administered the thymidine analog EdU to label newly synthesized DNA[3] to mice that had received a LIMB implant either 3 or 42 days earlier. EdU labeled a similar fraction and comparable pattern of hematopoietic cells distributed over the whole bone marrow in both cohorts ($n = 3$ mice in each cohort). We did not detect an overt proliferation of endothelial cells in the tissue surrounding the implant (Fig. 7b). Similarly, staining for the proliferation marker Ki67 did not show any accumulation of proliferating endothelial cells at the implant site, at any time point (Supplementary Fig. 8b). Taken together, these data support the hypothesis that the observed dynamics are the result of passive displacement of the vessels, probably caused by dynamics and cell proliferation in the surrounding tissue (Fig. 7c; Supplementary Movies 10, 11), rather than active proliferation in the vascular compartment. The exact kinetics and mechanisms of the vascular and stromal remodeling during the steady-state will be subject of further studies, as they impact on many processes taking place in the bone marrow.

Discussion

While intravital imaging of the bone marrow has previously been performed[3, 11–18, 22], longitudinal multi-photon imaging in the deep marrow of long bones over the time course of months was not feasible. Longitudinal microscopic and microendoscopic imaging of the CNS[20, 21], retina[30], or lymph nodes transplanted into the ear of mice[31] has been reported, and blood vessels have been used as anatomical reference points, allowing the recognition and imaging of the same regions within the tissue.

The bone marrow contains quiescent and activated hematopoietic stem cells in dedicated perivascular tissue niches[6, 29], and is the tissue in which most leukocytes complete their development. The bone marrow actively participates in immune reactions[32, 33] and is an important site for the maintenance of immunological memory[3, 10, 34, 35]. The interaction of hematopoietic cells with stromal cells plays a crucial role in these processes: subtypes of vascular cells provide niches for the maintenance of hematopoietic stem cell quiescence[6], and stromal cells in the bone marrow provide cytokines, which support the survival and differentiation of developing hematopoietic cells. Endothelial cells mediate leukocyte trafficking between the circulation and the bone marrow parenchyma[6], guiding immune memory cells back into the bone marrow together with stromal cells, which provide chemotactic cues and anchor the memory cells in their niches[36]. Moreover, the role of the immune, vascular and bone compartments during distinct phases of bone regeneration still remain elusive. Hence, there is a clear need for longitudinal imaging technologies to allow the investigation of dynamic processes at the cellular and sub-cellular level in this organ.

The GRIN lens microendoscopic implant presented in this work allows for the first time imaging of dynamic cellular

Fig. 6 LIMB approach reveals kinetics of vascular remodeling during bone healing and homeostasis on time scales from hours to months. *C57/B6J* mice received the LIMB implant and were injected intravenously with Qdots (red) prior to each LIMB imaging session to label the vasculature. Vessels were three-dimensionally imaged at increasing time resolution over the course of **a** weeks **b** days and **c** several hours. In line with our previous observations, we noted prominent changes in the vasculature, which continued over the whole monitoring time period, even after homeostasis is reached ($n = 5$ mice, two independent experiments, scale bar = 50 μm). Small vessels continuously appear and disappear, larger vessels change their position and shape. The trace of such a larger vessel is displayed at all time points as a line in **c**. Blood vessels which can be used as landmarks are labeled by arrowheads and those that completely disappear within days are labeled by asterisks. **d** Overlap of the 3D projections of blood vessels in a mouse 35 days post-surgery (+0 h, green) and 24 h later (+24 h, red). A differential image between the two 3D images was generated. Blood vessel volume change was calculated by dividing the fraction of the volume difference between +24 h and 0 h (cyan areas in the middle panel indicate positive values, i.e., appearance of blood vessels; yellow areas indicate negative values, i.e., disappearance of blood vessels) by the total volume of the blood vessel at +24 h (delineated by white lines in the left panel) to obtain a normalized parameter of vessel volume change. The normalized volume changes (right panel) are dependent on the blood vessel diameter, with small vessels remodeling more rapidly than large vessels ($n = 6$ mice, scale bar = 100 μm). **e** Similar to the observations in the deep femoral marrow, repeated imaging of blood vessels in calvarial bone and bone marrow also showed remodeling of the vasculature ($n = 3$ mice, two independent experiments). Scale bar = 100 μm. Error bars represent s.d. values. Statistical analysis in **d** was performed using an ANOVA test (*$p < 0.05$; **$p < 0.01$; ***$p < 0.001$)

processes in the deep femoral marrow, repeatedly, over a time period of up to several months. The central marrow represents an area, which has been inaccessible to intravital multi-photon imaging until now; our technique permits imaging of this tissue for the unprecedented duration of 4 months within the same bone marrow region. Importantly, this time period covers not

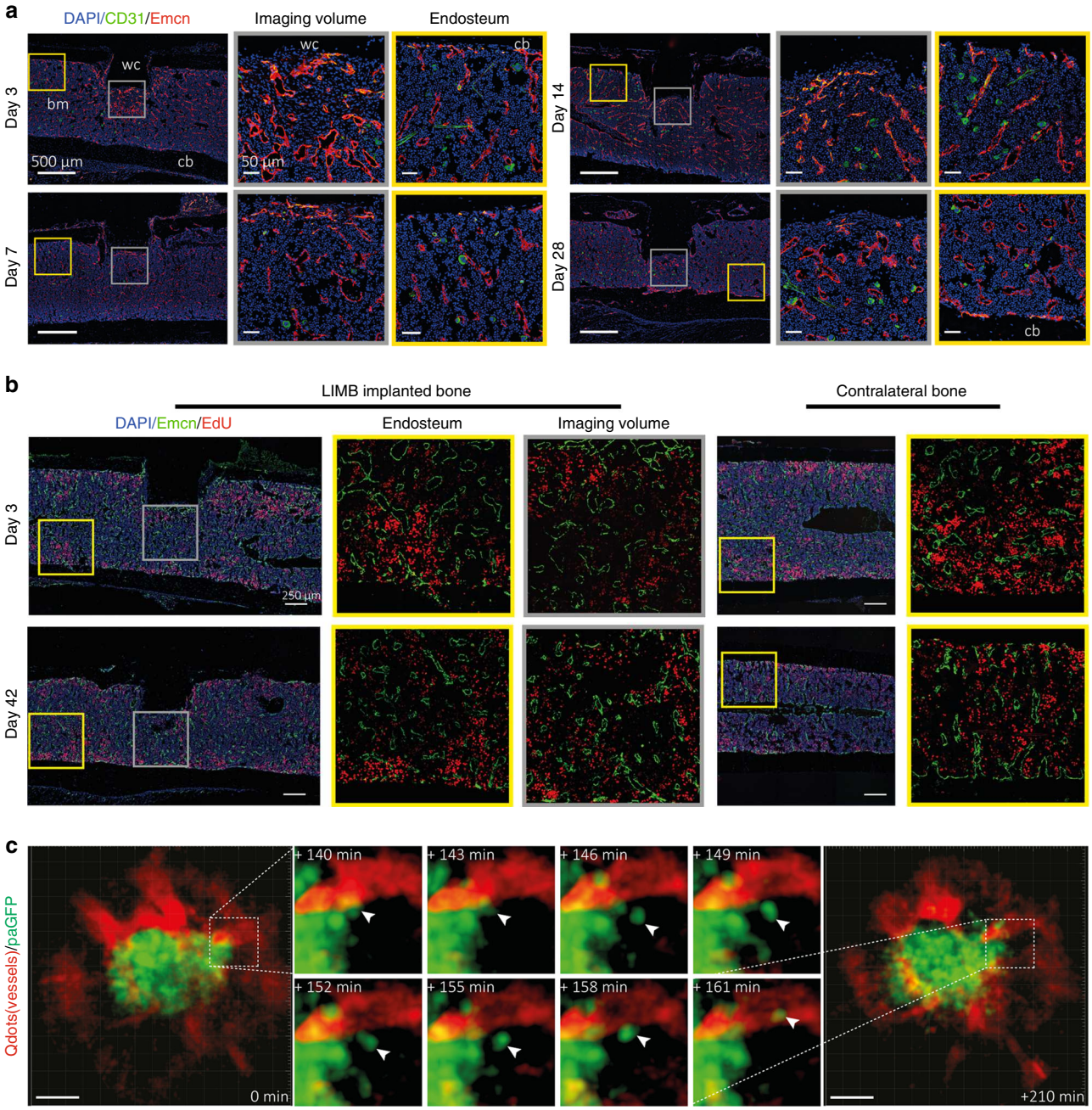

Fig. 7 LIMB and immunofluorescence analysis indicate possible mechanisms of vascular morphological changes deep in the femoral bone marrow, during regeneration, and in steady-state homeostasis. **a** Immunofluorescence analysis shows that type H vessels, characterized by CD31^{hi}Emcn^{hi}-expressing endothelial cells, are induced and present around the implant at day 3 after LIMB implantation. Their presence may vary individually but normalizes within 28 days post-surgery. Sinusoidal and type H vessel morphology adjacent to the wc is irregular in the first week and completely reorganizes to an appearance comparable to vessels found at endosteal areas distant from the injury site ($n = 3$ mice). bm bone marrow, cb cortical bone. Scale bar = 500 µm (left panels). **b** Immunofluorescence analysis after EdU pulse-chase experiments indicates similar EdU-uptake in the bone marrow of LIMB-implanted femurs and contralateral bones. Proliferating endothelial cells were rarely present at late time points after implantation. This result also supports the conclusion that 28 days after LIMB implantation both the bone and the bone marrow reach homeostasis ($n = 3$ mice in each cohort). **c** 3D fluorescence image (300 × 300 × 66 µm^3, left and right panel) acquired by LIMB 26 days post-surgery, in a *paGFP* mouse with the vasculature labeled by Qdots. Photoactivation was performed within a volume of 100 × 100 × 9 µm^3 in the center of the image. The fluorescence image was acquired 2 h post activation. Scale bar = 50 µm. The middle panel shows time-lapse 3D images of the inset from the left panel, indicating that paGFP fluorescent cells outside the initial photoactivation volume are present 3 h after photoactivation and that they fluctuate in number and position within the tissue. Passive displacement of the relatively immobile stromal and vascular compartments by continuous proliferation and movement of hematopoietic cells is a possible mechanism of tissue and vascular re-localization during homeostasis (see Supplementary Movies 10, 11)

only the bone healing phase, but also allows imaging during post-operative steady-state homeostasis, as demonstrated in this work.

As a microendoscopic approach, LIMB allows imaging of areas between 100 and 500 µm deep within bone marrow tissue, which are not accessible to existing intravital microscopy preparations. Whereas the maximum field of view of 280 µm in diameter and the spatial resolution are comparable to those achieved by the established longitudinal conventional intravital multi-photon microscopy, the imaging volume is fixed. This represents both a benefit, since the implant itself functions as a landmark for orientation in tissue, but also a limitation, since covering the relevant tissue areas can be more challenging than with other imaging methods.

Along that line, as we and others have previously shown[3], the deep bone marrow in diaphyseal regions does not show a supra-cellular compartmentalization, in contrast to secondary lymphoid organs, which are divided into zones that primarily host certain immune cell subtypes. In order to address tissue heterogeneity in the bone marrow, we developed various designs of our implant that allow positioning of the GRIN lens at various locations within the bone marrow, based on known anatomical compartmentalization. Hence, LIMB allows the imaging of diaphyseal or metaphyseal areas as well as peri-cortical vs. deep-marrow regions, which are known to differ in their cellular composition. As we demonstrated by imaging sessile plasma cells (which are present in the bone marrow in frequencies of less than 1% of all hematopoietic cells), LIMB is suitable for the analysis of rare cells, despite the rather small field of view. This kind of analysis is crucial to improve our understanding of both hematopoiesis and immunological memory.

Upon fluorescently marking the lumina of blood vessels as a way to identify the same tissue regions in different imaging sessions[21, 31], we unexpectedly found the vasculature to be markedly dynamic during steady-state homeostasis. As compared to other tissues, the bone marrow is characterized by a much higher frequency of proliferating cells[3], and an additional level of dynamics is added by the motility of hematopoietic cells. There is a constant egress of cells[5], but cells can also enter the marrow tissue, as in the case of memory T cells or plasma blasts[34, 37]. Currently, our experiments using different strategies in order to label proliferating cells indicate that dynamics occurring in the non-vascular compartment may affect the positioning of the vessels rather than proliferation of the endothelial cells. Future studies based on LIMB analysis will show whether the observed dynamics are solely caused by a passive displacement of the vessels induced by proliferation or motility of bone marrow cells, or whether they are the result of an active process such as neovascularization, especially in light of recently published findings, which indicate that angiogenesis in the bone marrow mechanistically differs from other organs[38]. In any case, we expect that our results will have implications on our understanding of bone marrow microenvironment organization. They add complexity to the concept of how various tissue niches within the bone marrow are regulated. In the future we will investigate the impact of stromal network dynamics on the niches, since stromal cells may also contribute to the stability of those niches by acting as a scaffold in the tissue.

Concluding, LIMB is a unique method, which enables us to longitudinally analyze the same tissue areas in the deep bone marrow of individual mice by intravital multi-photon microscopy. Our technique will open up new ways for analyzing both long-term processes occurring with slow dynamics as well as short-term processes, characterized by fast cellular dynamics. LIMB can be applied to image any process occurring in the bone marrow, including regenerative processes, such as bone formation in adaptation or after injury, as well as tumor formation and bone marrow metastasis, to name only a few examples.

Methods

Two-photon laser-scanning microscopy. Multi-photon fluorescence imaging experiments were performed using a specialized laser-scanning microscope based on a commercial scan head (TriMScope II, LaVision BioTec GmbH, Bielefeld, Germany). We used a 20× objective lens (IR-coating, NA 0.45, Olympus, Hamburg, Germany) combined with GRIN lenses (Fig. 1, GRINTech GmbH, Jena, Germany) to focus the excitation laser radiation into the sample and to collect the emitted fluorescence. Detection of the fluorescence signals was accomplished with photomultiplier tubes in the ranges of (466 ± 20) nm, (525 ± 25) nm, (593 ± 20) nm, and (655 ± 20) nm. paGFP was photoactivated at 840 nm. Both, activated paGFP and GFP were excited at 940 nm and detected at (525 ± 25) nm. eYFP (*Prx-1:YFP* mice) was excited at 940 nm and detected at (525 ± 20) nm and (593 ± 20) nm, while tdRFP was excited at 1100 nm and detected at (593 ± 20) nm. Blood vessels were labeled with Qdots excited at 940 or 1100 nm and detected at (593 ± 20) nm. In all imaging experiments we used an average maximum laser power of 10 mW to avoid photodamage, at a typical pixel dwell time of 2 µs. The maximum peak photon flux was 10^{29} photons cm^{-2} s^{-1}, in accordance to the values measured using conventional two-photon microscopy. The acquisition time for an image with a field of view of 150 × 150 $µm^2$ and a digital resolution of 497 × 497 pixel was 800 ms, as well as for a field of view of 350 × 350 $µm^2$ and a digital resolution of 507 × 507 pixel. We acquired 70 µm *z*-stacks (*z*-step size 6 µm) each 30 s over a total time course of typically 45 min. Calvarial and tibial imaging were performed using the same microscope setup. In contrast to LIMB, we used a 20× water-immersion objective for focusing (IR coated, NA 0.95, Olympus, Hamburg, Germany).

Data analysis. Image segmentation and tracking of all cells was performed using segmentation, object-recognition, and tracking plugins in Imaris (Bitplane AG, Zurich, Switzerland). Cell tracks that were present in the field of view for more than 10 recorded time points (i.e., 5 min) were included in the analysis. Statistical analysis of the data was performed using Prism (Graph Pad Software Inc., San Diego, USA).

Mice. All mice used were on a *C57/Bl6J* background. *CD19:tdRFP* fate mapping mice were generated in our lab by crossing *CD19:Cre*[28] onto *ROSA26:tdRFP*[29] mice. *Prx-1:Cre* mice[30] were crossed onto *ROSA26:eYFP* mice (*Prx-1:YFP*). Photoactivatable GFP (*paGFP*) mice, which ubiquitously express paGFP[18], were kindly provided by Prof. M. Nussenzweig. *CX_3CR1:GFP* mice express EGFP in monocytes, dendritic cells, NK cells, and brain microglia under control of the endogenous *cx3cr1* locus[39]. All mice were bred in the animal facility of the DRFZ. All animal experiments were approved by Landesamt für Gesundheit und Soziales, Berlin, Germany, in accordance with institutional, state, and federal guidelines.

Surgical preparation for longitudinal intravital imaging. We used a lateral approach to expose the femoral shaft of the right hind limb of mice anaesthetized with 1.5–2.0% isoflurane. Initially, an incision of ~1.5 cm was made into the shaved and disinfected skin between the knee and hip joint, parallel to the femur. The underlying muscles were dissected and retracted along the delimiting fascia. Then, a 0.65 mm pilot hole in the distal half of the diaphysis was drilled through the cortex using an electric precision drill (FBS 240/E Proxxon GmbH, Foehren, Germany) mounted on a stand to ensure minimal damage to the underlying bone marrow tissue. Ring forceps were applied to fix the bone in position. We placed the TiCP grade 4 implant parallel onto the femoral shaft and drilled the other two pilot holes (0.31 mm) for the bicortical screws manually through the complete shaft. Here, the holes in the implant act as drill templates. When fully inserted, the bone screws lock in the fixation plate, and thus prevent any movement or rotation. The wound was frequently washed during surgery with sterile NaCl solution and sewed with an absorbable surgical thread (Surgicryl Rapid PGA, USP 6-0, SMI, St. Vith, Belgium). Finally, we attached the reference plate. All animals were kept on a temperature-controlled heating device throughout the surgery (Supplementary Fig. 2). For longitudinal calvarial imaging we used a permanent window glued with bone cement onto the calvarial bone, leaving a circular window freely accessible[40]. The window glass was supported by a customized metal ring kindly provided by Dr. Rinnenthal, J.-L. (Charite—Universitätsmedizin, Berlin, Germany).

Clinical scoring system. Total clinical scoring post-surgery was based on behavior and appearance of the individual mice. The total clinical score represents the sum of eight factors (physical appearance, state of mucosae, motoric ability, wound healing, body weight loss, food and water consumption, response to provocation) rated on a scale of 0–3. No animal was scored to a total clinical score higher than 4.

Histochemistry. Femurs were fixed in 4% paraformaldehyde and transferred to 10–30% sucrose/PBS for cryoprotection. Fixed bone sample and implant were covered with Kawamoto's medium (SCEM, Section-Lab Co. Ltd., Hiroshima, Japan) in order to avoid air bubbles during separation. Bones were frozen and cryo-

sectioned using Kawamoto's film method[41]. Movat's pentachrome stainings were performed on 7 µm sections[42]. Brightfield images were generated by three-dimensional tile scanning on a Biorevo (BZ-9000, Keyence GmbH, Neu Isenburg, Germany) using the BZ-II Viewer with a 10×, NA 0.45 (air) objective lens. Images were stitched using BZ-II Analyzer and processed with Fiji software.

Fluorescence microscopy. Bones were fixed and sectioned as described above. Sections of 7 µm were blocked with 5% FCS/PBS for 30 min and stained with antibodies in 5% FCS/PBS/0.1% Tween for 1–2 h at room temperature: CD45 (1:100, ThermoFisher eBioscience, Frankfurt, Germany, 30-F11), Sca-1-APC (1:200, eBioscience, 17-5981-82), Laminin (1:200, Sigma-Aldrich, Taufkirchen, Germany, L9393), c-kit-PE (1:100, 130-102-542, Miltenyi, Bergisch Gladbach, Germany), Ki-67-bio (1:100, eBioscience, 14-5698-82), Endomucin (1:100, Santa Cruz, sc-65495), CD31-A488 (1:100, R&D Systems, FAB3628G). Sections were washed with PBS/0.1% Tween three times and incubated with secondary Abs (LifeSciences-Sigma-Aldrich, Taufkirchen, Germany) for 1 h at room temperature. Nuclei were stained with 1 µg ml^{-1} DAPI (Sigma-Aldrich) in PBS and mounted with Fluorescent Mounting Medium (DAKO, Hamburg, Germany). Overview images were generated by three-dimensional tile scanning on a LSM710 (Carl Zeiss MicroImaging, Jena, Germany) using Zen 2011 software, with either a 10×, NA 0.3 (air) objective lens for complete femoral bone marrow sections, or a 20×, NA 0.5 (air) objective lens for partial scans (implant area, distal bone). Maximum intensity projection images and stitched overviews were created using Zen 2011 and processed with Fiji. For tracking of CMTPX-labeled transferred cells, splenocytes were isolated and incubated with CellTracker Red CMTPX, according to the manufacturer's protocol (ThermoFisher, Frankfurt, Germany). 1×10^6 splenocytes were transferred to recipient mice. Bones were harvested 4 h after transplantation and femurs were processed as described in the immunofluorescence method section. Sections were stained with DAPI and fluorescent images were generated by three-dimensional tile scanning on a Biorevo (BZ-9000, Keyence GmbH, Neu Isenburg, Germany) using BZ-II Viewer with a 10×, NA 0.45 (dry) objective lens. Images were stitched using BZ-II Analyzer and processed with Fiji software.

EdU labeling and staining. Proliferating cells were labeled using EdU at 1.6 mg kg^{-1} mouse weight injected in PBS intraperitoneally 2 h before sacrifice[7]. Femoral bone sections were stained using the Click-iT EdU Alexa Fluor 647 kit (LifeSciences-Sigma-Aldrich, Taufkirchen, Germany), according to the manufacturer's protocol.

Flow cytometry. Diaphyseal ends including growth plate and secondary ossification centers of femurs were cut off and discarded. An 18 gauge needle was inserted into the distal end of the long bone and the bone marrow was thoroughly flushed out with 5 ml of cold (4°C) MACS buffer (0.5% BSA, 2 mM EDTA in PBS). LIMB implants were removed after flushing. Cells were re-suspended, filtered with a 50 µm cell strainer, spun down 6 min at 75 × *g*, and re-suspended in an erythrocyte lysis buffer. After washing, FcR were blocked using antibodies against CD16/32 (DRFZ in house clone 2.4G2, 5 µg ml^{-1}) and stained with antibodies on ice for 40 min. After washing the cells were acquired with a FACSymphony (BD Bioscience, Heidelberg, Germany) system and populations analyzed in FlowJo10. Cell counts were performed on $n = 6$ individuals. Live lymphocytes were divided into the following populations: progenitors: LSK cell (lin$^-$sca1$^+$ckit$^+$), long-term hematopoietic stem cell (LT HSC, lin-sca1$^+$ckit$^+$CD150$^+$CD48$^-$), short-term HSC (ST HSC, lin$^-$sca1$^+$ckit$^+$CD150$^+$CD48$^+$), multi-potent progenitor (MPP, lin$^-$sca1$^+$ckit$^+$CD150$^-$CD48$^+$), common lymphoid progenitor (CLP, LSK$^-$IL7R$^+$Flk2$^+$), common myeloid progenitor (CMP, lin$^-$sca1$^-$ckit$^+$CD34$^+$CD16/32$^-$), megakaryocyte-erythroid progenitor (MEP, lin$^-$sca1$^-$ckit$^+$ CD34$^-$CD16/32$^-$) and granulocyte-macrophage progenitor (GMP, lin$^-$sca1$^-$ckit$^+$CD34$^+$CD16/32$^+$), dendritic cell progenitor (DCP, lin$^-$sca1$^-$Flk2$^+$IL7R$^+$) B cells: propreB (B220$^+$CD19$^-$ckit$^+$Flk2$^+$), preBI (B220$^+$CD19$^+$ckit$^+$), preBII (B220$^+$CD19$^+$ckit$^-$IgM$^-$CD25$^+$), immature B cells (B220$^+$CD19$^+$ckit$^-$IgM$^+$IgD$^-$), mature B cells (B220$^+$CD19$^+$cki^{t-}IgM$^+$IgD$^+$), plasma cells (CD138high) T cells CD4 T cells (CD3$^+$CD4$^+$), CD8 T cells (CD3$^+$CD8$^+$) innate immune cells: natural killer cells (NK cells, NK1.1$^+$), granulocytes (CD11b$^+$Gr1$^+$), monocytes/macrophages (CD11b$^+$Gr1$^-$), dendritic cells (DCs, CD11c$^+$). Antibodies used: CD19-FITC (1:800, BioLegend, Fell, Germany, 115506), B220-FITC (1:800, BioLegend 103206), Gr1-FITC (1:800, BioLegend 108406), CD3-FITC (1:800, BioLegend 100204), CD11b-FITC (1:800, BioLegend 101206), Ter119-FITC (1:800, BioLegend 116206), IL7R-Pe-Cy7 (1:100, BioLegend 135014), B220-BV510 (1:400, BioLegend 103247), CD34-A647 (1:200, eBioscience 51-0341-82), CD16/32-A450 (1:800, eBioscience 48-0161-82), sca1-APC-Cy7 (1:400, BioLegend 108126), Flk2-Pe (1:100, BioLegend 135306), CD19-BV650 (1:400, BioLegend 115541), ckit-A700 (1:200, eBioscience 56-1172-82), c-fms-APC (1:200, eBioscience 17-1152-82), ckit-APC (1:200, BioLegend 135108), CD150-Pe (1:800, BioLegend 115904), CD48-Pe-Cy7 (1:800, BioLegend 560731), sca1-A700 (1:200, eBioscience 56-5981-82), CD138-BV421 (1:800, BioLegend 142508), IgM-APC (1:400, BioLegend 406509), CD25-APC-Cy7 (1:400, BioLegend 102026), IgD-A488 (0.7 µg ml^{-1}, in house, clone 11.26c), CD4-Pe-Cy7 (1:800, eBioscience 25-0042-82), CD8-APC (1:800, BioLegend 100712), CD3-APC-Cy7 (1:200, eBioscience 47-0031-82), CD11c-FITC (1:800, BioLegend 117306), NK1.1-Pe (1:800, BioLegend 108707), Gr1-PB (1:800, BioLegend 108429), CD11b-A700 (1:800, eBioscience 56-0112-82).

Mouse activity analysis. Analysis of mouse activity and motility was performed using radio-frequency identification (RFID) technology to identify and track individual mice within a cage. Animals were subcutaneously tagged with biocompatible glass-encapsulated RFID transponders (EURO I.D., Frechen, Germany) and were detected by a 2 × 4 sensor plate system (Phenosys, Berlin, Germany) underneath the cage. The frequency of crossed sensors serves as an approximate activity measure. Physical activity was normalized to the mean value of activity measured over 3 days before surgery. Before that, mice had been placed in the cage for at least 2 days. The relative change in activity for each mouse is displayed. For sham treatment, animals were put under anesthesia.

Ex vivo µCT. Femoral bones were harvested and fixed as described above. Fixed bones were measured in 20–30% sucrose solution using the vivaCT 40 (Scanco Medical AG, Bruettisellen, Switzerland). Scans were performed with 70 kVp and an isotropic voxel size of 10.5 µm. Reconstructed scans were converted into tiff-stacks for further data analysis. Bone morphological measurements from µCT 3D reconstructions were performed using the intensity. For bone thickness under the fixation plate and on the opposite site of the bone, areas were chosen as shown in Fig. 2e. For each position, the intensity profile was approximated with two Gaussian curves. The width of each Gaussian curve was considered to represent bone thickness at the respective position. For intact contralateral femurs, we performed the same measurements choosing a mirrored position of the bone to account for the fact that the LIMB femurs are always right femurs and the contralateral bones are left femurs.

Data availability. All relevant data are saved on the institutional servers. The data that support the findings of this study are available from the corresponding authors upon reasonable request.

Received: 14 March 2017 Accepted: 25 September 2017
Published online: 18 December 2017

References

1. Ramasamy, S. K. et al. Regulation of hematopoiesis and osteogenesis by blood vessel-derived signals. *Annu. Rev. Cell Dev. Biol.* **32**, 649–675 (2016).
2. Tokoyoda, K., Hauser, A. E., Nakayama, T. & Radbruch, A. Organization of immunological memory by bone marrow stroma. *Nat. Rev. Immunol.* **10**, 193–200 (2010).
3. Zehentmeier, S. et al. Static and dynamic components synergize to form a stable survival niche for bone marrow plasma cells. *Eur. J. Immunol.* **44**, 2306–2317 (2014).
4. Roth, K. et al. Tracking plasma cell differentiation and survival. *Cytometry A* **85**, 15–24 (2014).
5. Beck, T. C., Gomes, A. C., Cyster, J. G. & Pereira, J. P. CXCR4 and a cell-extrinsic mechanism control immature B lymphocyte egress from bone marrow. *J. Exp. Med.* **211**, 2567–2581 (2014).
6. Itkin, T. et al. Distinct bone marrow blood vessels differentially regulate haematopoiesis. *Nature* **532**, 323–328 (2016).
7. Kusumbe, A. P., Ramasamy, S. K. & Adams, R. H. Coupling of angiogenesis and osteogenesis by a specific vessel subtype in bone. *Nature* **507**, 323–328 (2014).
8. Junt, T. et al. Dynamic visualization of thrombopoiesis within bone marrow. *Science* **317**, 1767–1770 (2007).
9. Kohler, A. et al. G-CSF-mediated thrombopoietin release triggers neutrophil motility and mobilization from bone marrow via induction of Cxcr2 ligands. *Blood* **117**, 4349–4357 (2011).
10. Mazo, I. B. et al. Bone marrow is a major reservoir and site of recruitment for central memory CD8+ T cells. *Immunity* **22**, 259–270 (2005).
11. Mazo, I. B. & von Andrian, U. H. Adhesion and homing of blood-borne cells in bone marrow microvessels. *J. Leukoc. Biol.* **66**, 25–32 (1999).
12. Lo Celso, C., Lin, C. P. & Scadden, D. T. In vivo imaging of transplanted hematopoietic stem and progenitor cells in mouse calvarium bone marrow. *Nat. Protoc.* **6**, 1–14 (2011).
13. Wu, J. W., Runnels, J. M. & Lin, C. P. Intravital imaging of hematopoietic stem cells in the mouse skull. *Methods Mol. Biol.* **1185**, 247–265 (2014).
14. Kohler, A. et al. Altered cellular dynamics and endosteal location of aged early hematopoietic progenitor cells revealed by time-lapse intravital imaging in long bones. *Blood* **114**, 290–298 (2009).
15. Chen, Y., Maeda, A., Bu, J. & DaCosta, R. Femur window chamber model for in vivo cell tracking in the murine bone marrow. *J. Vis. Exp.* **113**, e54205 (2016).

16. Kim, S., Lin, L., Brown, G. A., Hosaka, K. & Scott, E. W. Extended time-lapse in vivo imaging of tibia bone marrow to visualize dynamic hematopoietic stem cell engraftment. *Leukemia* **31**, 1582-1592 (2017).
17. Park, D. et al. Endogenous bone marrow MSCs are dynamic, fate-restricted participants in bone maintenance and regeneration. *Cell Stem Cell* **10**, 259–272 (2012).
18. Hawkins, E. D. et al. T-cell acute leukaemia exhibits dynamic interactions with bone marrow microenvironments. *Nature* **538**, 518–522 (2016).
19. Trachtenberg, J. T. et al. Long-term in vivo imaging of experience-dependent synaptic plasticity in adult cortex. *Nature* **420**, 788–794 (2002).
20. Farrar, M. J., Wise, F. W., Fetcho, J. R. & Schaffer, C. B. In vivo imaging of myelin in the vertebrate central nervous system using third harmonic generation microscopy. *Biophys. J.* **100**, 1362–1371 (2011).
21. Barretto, R. P. et al. Time-lapse imaging of disease progression in deep brain areas using fluorescence microendoscopy. *Nat. Med.* **17**, 223–228 (2011).
22. Lewandowski, D. et al. In vivo cellular imaging pinpoints the role of reactive oxygen species in the early steps of adult hematopoietic reconstitution. *Blood* **115**, 443–452 (2010).
23. Matthys, R. & Perren, S. M. Internal fixator for use in the mouse. *Injury* **40**, S103–S109 (2009).
24. Perren, S. M. Evolution of the internal fixation of long bone fractures. The scientific basis of biological internal fixation: choosing a new balance between stability and biology. *J. Bone Joint Surg. Br.* **84**, 1093–1110 (2002).
25. Gerber, C., Mast, J. W. & Ganz, R. Biological internal fixation of fractures. *Arch. Orthop. Trauma Surg.* **109**, 295–303 (1990).
26. Perren S. M., Cordey J., Rahn B. A., Gautier E. & Schneider E. Early temporary porosis of bone induced by internal fixation implants. A reaction to necrosis, not to stress protection? *Clin. Orthop. Relat. Res.* **232**, 139–151 (1988).
27. Hyldahl, C., Pearson, S., Tepic, S. & Perren, S. M. Induction and prevention of pin loosening in external fixation: an in vivo study on sheep tibiae. *J. Orthop. Trauma* **5**, 485–492 (1991).
28. Victora, G. D. et al. Germinal center dynamics revealed by multiphoton microscopy with a photoactivatable fluorescent reporter. *Cell* **143**, 592–605 (2010).
29. Kusumbe, A. P. et al. Age-dependent modulation of vascular niches for haematopoietic stem cells. *Nature* **532**, 380–384 (2016).
30. Bremer, D. et al. Longitudinal intravital imaging of the retina reveals long-term dynamics of immune infiltration and its effects on the glial network in experimental autoimmune uveoretinitis, without evident signs of neuronal dysfunction in the ganglion cell layer. *Front. Immunol.* **7**, 642 (2016).
31. Gibson, V. B. et al. A novel method to allow noninvasive, longitudinal imaging of the murine immune system in vivo. *Blood* **119**, 2545–2551 (2012).
32. Sapoznikov, A. et al. Perivascular clusters of dendritic cells provide critical survival signals to B cells in bone marrow niches. *Nat. Immunol.* **9**, 388–395 (2008).
33. Cariappa, A. et al. Perisinusoidal B cells in the bone marrow participate in T-independent responses to blood-borne microbes. *Immunity* **23**, 397–407 (2005).
34. Tokoyoda, K. et al. Professional memory CD4+ T lymphocytes preferentially reside and rest in the bone marrow. *Immunity* **30**, 721–730 (2009).
35. Sercan Alp, O. et al. Memory CD8(+) T cells colocalize with IL-7(+) stromal cells in bone marrow and rest in terms of proliferation and transcription. *Eur. J. Immunol.* **45**, 975–987 (2015).
36. Tokoyoda, K., Egawa, T., Sugiyama, T., Choi, B. I. & Nagasawa, T. Cellular niches controlling B lymphocyte behavior within bone marrow during development. *Immunity* **20**, 707–718 (2004).
37. Hauser, A. E. et al. Chemotactic responsiveness toward ligands for CXCR3 and CXCR4 is regulated on plasma blasts during the time course of a memory immune response. *J. Immunol.* **169**, 1277–1282 (2002).
38. Ramasamy, S. K., Kusumbe, A. P., Wang, L. & Adams, R. H. Endothelial Notch activity promotes angiogenesis and osteogenesis in bone. *Nature* **507**, 376–380 (2014).
39. Jung, S. et al. Analysis of fractalkine receptor CX(3)CR1 function by targeted deletion and green fluorescent protein reporter gene insertion. *Mol. Cell Biol.* **20**, 4106–4114 (2000).
40. Fuhrmann, M., Mitteregger, G., Kretzschmar, H. & Herms, J. Dendritic pathology in prion disease starts at the synaptic spine. *J. Neurosci.* **27**, 6224–6233 (2007).
41. Kawamoto, T. Use of a new adhesive film for the preparation of multi-purpose fresh-frozen sections from hard tissues, whole-animals, insects and plants. *Arch. Histol. Cytol.* **66**, 123–143 (2003).
42. Movat, H. Z. Demonstration of all connective tissue elements in a single section; pentachrome stains. *AMA Arch. Pathol.* **60**, 289–295 (1955).

Acknowledgements

We thank Patrick Thiemann and Manuela Ohde for assistance with animal care. This work was supported by DFG FOR 2165 (NI1167/4-1 and NI1167/4-2 to R.A.N. and HA5354/6-1 and HA5354/6-2 to A.E.H.), TRR130, TPC01 (to R.A.N. and A.E.H.), TP17 (to A.E.H.) and TP16 (to H.D.C.) and HA5354/8-1 to A.E.H. D.R. and J.S. are members of the Berlin-Brandenburg School for Regenerative Therapies (BSRT). We would like to thank the Charité-Universitätsmedizin Electron Microscopy Facility (Prof. S. Bachmann) for help with experiments. The authors thank Randy Lindquist for proofreading of the manuscript.

Author contributions

R.A.N., A.E.H., D.R. and J.S. designed the study, analyzed data and interpreted results. R.A.N., A.E.H., D.R., J.S., R.G., G.P., A.R. and S.Z. performed experiments. R.M., R.N., K.S.-B. and G.D. provided expertise for the implant design, surgery and Movat's pentachrome histochemical staining. F.M. provided expertise in the analysis of HSCs subsets frequencies and interpretation of these data with respect to the characterization of post-surgical homeostasis. Y.W., H.-D.C. and S.N. helped with mouse activity analysis. R.A.N. and A.E.H. wrote the manuscript.

Additional information

Supplementary Information accompanies this paper at https://doi.org/10.1038/s41467-017-01538-9.

Competing interests: R.M. and R.N. (RISystem AG, Davos, Switzerland) declare competing financial interests. The implant for longitudinal imaging will be commercialized by RISystem AG, Davos, Switzerland. The remaining authors declare no competing financial interests.

Reprints and permission information is available online at http://npg.nature.com/reprintsandpermissions/

Publisher's note: Springer Nature remains neutral with regard to jurisdictional claims in published maps and institutional affiliations.

Open Access This article is licensed under a Creative Commons Attribution 4.0 International License, which permits use, sharing, adaptation, distribution and reproduction in any medium or format, as long as you give appropriate credit to the original author(s) and the source, provide a link to the Creative Commons license, and indicate if changes were made. The images or other third party material in this article are included in the article's Creative Commons license, unless indicated otherwise in a credit line to the material. If material is not included in the article's Creative Commons license and your intended use is not permitted by statutory regulation or exceeds the permitted use, you will need to obtain permission directly from the copyright holder. To view a copy of this license, visit http://creativecommons.org/licenses/by/4.0/.

© The Author(s) 2017

11. Lebenslauf

Mein Lebenslauf wird aus datenschutzrechtlichen Gründen in der elektronischen Version meiner Arbeit nicht veröffentlicht.

12. Publikationsliste

Naundorf S*, Schröder M*, Höflich C, Suman N, Volk HD, Grütz G. IL-10 interferes directly with TCR-induced IFN-gamma but not IL-17 production in memory T cells. Eur J Immunol. 2009;39:1066-77. IF: 5.179

Schottelius AJ, Zügel U, Döcke WD, Zollner TM, Röse L, Mengel A, Buchmann B, Becker A, Grütz G, **Naundorf S**, Friedrich A, Gaestel M, Asadullah K. The role of mitogen-activated protein kinase-activated protein kinase 2 in the p38/TNF-alpha pathway of systemic and cutaneous inflammation. J Invest Dermatol. 2010;130:481-91. IF: 6.270

Reismann D, Stefanowski J, Günther R, Rakhymzhan A, Matthys R, Nützi R, Zehentmeier S, Schmidt-Bleek K, Petkau G, Chang HD, **Naundorf S**, Winter Y, Melchers F, Duda G, Hauser AE, Niesner RA. Longitudinal intravital imaging of the femoral bone marrow reveals plasticity within marrow vasculature. Nat Commun. 2017;8:2153. IF: 12.353

Riedel R, Addo R, Ferreira-Gomes M, Heinz GA, Heinrich F, Kummer J, Greiff V, Schulz D, Klaeden C, Cornelis R, Menzel U, Kröger S, Stervbo U, Köhler R, Haftmann C, Kühnel S, Lehmann K, Maschmeyer P, McGrath M, **Naundorf S**, Hahne S, Sercan-Alp Ö, Siracusa F, Stefanowski J, Weber M, Westendorf K, Zimmermann J, Hauser AE, Reddy ST, Durek P, Chang HD, Mashreghi MF, Radbruch A. Discrete populations of isotype-switched memory B lymphocytes are maintained in murine spleen and bone marrow. Nat Commun. 2020;11:2570. IF: 12.121

13. Danksagung

In diesen Zeilen möchte ich allen danken, die zum Gelingen dieser Arbeit beigetragen haben.

Mein besonderer Dank gilt Prof. Dr. Hans-Dieter Volk, Direktor des Instituts für Medizinische Immunologie der Charité, Universitätsmedizin Berlin, für die Möglichkeit der Anfertigung der Doktorarbeit in seinem Institut und die bereitwillige Übernahme der Betreuung meiner Promotion.

Mein größter Dank gilt PD Dr. Gerald Grütz für die Überlassung der interessanten Fragestellung und seiner Betreuung. Während der Durchführung meiner Doktorarbeit stand er mir mit Rat und Tat zur Seite. Auf seine konstruktiven Vorschläge für anfallende Probleme jeglicher Art konnte ich immer zählen.

Darüber hinaus möchte ich mich ganz herzlich bei meinen Laborkollegen Katrin Bossmann, Nadine Nippe, Nadine Koch, Marcel Krüger und Nimisha Suman für die sehr gute Laboratmosphäre und die gegenseitige Unterstützung danken. Es hat mir viel Spaß gemacht mit euch zusammen zu arbeiten.
Zudem bedanke ich mich bei allen Mitarbeitern des Instituts für Medizinische Immunologie der Charité, die meine Arbeit begleitet und mir mit vielen nützlichen Ratschlägen weitergeholfen haben. Nicht zu vergessen, all diejenigen, die für diese Experimente ihr Blut geopfert haben.

Ein besonderer Dank gilt auch Prof. Khusru Asadullah (Schering/Bayer Pharma AG) und seinen Kollegen für die gute Kooperation. Prof. Matthias Gaestel (Medizinische Hochschule Hannover) danke ich für die MK2 und MK3 Knockout-Mäuse.

Außerdem bedanke ich mich bei Dr. Hyun-Dong Chang (DRFZ) für seine fachliche Unterstützung. Prof. Raluca Niesner und Prof. Anja E. Hauser (DRFZ) danke ich für die gute Zusammenarbeit.

Insbesondere möchte ich mich bei meiner Familie bedanken, die mich stets bestärkt und unterstützt haben.